



**HAL**  
open science

## Lahars and debris flows: Characteristics and impacts

Jean-Claude Thouret, S. Antoine, C. Magill, C. Ollier

► **To cite this version:**

Jean-Claude Thouret, S. Antoine, C. Magill, C. Ollier. Lahars and debris flows: Characteristics and impacts. *Earth-Science Reviews*, 2020, 201, pp.103003. 10.1016/j.earscirev.2019.103003. hal-02454078

**HAL Id: hal-02454078**

**<https://uca.hal.science/hal-02454078>**

Submitted on 7 Mar 2022

**HAL** is a multi-disciplinary open access archive for the deposit and dissemination of scientific research documents, whether they are published or not. The documents may come from teaching and research institutions in France or abroad, or from public or private research centers.

L'archive ouverte pluridisciplinaire **HAL**, est destinée au dépôt et à la diffusion de documents scientifiques de niveau recherche, publiés ou non, émanant des établissements d'enseignement et de recherche français ou étrangers, des laboratoires publics ou privés.



Distributed under a Creative Commons Attribution - NonCommercial 4.0 International License

1                                   **Lahars and debris flows: characteristics and impacts**

2  
3                                   Thouret J.-C. <sup>1</sup>, Antoine S <sup>2</sup>, Magill C. <sup>3</sup>, Ollier C. <sup>4</sup>

4  
5  
6     <sup>1</sup> Université Clermont-Auvergne, CNRS, IRD, OPGC, Laboratoire Magmas et Volcans,  
7 F-63000 Clermont-Ferrand, France (Phone +33 4 73 34 67 73 Email: j-claude.thouret@uca.fr)

8     <sup>2</sup> Institut de Physique du Globe, Laboratoire de tectonique et mécanique de la lithosphère,  
9 1 rue Jussieu 75005 Paris, France (Phone +33 1 83 95 74 00; Email: santoine@ipgp.fr)

10    <sup>3</sup> Department of Environmental Sciences, Faculty of Science and Engineering, Macquarie  
11 University, NSW 2109, Australia (Phone +61 2 9850 7477; Email:  
12 christina.magill@mq.edu.au)

13    <sup>4</sup> School of Earth and Environment, The University of Western Australia, 35 Stirling Hwy,  
14 Crawley WA 6009 (Phone: 61 8 9386 9639; Email: cliff.ollier@uwa.edu.au)

15  
16  
17  
18  
19  
20                                   *Revised and re-submitted to Earth-Science Reviews, 26 October 2019*

## 35 **ABSTRACT**

36 This review describes the mechanisms of lahars and debris flows, and their impacts on  
37 buildings, infrastructure and other valuables. Lahars are a type of debris flow restricted to  
38 volcanic debris. Both water-rich mass flows, having solid concentration from 40 to 80%  
39 volume and density from 1,300 to 2,400 kg/m<sup>3</sup>, exhibit velocities ranging between 3 and 30  
40 m/s, peak discharge as high as 48,000 m<sup>3</sup>/s, volume as large as 100 million m<sup>3</sup>, and can flow  
41 down valley as far as 100 km from the source. The review presents the array of methods and  
42 tools used in the field-based and experimental study of hydraulic, physical and rheological  
43 characteristics of volcanic and non-volcanic debris flows worldwide. These mass flows share  
44 several characteristics and effects with floods, but fewer studies have analyzed the wide range  
45 of impacts produced by lahars and debris flows. Damages are induced by three principal  
46 forces driving impacts: (1) hydrodynamic pressure, (2) hydrostatic pressure, and (3) the  
47 collisional forces of boulders acting as missiles. The impacts of debris flows are diverse,  
48 cascading and interacting because the size, the velocity and the proportion of rock debris  
49 mixed with water constantly change down valley. The review will complement previous  
50 studies in three ways: 1) we investigate how debris-flow characteristics and processes lead to  
51 damage mechanisms on buildings, infrastructure and lifelines; 2) we explore the broad range  
52 of valuable assets impacted by debris flows, and; 3) we analyze the physical vulnerability of  
53 valuables, leading to a review of indicators, matrices and fragility functions, which may lead  
54 to better understand loss. The review shows that economic impacts of lahars and debris flows  
55 extend well beyond the immediate costs of loss of life and asset damage. Enhanced  
56 understanding of flows and their impacts can improve risk mitigation and land use planning.

57

58 **Keywords:** lahar; debris flow; impact; building; infrastructure; exposure; vulnerability;  
59 damage; loss.

60

## 61 **1. INTRODUCTION**

62

63 In this paper, we discuss the processes and associated impacts of lahars (LHs) and debris  
64 flows (DFs). DFs occur in numerous environments: hillslopes, alluvial fans, and catchment  
65 channels that can vary greatly in geomorphology and lithology. Most DFs exhibit similar,  
66 unique morphologies, often forming a channel constricted by lateral levees and ending in  
67 depositional lobes (Iverson, 2014). Being more frequent than LHs, non-volcanic DFs have  
68 been generally more lethal. Dowling and Santi (2014) reported a total of ca. 77,800 fatalities

69 from 213 events since 1950, making them the third most lethal and destructive natural hazard  
70 following earthquakes and floods. Among volcanic hazards, lahars are more lethal and  
71 destructive than any other direct cause except for pyroclastic density currents (PDCs) and  
72 tsunamis (**Fig. 1**). Brown et al. (2017) reported that since 1500 AD, approximately 56,300  
73 fatalities (26% of total volcano-related fatalities) have been LH related.

74 Because large volumes of unstable rock, debris and water can spill over from abundant  
75 valleys draining volcanoes, lahar-inundated areas can be larger (Vallance and Iverson, 2015)  
76 and wider than those fed by DFs (Vallance and Scott, 1997). LHs can wreak havoc at much  
77 greater distances from a volcano than PDCs due to greater mobility. The 1985 LHs from  
78 Nevado del Ruiz, Colombia flowed 100 km beyond the Central Cordillera towards the  
79 Magdalena River valley (Pierson et al. 1990). Exceptionally large-volume LHs at Cotopaxi  
80 volcano, Ecuador, reached 370 km from source in 1877 (Mothes et al., 1998). In contrast,  
81 channeled PDCs reach distances typically less than 20 km down valley (e.g., at Merapi,  
82 Indonesia in 2010: Surono et al., 2012).

83 The main objective of this review is to describe and explain the magnitude and diversity of  
84 impacts that LHs and DFs can exert on buildings, infrastructure, lifelines and other economic  
85 valuables or assets. The review is based on LH/DF case studies observed in the field (**Table**  
86 **1**) and on small- and large-scale experiments made by engineers and scientists in instrumented  
87 river channels and flumes. The review will complement previous studies in four ways: 1)  
88 exploring the broad range of valuables impacted by LHs and DFs; 2) investigating how and to  
89 what extent LH/DF characteristics and processes lead to damage, 3) explaining the damage  
90 mechanisms related to LH/DF characteristics; and (4) analyzing the physical vulnerability of  
91 valuables, which may lead to better understanding of loss.

92

## 93 **1.1 Terminology**

94

### 95 *1.1.1 Flow types*

96

97 Lahars (LHs) and debris flows (DFs) are potentially destructive water-saturated mass-flows  
98 acting in mountainous regions and in areas where steep slopes cut down in loose sediment.

99 These flows can be divided into two categories using sediment concentration, grain-size  
100 distribution and bulk density (Vallance, 2000; Hungr and Jakob, 2005; Vallance and Iverson,  
101 2015):

102 1. Debris flows (DFs) are mixtures of debris and water with high sediment concentrations that  
103 move downslope due to gravity as surging sediment slurries (Coussot and Meunier, 1996;  
104 Vallance, 2000). DFs comprise a solid phase of at least 60 vol% (>80 wt%), thoroughly  
105 mixed with water. The solid component includes mostly gravel and boulders with sand, silt  
106 and clay proportions remaining low. A threshold of 3 wt% of silt and clay helps  
107 distinguishing non-cohesive from cohesive DFs (Scott, 1988; Scott et al., 1995). The density  
108 of a DF ranges between 1,800 and 2,400 kg/m<sup>3</sup>, twice as much as the muddy water that flows  
109 in stream channels during floods (Pierson, 1980).

110 2. Hyperconcentrated flows (HCFs) are two-phase flows intermediate in sediment  
111 concentration between normal streamflows and DFs, with densities between 1,300 and 1,800  
112 kg/m<sup>3</sup>. HCFs transport between 20 and 60 vol% (40 and 80 wt%) of sediment (Beverage and  
113 Culberton, 1964; Pierson, 2005).

114 LHs are water saturated, and both liquid and solid interactions influence their behavior and  
115 distinguish them from debris avalanches (Vallance and Iverson, 2015), or from jökulhlaups  
116 released from glaciers in Iceland (Gudmundsson, 2015). LH/DFs usually consist of more than  
117 one flow regime (Vallance, 2000; **Figs. 2 and 3**). An individual lahar pulse can be broken  
118 down into three successive segments: (1) the ‘head’ or front is characterized by the densest  
119 slurry reaching the highest flow height and peak velocity, (2) the ‘body’ represents the bulk of  
120 the lahar and is characterized by packets or pulses driven by variations in sediment  
121 incorporation and dilution and/or deposition, and (3) the ‘tail’ represents the recessional limb  
122 of the slurry having the lowest sediment concentration due to dilution (Pierson, 1986; **Fig.**  
123 **2A**).

124 Post-eruptive, ‘secondary’ LHs are typically more frequent and protracted than syn-eruptive,  
125 ‘primary’ LHs. LHs represent a long lasting threat as they can be triggered long after an  
126 eruption (**Table 1**): at least 15 years following the 1980 Mt. St-Helens eruption (Major, 2000)  
127 and 13 years after the 1991 Pinatubo eruption, Philippines (Major et al., 1996; Pierson et al.,  
128 1996; Pierson and Major, 2014). LH initiation mechanisms include direct transformation from  
129 debris avalanches, rapid melting of snow and ice during eruptions, outbreaks of impounded  
130 lakes, and rainfall on fresh tephra deposits (Pierson and Major, 2014). DFs also represent  
131 frequent perils in the shadow of dormant edifices prone to landslides and/or heavy rainstorms,  
132 e.g., Casita in Nicaragua in 1998 (Scott et al., 2005), and from rapid landslides or ‘earthflows’  
133 that transform into cohesive DFs (Scott et al., 2001).

134

### 135 **1.1.2 Impacts**

136 A natural hazard impact can be defined as direct or indirect, and tangible or intangible, and is  
137 usually regarded as a loss to an environment or a society (Swiss Re, 1998). Jenkins et al.  
138 (2014) defined impact as a function of hazard and the vulnerability of exposed valuables.  
139 Here, we use impact as a collective term that includes the direct and indirect actions and  
140 consequences that LHs and DFs bear on valuables: buildings, infrastructure or networks.  
141 We further distinguish the physical effects (e.g., land or building burial), the direct and  
142 indirect processes (e.g., loading or capillarity rise), and ultimately the damage as mechanical  
143 failure (collapse) and/or the removal of valuables: e.g. a building, dam, bridge or a vehicle  
144 (**Table 2**). Direct loss deals with the physical effects of the hazard on individuals (death or  
145 injury) or infrastructure (reduction in functionality, failure and/or removal). Indirect loss  
146 concerns the effect on society's functionality via damage to utility services or local business,  
147 the loss of revenue and jobs, the failure of networking activities, increases in living costs and  
148 insurance, etc. Intangible losses are defined as the social, psychological and cultural effects of  
149 the disasters (Petrucci, 2012). These long-term effects must not be overlooked, but they  
150 remain beyond the scope of this paper (Rodolfo, 1995; Grattan and Torrence, 2007).  
151 The physical vulnerability of valuables, as well as damage and loss, can be measured using  
152 indicators, matrices and fragility or vulnerability functions (Wilson et al., 2014, 2017;  
153 Papathoma-Köhle et al., 2017; Prieto et al., 2018). Vulnerability indicators or indices based  
154 on hazard intensities (velocity, depth, pressure) and physical variables help assess how a  
155 system is susceptible to natural hazard impacts. Vulnerability functions, expressed as curves,  
156 quantify a component's damage or loss relative to total loss as a function of hazard intensity.  
157 Vulnerability functions were described for DFs by Papathoma-Köhle et al. in 2017. Fragility  
158 functions, also expressed as curves, describe the probability that a particular state or scale of  
159 damage, for a specific asset, will be exceeded as a function of hazard intensity or magnitude.  
160 Wilson et al (2017) coined the term impact metric (IM) in order to assess volcanic impact  
161 (damage) to critical infrastructure. To describe vulnerability, an IM has a value between 0 and  
162 1, which indicates a proportion of total economic loss.

163 The impacts of hazards on buildings and infrastructure have recently been the focus of  
164 specialized articles, e.g. ash fall (Wilson et al., 2012), pyroclastic density currents (PDCs)  
165 (Jenkins et al., 2013), snow avalanches (De Biagi et al., 2015), and flash floods (Calianno et  
166 al., 2013). With the notable exception of Jenkins et al. (2015), who analyzed building damage  
167 on Merapi's slopes following the 2010 eruption, very few studies have quantitatively  
168 examined the impacts of lahars on critical infrastructure or lifelines, as examined in the ash  
169 fall and PDC cases of Wilson et al. (2014, 2017), Zuccaro et al. (2013a, b, 2015) and Deligne

170 et al. (2017). In contrast to tephra fallout and PDCs, LH impacts have not been covered in  
171 detail in the literature except for the synthesis of Pierson et al. (2014), which primarily dealt  
172 with strategies for LH hazard reduction. Previous studies considering LH impacts have  
173 focused mostly on social and institutional responses (Leone and Gaillard, 1999 and Santi et  
174 al., 2011), or described effects without any structural analysis of damaged buildings (Scott,  
175 2010). According to Blong (1984), DFs exert impacts on six exposures: 1) humans and  
176 animals; 2) the built environment; 3) lifeline networks (water, sanitation, transport,  
177 communications, power) and equipment; 4) rural environments, crops, forests, fisheries, and  
178 natural vegetation; 5) economic activities and services, and 6) social fabrics. **Table 2**  
179 summarizes the flow actions and processes that put lives in danger (Baxter and Horwell,  
180 2015). LHs can sterilize cultivated or forest land for a relatively short period of time –from  
181 five to twenty years under wet climate. Soils are then rapidly formed in loose LH deposits,  
182 while their material, which is mined along valleys and on fans, also brings benefits to local  
183 people, e.g., in Indonesia (De Belizal et al., 2013).

184

## 185 **1.2 Hazardous mass flows and agents of landscape change**

186

187 We considered **42** case studies to construct a record of severe and costly water-rich mass-flow  
188 events (**Table 1**). LHs and DFs have wreaked havoc in many towns and across diverse  
189 environments, including Kelut (Indonesia) in 1909, Nevado del Ruiz (Colombia) in 1985,  
190 Pinatubo (Philippines) in 1991-1998, Ruapehu (New Zealand) in 1945, 1996 and 2007, Sarno  
191 (Italy) in 1998, Soufrière Hills (Montserrat) between 2001 and 2004, and Mayon (Philippines)  
192 in 2006. Non-volcanic DF events also appear in **Table 1**, but these hazards are covered  
193 extensively in the literature including the parameter dataset elaborated by Rickenmann (1999)  
194 and 213 events reported by Dowling and Santi (2014).

195 Case studies indicate that physical impacts from LHs and DFs affect a variety of resource  
196 categories (**Table 2**). Impacts on buildings and infrastructure have been examined in several  
197 papers (e.g., Johnston et al., 2000; Zanchetta et al., 2004; Jenkins et al., 2015), but lifelines  
198 such as water, power and telecommunication networks have been less studied. LH and DF  
199 effects are principally described through land burial or inundation and pressure exerted on  
200 walls and bridges. However, other physical and bio-chemical effects can affect critical  
201 lifelines, disrupt economic activity, and damage strategic resources including health facilities  
202 and civil protection arrangements. LHs and DFs also induce downcutting, while removal of

203 check dams or retention walls can add more material to channeled flows, and produce missiles  
204 (e.g., Arequipa in Peru; Thouret et al., 2013; Ettinger et al., 2015).  
205 Newhall and Solidum (2015) aptly summarized the key hazardous, geomorphic property of  
206 LHs/DFs as follows: “Unlike floods that come and go, lahars come...and stay”. **Table 3**  
207 displays the principal geomorphic processes induced by LHs and DFs in drainage networks.  
208 All bury land and alter the river bed, bank morphology, and drainage networks. Geomorphic  
209 changes that increase hazards inside channels are fourfold: (i) gradient steepening, headward  
210 wall retreat and denudation in the steep initiation area; (ii) channel progradation; (iii) channel  
211 widening due to land burial or entrenchment due to scouring, and (iv) enhanced channel  
212 curvature and river sinuosity. Geomorphic changes that induce hazards outside channels are:  
213 (i) land burial beyond channel overspill, and (ii) infilling of channels and flow avulsion  
214 towards secondary, often non-active drainage channels, that bring hazards to hitherto un-  
215 affected valuables and un-prepared people.  
216 LHs contribute to the growth of fans and feed sediment-delivery systems to widespread ring  
217 plains as documented at Mayon following its 1984 eruption (Rodolfo and Arguden, 1991),  
218 Pinatubo after the large 1991 eruption (Rodolfo, 1995; Pierson and Janda, 1992; Punongbayan  
219 and Newhall, 1996; Hayes et al., 2002), Santiaguito over the period 1987-2000 (Harris et al.,  
220 2006), Merapi following the 2010 eruption (De Belizal et al., 2013; Solikhin et al., 2015;  
221 Thouret et al., 2015), Semeru between 1981 and 2011 (Thouret et al., 2014a), and Mt.  
222 Ruapehu over longer intervals (Cronin and Neall, 1997; Keigler et al., 2011; Tost et al.,  
223 2015). Extraordinary sediment delivery, excess sedimentation rates, and perturbations of the  
224 drainage network were the geomorphic responses of the catchments following the 2008-2009  
225 Chaitén eruption in Chile, as described by Pierson et al. (2013), Pierson and Major (2014) and  
226 Major et al. (2016). During the waning phase of explosive activity, modest rainfall triggered  
227 an extraordinary sediment flush: ten kilometers from the volcano, the Chaitén River channel  
228 aggraded 7 m and the river avulsed through a coastal town. After channel avulsion, a second  
229 delta added about  $2 \times 10^6 \text{ m}^3$  of sediment to the initial  $0.5\text{--}1.5 \times 10^6 \text{ m}^3$  deposited at the mouth  
230 of the Chaiten River from 11 to 14 May 2008; and by late 2011 it aggregated approximately  
231  $11 \times 10^6 \text{ m}^3$ .

232

## 233 **2. CHARACTERISTICS OF LAHARS AND DEBRIS FLOWS**

234

235 Hydraulic characteristics of flows and solid/liquid concentrations were defined in early  
236 classifications (Costa, 1984, 1988; Coussot and Meunier, 1996; Iverson, 1997; Lavigne and

237 Thouret, 2000), while rheological parameters were further measured using small-scale  
 238 experiments, laboratory testing (**Fig. 4**, Ancey, 2007; Hübl et al., 2009; Dumaisnil et al.,  
 239 2010), and large-scale experiments carried out in channels (Rickenmann, 1999; Doyle et al.,  
 240 2010, 2011; Zhou and Ng, 2010) or experimental flumes (Iverson et al., 2010, 2011). A list of  
 241 physical and dimensionless parameters of small-scale, experimental DFs and large-scale,  
 242 natural DFs was provided by de Haas et al. (2015, their Table 2). The characteristics of LHs  
 243 and DFs reported here have been derived from forty-two case studies (**Table 1**).

244

## 245 **2.1 Hydraulic characteristics**

246

247 1. Velocity ( $u$ , in m/s) of flows can be broken down into three components (Doyle et al.,  
 248 2007): (i) surface velocity  $u_{surf}$ , the instantaneous velocity calculated from video film footage,  
 249 (ii) travel velocity  $u_r$  corresponding to the total flow velocity, and (iii) body velocity  $u_b$ , the  
 250 depth averaged velocity for a given location. The body velocity  $u_b$  is assumed to be  
 251 proportional to the surface velocity with  $k$  as a correction factor. Ranging between 0.7 and 0.9  
 252 (Creutin et al., 2003),  $k$  is described by a vertical velocity distribution (Cronin et al., 1999;  
 253 Hayes et al., 2002). The flow front velocity is often used in equations as the flow head plays a  
 254 major role in the initial impact intensity on structures, which reaches its maximum when the  
 255 boulder-rich head is thick and fast (Lavigne and Suwa, 2004; Thouret et al., 2007). Travel  
 256 velocity reaches a peak slightly after the front because the latter, being thicker and coarser,  
 257 exerts more friction.

258 2. Discharge rate ( $Q$ , in  $m^3/s$ ) is a function of the mean velocity of the flow, its ability to erode  
 259 and bulk material from the channel bed and banks, and channel geometry. Coupled with high  
 260 velocities, discharge rate can influence the degree of building and infrastructure damage along  
 261 the flow path. It is therefore a key parameter for understanding LH/DF impact. Flow  
 262 discharge is shown by the equation:

$$263 \quad Q(t^{i+1}, t^i) = \frac{1}{2} (A^i u_b^i + A^{i+1} u_b^{i+1}) \quad (1)$$

264 where  $A$  is the wetted area,  $u_b$  is the body velocity,  $Q$  is the average discharge of the flow and  
 265  $i$  represents individual measurements recorded at intervals of  $\Delta t = t^{i+1} - t^i$  (Doyle et al., 2011).  
 266 Variations in discharge rate with time and space depend on cycles of sediment bulking and  
 267 debulking. Bulking is the amount of pre-existing material removed from the channel bed and  
 268 banks and entrained by the flow, whereas debulking is achieved through dilution and  
 269 deposition of material down valley, together with water infiltration into the channel bed. The

270 formula from Vallance (2000) calculates the apparent bulking and debulking factors ABF:

$$271 \quad ABF = 1 - (R_f/R_i)(S_i/S_f), \quad (2)$$

272 where  $R$  is the proportion of the reference component (or size class) not affected by bulking,  $S$   
273 is the proportion of any other component (or size class) of interest,  $i$  indicates proximal  
274 (initial) value, and  $f$  indicates downstream values. Bulking is controlled by the erodibility of  
275 the channel bed and bank material, the volume of sediment available for erosion, and the flow  
276 parameters (Pierson, 1995; Fagents and Baloga, 2006). The capacity for entrainment of  
277 material from channel beds and banks is responsible for dramatic growth in flow volume and  
278 peak discharge, e.g., four times over a distance of ~100 km at Nevado del Ruiz (Pierson et al.,  
279 1990). Bulking is an important process in lahar impact analysis as erosion can threaten the  
280 stability of river banks and constructions, and hence population safety.

281 3. Flow depth ( $H$ , in m), or hydraulic radius during emplacement, can be 4 to 5 times the  
282 deposit thickness. A deeper flow results in a larger area being exposed and flows that reach a  
283 higher level around buildings and infrastructure.

284 4. The relationship between velocity and depth is expressed by the dimensionless Froude ( $Fr$ )  
285 number. Defined as the ratio between inertial and gravitational forces acting on flows,  $Fr$   
286 describes the stability of the deformable flow surface as follows:

$$287 \quad Fr = \frac{u}{\sqrt{gD}} \quad (3)$$

288 where  $u$  is the flow velocity,  $g$  the acceleration due to gravity, and  $D$  the hydraulic maximum  
289 depth of the flow in the channel (Manville et al., 1998). LH Froude numbers commonly range  
290 between 0.5 and 1.5 (Tiberghien et al., 2007). In cold and hot LH cases,  $Fr$  characterizes two  
291 different regimes with identical slopes but different velocities (Arguden and Rodolfo, 1990).  
292 For a subcritical flow ( $Fr < 1$ ), runoff will be deep and low with a flat and smooth surface,  
293 whereas in a supercritical flow ( $Fr > 1$ ), runoff will be shallow and fast, while its surface will  
294 exhibit waves and disturbances such as hydraulic jumps (Manville et al., 1998). By comparing  
295 small-scale experimental flows and measured real DFs, the relationship between  $Fr$  and  
296 hydrodynamic and hydrostatic pressures has been assessed (Hübl et al., 2009).

297 5. The velocity, discharge rate, flow depth, and the width/depth ratio of the channel influence  
298 flow mobility, which also varies due to the river bed characteristics such as slope angle, basal  
299 friction angle and bed roughness. In turn, the flow momentum will determine the runout  
300 distance, a pivotal parameter for delineating at-risk areas down valley.

301

## 302 **2.2 Physical and rheological properties**

303

304 Physical thresholds of flow behavior and rheological changes are of much interest in hazard  
305 assessment (Pierson and Costa, 1987; Costa, 1984, 1988; Ancey, 2007). Using data from 28  
306 large-scale flume experiments, Iverson et al. (2011) argued that a key feature of DF behavior  
307 was the development and persistence of dilated, high-friction, coarse-grained flow fronts,  
308 pushed from behind by nearly liquid, finer-grained debris. DFs show some cohesive behavior  
309 and relatively little internal mixing. Thus a ‘slug’ of material moves down the channel and  
310 deposition can occur as the result of *en masse* ‘freezing’ of the flow or pulsed deposition  
311 (Major, 1997; Major and Iverson, 1999). HCFs exhibit non-Newtonian behavior, have less  
312 internal cohesion and are dominated by particle–particle interactions and frictional behavior  
313 (Mulder and Alexander, 2001). Four properties further help characterize LHs and DFs.

314 1. Bulk density ( $\rho$ ), i.e. the sum of the fluid density ( $\rho_f$ ) and the solid component density ( $\rho_s$ ),  
315 varies between 1,500 and 2,500 kg/m<sup>3</sup> on average; the calculated bulk flow density ranges  
316 between 1,330 and 1,800 kg/m<sup>3</sup> for hyperconcentrated flows and increases to 1,800 - 2,300  
317 kg/m<sup>3</sup> for debris flows, depending on lithological components and solid concentrations  
318 (Zanchetta et al., 2004). However, flume experiments have revealed that debris porosities and  
319 bulk densities evolve between the dilated front and the more stabilized bulk densities of the  
320 body (Iverson et al., 2011).

321 2. Viscosity ( $\mu$  in Pa.s, commonly 0.001–0.1) is the property of a fluid that slows the settling  
322 of suspending particles and allows it to resist shear deformation, thus controlling the shear and  
323 flow rates (Pierson, 2005). Shear deformation is related to shear stress (equation 3), a force  
324 that corresponds to the erosion exerted by the flow on the stream bed, which ranges between  
325 10<sup>2</sup> and 5.10<sup>4</sup> poises (Costa, 1984; **Table 1**):

$$326 \quad \tau = \rho g R S \quad (4)$$

327 where  $\tau$  is the total shear stress,  $\rho$  is fluid density,  $g$  is gravitational acceleration,  $R$  is  
328 hydraulic radius and  $S$  is slope. Viscosity is a function of the concentration of sediment or  
329 solid, particularly the silt and clay contents which play an important role in fluid cohesion and  
330 flow mobility. Viscosity depends on inter-particle interactions, and particle-bed and particle-  
331 fluid interactions, the combination of which is a complex and continuous process (Pierson,  
332 2005). Taking this complexity into account, two different viscosity categories are assigned to  
333 two flow categories (**Fig. 4**). According to Pierson and Scott (1985), the transition phase  
334 between a Newtonian and a non-Newtonian (Bingham) fluid can describe a transitional flow  
335 between a hyperconcentrated flow (HCF) and a debris flow (DF).

336 3. Shear stress ( $\tau$ ) is a meaningful parameter in the processes of erosion and bulking.

337 According to equation 3, shear stress is positively correlated with the density of the flow thus

338 the denser a flow, the more erosive it is. Higher density and viscosity increase friction with  
339 the channel bed, thereby reducing velocity. This is the reason why DFs are less swift than  
340 HCFs and much slower than flash floods on steep slopes. The transport of coarse particles,  
341 including boulders, is mostly controlled by the cohesion and buoyancy of the flow body  
342 (Johnson, 1970; Hampton, 1979), while both are positively correlated with flow density  
343 (Costa, 1984). Denser flows will erode the stream bed, incorporate and transport particles.  
344 4. Pore-fluid pressure (*pdf*) exhibits spatial and temporal fluctuations that buffer or harden  
345 flow resistance through the interplay with frictional, collisional or viscous particle-particle  
346 contacts. Iverson et al. (2010, 2011) argued that the prominent role of evolving pore fluid  
347 pressure was the chief mechanical trait distinguishing DF behavior from that of granular  
348 avalanches. High *pdf* renders DFs more mobile as frictional resistance decreases because *pdf*  
349 tends to buffer grain interactions, a tendency described by the Darcy number. Large positive  
350 values of *pdf* were shown in flume experiments to develop in wet bed sediments when they  
351 are overridden by DFs (Iverson et al., 2011). Steep, highly resistant, surge fronts of coarse-  
352 grained material without measurable pore-fluid pressure are pushed along by relatively fine-  
353 grained and water-rich tails that have a wide range of pore fluid pressures (Mc Coy et al.,  
354 2010). Pore fluid pressure variations in flows influence the fundamental process of  
355 entrainment of debris from the channel bed and banks when flow momentum and speed  
356 increase. Entrainment in turn feeds the sediment bulking process of erosive flows.

357

### 358 **2.3 What ultimately determines lahar/debris flow ability to impact valuables?**

359

360 As many as six conditions explain why LHs and DFs are some of the most erosive mass flows,  
361 causing damage at distances greater than those attained by floods (**Table 1**).

362 1. Flow mobility, volume and momentum ( $\Delta H/L$ , elevation/travel distance) strongly influence  
363 the runout distance and inundated area (Rickenmann, 1999, 2005; Lube et al., 2009; de Haas  
364 et al., 2015). Both runout distance and inundated area are pivotal to predict the extent of  
365 damage (Toyos et al., 2007; Bettella et al., 2012; Iverson et al., 2016; Han et al., 2017a,b).  
366 The area inundated versus the volume of natural and small-scale experimental DFs show a  
367 perfect linear correlation on a log-log scale (de Haas et al., 2015). Runout distance increases  
368 with flow type (e.g., more mobile water-rich flows) and grain-size distribution (cohesive  
369 LHs/DFs), high slope gradient and wide channels on ring plains, and the existence of lateral  
370 levees on steep fans (5–15°), influencing the flow width/depth ratio and mobility.

371 2. LHs and DFs are unsteady flows that move in a pulsating way, forming packets or surges  
372 each with clear variation of flow properties along the length of the surge, which exert erosion  
373 and aggradation that fluctuate in space and time (Doyle et al. 2010, 2011; McCoy et al.,  
374 2010). Such mass flows erode their channels by cutting debris away from the banks and the  
375 base. Undercutting of banks can cause problems in populated areas, as witnessed during Mt.  
376 Pinatubo's LHs following the 1991 eruption. Channels can suddenly widen from a few meters  
377 to tens of meters, thereby inducing costly damage for neighborhoods built along river banks.  
378 Moreover, excavation of the channel bottom will deepen and increase confinement of  
379 LH/DFs, allowing them to travel more rapidly. With larger debris removed, the flow can  
380 continue to move while dissipating less of its gravitational energy due to friction. Thus, a  
381 valley-confined HCF can continue to move long after boulders have dropped out.

382 3. Unsteady and pulsating LH/DF behavior depends on bulking/debulking; as the flow  
383 volume, flow density and grain size distribution changes, so too does its erosion power  
384 through pore pressure changes (Manville et al., 2013). Bulking, counterbalanced by  
385 infiltration into the channel bed, will increase volume and peak discharge by a factor of three  
386 to ten relative to initial values. This happens often at the flow head, which exerts the  
387 maximum hydrodynamic pressure, in particular when the snout is boulder rich. In contrast,  
388 debulking will decrease the flow pore pressure, but less concentrated flow pulses or tails will  
389 induce incision of the deposit and undercutting of structures such as bridges. Changes in flow  
390 volume and velocity, sediment bulking/debulking and peak discharge tend to decrease  
391 downstream, as shown by flat and long-lasting LH/DF discharge hydrographs (e.g. Nevado  
392 del Ruiz in 1985). However, changes in flow type (from HCF to DF and again from DF to  
393 HCF) induce erosion. This leads to burial followed by incision, which occurred with each of  
394 lahar packets during the 90 minute flow at Semeru in 2008 (**Fig. 5**), and for as long as 16  
395 hours at Ruapehu in 2007 (Manville and Cronin, 2007; Cole et al., 2009).

396 4. LH/DF composition, grain-size distribution and segregation between particle  
397 concentrations fundamentally affect flow dynamics (Iverson et al., 2010). Particle segregation  
398 can occur by size, shape, and density during flow stratification, and can cause boulder-rich  
399 snouts that push water ahead. A series of steep-fronted surges will thus exert several pressure  
400 pulses that may further debilitate structures already weakened by the first flow snout. LHs and  
401 DFs can deposit sediment 'en masse', thereby invading a structure, or through step-wise  
402 vertical accretion, applying hydrostatic load against structures causing bending or breaking  
403 with time. Hydrostatic pressure acts together with dynamic pressure on walls and bridge piles.  
404 Hydrostatic forces can lead to equalization of lahar depths on the inside and outside of the

405 buildings. As equalization usually takes a reasonable amount of time, hydrostatic force is thus  
406 not often accounted for in numerical modeling of flow impacts on structures (e.g., Mead et al.  
407 2017). In contrast, HCFs deposit sediment progressively by accretion of bedload and settling  
408 from suspension, thereby exerting less head pressure upon encountering a structure. In this  
409 case, dynamic and hydrostatic pressure exerted by HCFs remains high for long time intervals,  
410 instead of the brief and high peak of dynamic pressure exerted by LH/DF fronts on the outside  
411 of structures.

412 5. Channel morphology plays a role in runout distance and flooding area. De Haas et al.  
413 (2015) explored DF morphology using small-scale experiments compared to natural cases.  
414 Channel morphology typically consists of high, steep ( $>20^\circ$ ) levees and flat, rough beds,  
415 while flow fronts create stubby lobes. Longitudinal levees confine flows, thereby promoting  
416 high velocity and runout distance. Steeper channel slopes lead to longer runout and higher  
417 flow velocities, induced by the increased gravitational potential energy, thereby increasing  
418 dynamic pressure. Runout distance and inundation area increase with channel width, but very  
419 wide channels will induce thinner flows, hence shallower inundated areas.

420 Three geometric parameters of the channel-bed system determine how confined LH/DFs, like  
421 PDCs, can spill over banks and avulse to induce widespread impacts: reduced channel  
422 capacity  $C$  (in  $m^2$ ), change in the longitudinal rate of channel confinement  $\Delta C/\Delta x$  (in  $m^2/m$ ),  
423 and change in channel sinuosity  $\Delta\theta/\Delta x$  (in  $^\circ/m$ ) (Lube et al., 2011; Solikhin et al., 2015). Such  
424 geomorphological conditions change flow dynamics, decoupling the more mobile upper flow  
425 from the basal flow, leading to overbank flow. Overspill not only induces hazards for areas  
426 adjacent to the river channel, but also for secondary channels beyond the main valley, leading  
427 to further threats due to flow avulsion (**Table 3**), e.g., during and after the 2006 and 2010  
428 Merapi eruptions (Lube et al., 2011; De Belizal et al., 2013; Solikhin et al., 2015; Thouret et  
429 al., 2015; Charbonnier et al., 2018a).

430 6. Variability in flow-path topography can strongly influence flow velocity, sediment erosion  
431 and deposition, and hence the behavior of the front and rear of the flow during the debris-rich  
432 erosional phases. The head is often higher than the rear portion owing to friction with the  
433 channel topography and to the fact that the front will first incorporate loose debris. The flow  
434 tail does not incorporate excess debris, instead becoming more diluted due to deposition. The  
435 more water-rich tail acts like a flood, therefore becoming more rapid, providing efficiency to  
436 erode the channel and banks. As a result, flow fronts and tails show contrasting behavior:  
437 heads carry the most debris, but only up to a threshold where the amount can be held, then  
438 erosion decreases. Water-rich tails continue to erode channels, but a large amount of debris

439 cannot be removed because the kinetic energy is much less than at the front. Thus, the tail  
440 velocity decreases, favoring incision of the deposits that were pushed down and aside by the  
441 head.

442

### 443 **3. METHODS FOR ANALYSING LAHAR AND DEBRIS-FLOW** 444 **CHARACTERISTICS AND IMPACTS**

445

446 As LHs and DFs are dangerous and difficult to predict, a combination of many methods is  
447 used to measure flow dynamics, to assess damage, and to delineate hazard-prone areas.

448

#### 449 **3.1 Field based surveys, empirical and geophysical approach**

450

451 Field based methods aim to observe and analyse LH/DFs and their deposits, and the diversity  
452 of impacts, leading to a scale of damage. Embedded in GIS, damage inventories are also  
453 employed for outlining inundated areas and vulnerable valuables.

454

##### 455 ***3.1.1 Event observations and geophysical measurements of flow parameters***

456

457 Arrays of geophysical sensors in and near river channels allow measurement of LH/DF  
458 characteristics and understanding of mechanical impacts. Parameters include: mean and peak  
459 velocity, mean and peak discharge, depth range, sediment concentration, surface instability,  
460 temperature and pH. In turn, these parameters help induce important characteristics of  
461 LHs/DFs such as Froude number, density, viscosity and bulking capacity (Pierson et al.,  
462 1990; Doyle et al., 2010, 2011; Coviello et al., 2018). Combined with hydraulic  
463 characteristics of LH/DFs recorded in channels (Doyle et al., 2010), rheological tests using  
464 flow material in laboratory settings (Major and Pierson, 1992; Dumaisnil et al., 2010) aim to  
465 describe and understand LH behavior. DF behavior and dynamics were studied in small-scale  
466 and natural channels mostly in the Alps (Rickenmann, 1999) and Himalayas, while recent  
467 methods measure LH/DF parameters using a broad array of geophysical tools (Itakura et al.,  
468 2005; McCoy et al., 2010; Burtin et al., 2013; Mainsant, 2014).

469 1. *Direct measurements* of LH/DF propagation include sampling material inside the flows or  
470 video camera recordings, e.g., Lavigne et al. (2000a,b) and Wibowo et al. (2015) at Merapi  
471 (Indonesia), Scott et al. (2005) at Casita (Nicaragua), Doyle et al. (2010, 2011) at Semeru  
472 (Indonesia), Cole (2009, 2011) and Lube et al. (2012) at Mt. Ruapehu (New Zealand), Okano

473 et al. (2012) at Mt. Yakedake (Japan), and Vázquez et al. (2016) at Volcán Colima (Mexico).  
474 Sampling using buckets or hatches carved in the channel bed help collect the flow mixture at  
475 frequent time intervals, which can be used to analyze the particle size, density and sediment  
476 concentration of LHs (Cole, 2011) as well as the water chemistry to trace their origin (Cronin  
477 et al., 1996; Lube et al. 2012). Video recordings allow the flow velocity and the transport of  
478 large blocks to be measured, and surficial instabilities such as rolling waves and hydraulic  
479 jumps to be recorded (Lavigne and Thouret, 2003; Doyle et al., 2010; McCoy et al. 2010;  
480 Starheim et al., 2013).

481 *2. Indirect measurements* may be carried out by geophysical sensors, including ultrasonic or  
482 laser radars recording flow stages (Iverson et al., 2010; Doyle et al., 2011). Mean velocity and  
483 discharge can be estimated based on this information and the channel geometry. Basal normal  
484 stress and shear stress can be measured by load cells, and two load cells are used to infer  
485 changes in sediment concentration (Cole et al., 2009). Pore pressure sensors measure the  
486 pressure of the interstitial fluid, which can increase due to turbulence, but can also decrease  
487 with fluid dilatation due to collisional phenomena (Cole et al., 2009).

488 Seismic recording has been widely deployed for monitoring all types of ground movements  
489 including mass flows, landslides, and rockfalls (Tonnellier et al., 2013). Diverse seismic  
490 sensors are used to record ground vibrations generated by LHs and DFs: (1) seismometers, (2)  
491 acoustic devices such as geophones, microphones, hydrophones, and (3) accelerometers  
492 (Bänziger and Burch, 1990; Itakura et al., 1997; Suwa et al., 2000; Lavigne et al., 2000b;  
493 Huang C.J. et al., 2004, 2007; Arattano and Marchi, 2008; Cole et al., 2009; Burtin et al.,  
494 2013). A few studies have focused specifically on characterizing DFs by means of seismic  
495 survey and frequency analysis to determine flow dynamics and kinematics (Zobin et al. 2009;  
496 Cole et al. 2009; Cole 2011; Vázquez et al., 2016; Coviello et al., 2018). The signal duration,  
497 frequency composition, apparent velocity, and correlations between them are the most  
498 significant and discriminant parameters (Tonnellier et al., 2013); although it is recognized that  
499 analysing flow signals may be biased by other seismic sources such as tremors and rockfalls,  
500 particularly near active volcanoes. The amplitude and frequency band signals generated by  
501 LH/DF events are often determined by (1) the type of particle motion, (2) the distribution and  
502 size of particles, (3) properties of the interstitial fluid, and (4) the geometry and nature of the  
503 channel (Huang C.J. et al., 2004; Cole, 2011; Lai et al., 2018).

504 The succession of phases within a lahar event, as depicted in **Figures 2B and 3**, can also be  
505 recognized using seismic records (**Fig. 5**; Cole et al., 2009, Cole, 2011; Doyle et al., 2010,  
506 2011). The front is defined by an increase in height and surface velocity, which generates

507 relatively low seismic frequency. The head phase, behind the front, shows a rapid increase in  
508 sediment concentration with corresponding intense seismic frequency. The body phase is  
509 marked by seismic activity lower than the head phase, while a further decrease in seismic  
510 energy reflects the LH tail. Variations in frequency, which depend on flow composition and  
511 dynamics, led several authors (Marcial et al., 1996; Lavigne et al., 2000b; Huang C.J. et al.  
512 2004, 2007) to similar conclusions: LH fronts generate signals between 10 and 30 Hz (in  
513 some cases due to the accumulation of large blocks at the flow front), while LH tails trigger  
514 frequency signals between 60 and 80 Hz. HCFs, instead, generate higher frequency bands  
515 between 100 and 300 Hz (Marcial et al., 1996).

516 Different mechanical models of flows can explain differences in the spectral composition of  
517 LHs illustrated by seismic signals (Zobin et al., 2009; Vázquez et al., 2014, 2016). Cole et al.  
518 (2009) found correlations between the signal amplitude, location of seismometers with respect  
519 to the channel, and the flow regime of different LHs in the same channel on Mt. Ruapehu,  
520 New Zealand, which were triggered by a phreatic eruption. The HCFs were turbulent, and the  
521 collisions between particles and those with the channel generated signals with higher  
522 amplitude and greater energy in the perpendicular direction than parallel. The snow-slurry  
523 LHs, mixtures of mud and slush, showed higher signal energy parallel to the channel due to  
524 lateral sedimentation that isolated the edges, and were then identified as laminar flows.

525

### 526 ***3.1.2 Observed impacts***

527

528 Inventories of a range of damage levels have been elaborated in urban areas along mountain  
529 torrents and fans, and river channels draining volcanoes and ring plains (Zanchetta et al., 2004  
530 for non-eruptive LHs in Sarno, Italy; Nigro and Faella, 2008 and Sosio et al., 2007 for DFs in  
531 Italy; Solikhin et al., 2015 and Jenkins et al., 2015 for LHs around Semeru and Merapi  
532 volcanoes). Essential for understanding the mechanisms that led to damage, inventories of  
533 impacts have been elaborated on both large scale (e.g., a city) and small-scale (e.g., a ravine  
534 or a neighborhood) using remote sensing techniques and field surveys following disasters  
535 (Kerle, 2002, Kerle et al., 2003; Ettinger et al., 2015). Damage quantification is aided by pre-  
536 disaster reference imagery (Kerle and Oppenheimer, 2002). Once post-disaster changes have  
537 been detected, high-spatial resolution images, including unmanned aerial vehicles and Lidar  
538 survey data, are embedded in Geographic Information Systems (GIS) where the coded  
539 damage levels overlie layers depicting buildings and other valuables, which are automatically  
540 recognized through cognitive systems engineering (Kerle and Hoffman, 2013).

541 *Remote sensing for post-event damage assessment*

542 Remote sensing techniques applied to high-spatial resolution imagery, together with GIS  
543 mapping and DEMs, can be used in risk assessment to describe DF/LH events and their  
544 catastrophic impacts (Hubbard et al., 2007). These techniques are ideally part of timely  
545 responses leading to improved emergency relief. Similar methods were often applied to  
546 analyse the catastrophic effects from earthquakes (Dong and Shan, 2013), flash floods for the  
547 city of Arequipa, Peru (Delaite et al., 2005; Ettinger et al., 2014), and for structural damage  
548 due to cyclones, e.g., in La Réunion Island following Cyclone Bejisa in 2014 (Yésou et al.,  
549 2015). In the latter case, pre- and post-disaster data were used to assess changes in buildings  
550 integrity. Using long-time series of satellite images such as Landsat, scientists analyzed the  
551 factors leading to mass-flow events, including structural mapping of the flank collapse and  
552 DF triggered by Hurricane Mitch on the dormant Casita volcano in Nicaragua, 1998 (Scott et  
553 al, 2005) and the calculation of its initial failure volume (Kerle et al., 2003; Devoli et al.,  
554 2009). The availability of very high-spatial resolution sensors launched since 2002 (e.g.,  
555 GeoEye, Quickbird, WorldView, and Pléiades) has allowed mapping of deposits with  
556 unprecedented detail, allowing elementary drainage networks to be extracted, the morphology  
557 of volcanoes to be depicted, and the source of flows together with potential future flows to be  
558 assessed (Thouret et al., 2010, 2015). Such high-spatial resolution ability, for example,  
559 allowed Ettinger et al. (2014) to delineate eroded and unstable channels reaches along the path  
560 of a disastrous HCF in February 2013 in Arequipa, Peru.

561 One pivotal challenge associated with remote sensing methods is the analysis of new images  
562 of the damaged zones rapidly and accurately. Two techniques are used for recognizing  
563 damaged zones: (1) analysis of patterns extracted at a pixel level, and (2) analysis of the  
564 radiometric distribution pattern at a region scale, which is more meaningful in the case of very  
565 high-spatial resolution images (Vetrivel et al., 2016). A critical step is to determine and  
566 delineate appropriate ‘training’ regions in which damage patterns can be recognized and  
567 analyzed, hence gridding is commonly used as the most straightforward strategy. A  
568 segmentation approach, i.e. an object-oriented classification is exploited in which damaged  
569 portions and objects are considered as separated regions (Vetrivel et al., 2016). Additional  
570 methods used for analyzing images are based on learning approaches, and include Scale  
571 Invariant Feature Transform (SIFT), Visual-Bag-of-Words (BoW) and convolutional neural  
572 networks (CNN) (Vetrivel et al., 2016, 2018). Recently, remote sensing techniques have been  
573 improved due to the use of Sentinel 1 and 2 satellites. These pioneers of a future constellation  
574 of 20 satellites expected by 2030, launched by ESA since 2014, are dedicated to Earth

575 monitoring, which includes land and sea changes. Together with very-high resolution imagery  
576 of floods, volcanic eruptions and landslides already exploited by this endeavor, the mission  
577 supports disaster risk management procedures such as rapid and effective post-disaster  
578 damage assessment (Voigt et al. 2011; Kaku et al., 2015; Miyazaki et al., 2015).

579 The principal hindrance to applying these methods to LHs/DFs is not with the analysis of  
580 damage but with the recognition of the phenomenon itself. Indeed, identification of flow  
581 deposits is challenging because LHs/DFs can initiate rapidly, while remote sensing alone  
582 cannot recognize complex deposit structures and compositions (Kerle and Oppenheimer,  
583 2002).

584

### 585 **3.2 Experimental approach**

586

587 Experiments aimed at measuring debris-flow dynamics have been conducted in laboratory and  
588 natural environments. Early laboratory experiments were typically small scale (Armanini,  
589 1997; Armanini et al., 2011; Bugnion et al., 2012a; de Haas et al., 2015) or even miniaturized  
590 (Cui et al., 2015), but recent sets of controlled experiments have been conducted at medium  
591 and large scales (Larcher et al., 2007; McCoy et al., 2010) using outdoor flumes several tens  
592 of meters long loaded with natural material. Aggregated results from such controlled flume  
593 experiments allowed Iverson's USGS group (Major, 1997; Major and Iverson, 1999; Iverson  
594 et al., 2010, 2011) to quantify essential LH/DF physical and rheological parameters and  
595 improve our fundamental knowledge on DF behavior. Iverson (2015) stated that both small  
596 experimental DFs have a different behavior from natural DFs in proportion to the height of  
597 the moving mass. Large effects of viscous shear resistance and cohesion, pore fluid pressure,  
598 characteristic macroscopic velocity, and time scales must be addressed in the comparison  
599 between experimental and natural flows.

600 In natural river channels, experiments enabled Rickenmann (1999) to draw empirical  
601 relationships that define DF dynamics across fans, involving volume, peak discharge, flow  
602 velocity, travel distance, and runout distance (**Table 1**). After Marchi et al. (2002) described  
603 DF characteristics in the Italian Alps, Sosio et al. (2007) and Sosio and Crosta (2009, 2011)  
604 added rheological testing and numerical modeling to field observations for one landslide-  
605 triggered DF event in the area. More recently, geophysical sensors, among which  
606 seismometers, AFMs and load sensors, have emerged as critical tools, allowing several teams  
607 at Massey University, New Zealand (Cole, 2009; Procter et al., 2010a,b; Lube et al., 2012)  
608 Colima Volcano Observatory, Mexico (Zobin et al., 209; Vázquez et al., 2016; Coviello et al.,

609 2018) and the Dongchuan debris flow observation and research station in China (Zhou and  
610 Ng, 2010; Hong et al., 2015), to better measure DF dynamics and impacts.

611 Another advance involves the development of physically based models that describe transient  
612 rainfall infiltration and its effect on evolving pore-pressure distributions that may initiate DFs  
613 (Baum et al., 2010). Capra et al. (2010) investigated the role of hydro-repellency, a specific  
614 soil property, related to the role of vegetation cover in LH initiation. Hydro-repellency under  
615 high density, evergreen vegetation with sandy soils can explain the high frequency of LHs at  
616 the beginning of the rainy season during low rainfall events. In these hydrophobic conditions,  
617 infiltration is inhibited and runoff is characterized by high peak discharges that are more  
618 likely to initiate LHs. Jones et al. (2017) examined the role of grain size and antecedent  
619 rainfall on overland and DF triggering mechanisms. Laboratory experiments showed that  
620 increased antecedent rainfall and finer-grained surface tephra individually increased runoff  
621 rates and decreased runoff lag times. These factors, sometimes combined, were driven by  
622 increased residual moisture content and decreased permeability due to surface sealing.

623

#### 624 *Controlled experiments to understand impacts*

625 Small or miniaturized scale experiments allow fluid mechanics experts to observe the physical  
626 and rheological characteristics of two-phase flows and hydraulic characteristics together with  
627 the mechanical response of exposed valuables (Tiberghien et al., 2007; Zhang et al., 2007;  
628 Armanini et al., 2011; Cui et al., 2015). For example, two-phase flows were modelled by  
629 either a mixture of debris and water (Bugnion et al., 2012a,b; Cui et al., 2015) or by polymer  
630 solutions mimicking slurries (Tiberghien et al., 2007). Medium- to small-scale laboratory  
631 experiments settings enabled engineers to learn how a flow analogue hits an obstacle so as to  
632 monitor and quantify its mechanical impacts on a vertical wall, a bridge pier, or a barrier  
633 (Wang et al., 2018). These experiments measure the pressure exerted during impacts and  
634 variations in time and space, related to different categories of flows or slope angles. More  
635 comprehensively, Cui et al. (2015) divide the DF impact process into three phases by  
636 analyzing the variations in impact signals and flow regime. The three phases identified were:  
637 (1) the sudden strong impact of the DF head, (2) continuous dynamic pressure of the body,  
638 and (3) slight static pressure of the tail.

639

#### 640 *Mechanical tests on construction materials*

641 A mechanical approach consists of testing diverse categories of construction material under  
642 the impact of a LH/DF, in order to characterize the strength and durability of a building,

643 bridge or barrier, and to understand failure mechanisms. Three mechanical tests (uniaxial  
644 compression, shearing and pushing) were conducted by Martelli (2011) followed by Arenas  
645 Lopez (2018) on construction materials used in Arequipa (Peru), where buildings have often  
646 been impacted by flash floods and HCFs. Five categories of construction material ranged  
647 from adobe to reinforced concrete. In addition to density and porosity measurements, two  
648 factors were determined using: (1) the Ultrasonic Pulse Velocity, which measures the velocity  
649 of acoustic waves through a material and assesses mechanical characteristics such as the  
650 modulus of elasticity and compressive strength (Goodman, 1989; de Vekey, 1996), and (2)  
651 the Unconfined Strength, which defines the capacity of a material to withstand axially-  
652 directed compressive forces whereby the material is crushed once the limit of compressive  
653 strength has been reached (Hoek and Brown, 1980). Mechanical tests conducted on  
654 construction material led to six principal categories being distinguished on the basis of  
655 mechanical strength. However, the availability of materials, quality of components, and land  
656 use vary according to countries and regions, thereby precluding general conclusions on  
657 strength of particular materials. In addition to the wall material alone, experimental tests and  
658 numerical experiments showed that edifice failure depends primarily on the integrity of the  
659 entire structure.

660 A second type of experiment analyzes the dynamic response of different types of construction  
661 material under LH impact. Zhang et al. (2007) analyzed the behavior of scaled models of  
662 building walls struck by DFs and defined the pressures required for permanent damage to  
663 each class of building material. Engineers used the same set up for the impact force  
664 experiments, which consists of a series of pressure sensors and cameras monitoring an  
665 artificial LH that encounters walls with three designs, namely reinforced concrete, brick  
666 masonry and reinforced masonry combination.

667

### 668 **3.3 Modelling**

669

670 Over the past twenty years, advances in computational modeling have enabled scientists to  
671 simulate the physics of DF initiation, motion and deposition. However, the use of physically  
672 based models for hazard forecasting can be limited by imprecise knowledge of initial and  
673 boundary conditions and material properties. Empirical methods must therefore continue to  
674 play an important role in DF hazard assessment in order to inform modeling (Iverson, 2014).  
675 The most sophisticated models combine digital map-based methods of hazard-zone  
676 delineation with spatially distributed hydrologic and slope-stability models (Griswold and

677 Iverson, 2008). However, all models are complicated by debris rheology that changes down  
678 valley; material is static in the initiation area, then deforms, flows through channels, and later  
679 regains rigidity in the deposition area (Iverson, 2014). Physically based DF models employ  
680 depth-averaged mass- and momentum-conservation equations. Iverson (2014) stated that  
681 numerical methods must be robust enough to simulate the development of shocks (hydraulic  
682 jumps) that occur when moving DF encounter obstacles or abrupt changes in topography.  
683 Modern shock-capturing methods such as the finite-volume can provide accurate solutions as  
684 they can evaluate discontinuous fluxes of conserved quantities between adjacent  
685 computational cells; however, a key challenge arises from the complicating effects of driving  
686 and resisting forces (Iverson, 2014).

687 Several models and programs or codes have been used to reproduce the dynamics of LH/DFs  
688 and to simulate their extent, runout, and effects (**Table 4**). The quality of simulations relies  
689 heavily on DEM spatial resolution and accuracy as topography is still poorly constrained  
690 (Charbonnier et al., 2018a). Current models can be divided into two broad categories, those  
691 geared towards practical work that have seen widespread use in the engineering community,  
692 and those more focused on understanding the underlying physics (Turnbull et al., 2015).

693 Models are categorized in **Table 4** according to three criteria: (i) the modeling goal, either  
694 understanding flow dynamics, or contributing to hazard assessment; (ii) the empirical,  
695 statistical, and physically based method; and (iii) the scale of the modeled watershed or  
696 channel. Three main types of models can be used to simulate flow phenomena (Takahashi;  
697 2014; Han et al., 2017a,b, and all references in **Table 4**): (1) statistical codes such as  
698 LAHARZ-py (Schilling, 2014), and random flow routing models such as DAN-W (Hungr,  
699 2010), TopFlowDF (Scheidl and Rickenmann, 2010, 2011; Horton et al., 2013), used, for  
700 example, to predict runout (Rickenmann, 2005; Hürlimann et al., 2008). As these GIS-based  
701 methods help delineate the extent of potential inundated areas, they serve the pivotal purpose  
702 of assessing potential effects and harmful paths; (2) two-dimensional models based on  
703 shallow water equations such as TITAN2D (Pitman and Le, 2005; Sheridan et al., 2005),  
704 RAMMS (Quan Luna et al., 2011; Han et al., 2013, 2015) and VOLCFLOW (e.g., Kelfoun  
705 and Druitt, 2005), and; (3) three-dimensional models, such as the Lagrangian Smooth  
706 Hydrodynamics Particle code (SPH, Pastor et al., 2009), allow engineers to monitor the  
707 behavior of particles, extract critical velocity and dynamic pressure, and assess flow impacts  
708 using high resolution DEMs based on UAV photogrammetric data (Mead et al., 2015, 2017).  
709 As standard numerical simulations of LH/DF are commonly based on shallow water  
710 equations, new research has sought to shift the approach as these flows are in reality two-

711 phase anisotropic mixtures that display complex rheological behavior and evolve through  
712 space and time. Mathematical codes were recently implemented for rapid landslides,  
713 earthflows and DFs: DCLAW (George and Iverson, 2011, 2014; Iverson and George, 2014,  
714 2016) and EDDA1.0 (Chen and Zhang, 2015). Han et al (2017a) implemented an improved  
715 cellular automaton (CA) model for simulating the extent of DF runout. A CA model consists  
716 of three components: a two-dimensional rectangular cellular space in the DTM, the Moore  
717 neighborhood lattice relation, and a transition function based on a Monte Carlo iteration  
718 algorithm also used to automatically select the flow direction and routine. The results showed  
719 that the DF persistence function was closely related to the channel slope, which approximates  
720 the law of cosines for a steep slope and Gamma law for a gentle slope. The simulated  
721 deposition perimeter, runout distance, and sediment depth were in accordance with field-  
722 based data collected after the 2010 Yohutagawa DF event in Japan.

723 Only a few authors, e.g., Cesca and d'Agostino (2008), have compared performance between  
724 behavior oriented models, such as RAMMS, and hazard assessment oriented programs, such  
725 as FLO-2D (O'Brien and Julien, 2000), that are able to simulate HCFs, by incorporating  
726 modeled rainfall distributions, hydrographs and entrained material. It was found that FLO-2D  
727 gave the best results, even if rheological variables – viscosity and yield stress coupled with  
728 surface detention depth – need further investigations of their physical significance. Surface  
729 detention (i.e. water in temporary storage as a thin sheet over the soil surface during the  
730 occurrence of overland flow) has a large influence on runout distances and maximum lateral  
731 dispersion. In RAMMS simulations, the entire input solid volume is located in a restricted  
732 area and not timed as in a FLO-2D input hydrograph. Therefore, the released DF suddenly  
733 reaches a channel that is insufficient to contain the entire discharge. As a consequence,  
734 avulsion phenomena occur along the channel, producing a larger lateral spread than that  
735 observed in the field.

736 All these models contribute to hazard assessment by delineating LH/DF paths, runouts and  
737 potential inundated areas, and deposit thicknesses (Caballero and Capra, 2014). Coupled with  
738 probabilistic methods and embedded in SIG (Wang et al., 2006; Scheidl and Rickenmann,  
739 2010, 2011), such model outputs represent tools for first-order decision making in case of  
740 water-rich mass flow crises and for long-term planning. Models set up by Proske et al. (2011),  
741 Armanini et al. (2011), Zeng et al. (2015) and Gao et al. (2017) are more useful for defining  
742 mechanical impacts, failure moments, and the response of damaged structures. Coupled with  
743 rheological tests on DF material and validation against real case studies, model outcomes lead  
744 to a critical retrospective analysis of input parameters; e.g. using a Bayesian approach to

745 check model validity, enabling both scientists and end-users to assess hazards (Tierz et al.,  
746 2017; Charbonnier et al., 2018a). The use of well-constrained geological data and Bayesian  
747 Posterior Functions (BPFs), such as those described in Charbonnier et al. (2018b), allow the  
748 model user to calibrate and tune model-specific input parameters in order to obtain a best-fit  
749 flow simulation with the highest BPF scores. Careful use of such tools, e.g., Bayesian belief  
750 networks (Tierz et al., 2017), can provide valuable insights and assist in the hazard analysis  
751 process. The differences among BPFs give important information regarding how simulations  
752 mismatch observed flows, and gives a sense of the reliability of the model in hazard  
753 assessment.

754 Models that assess LH/DF extent and initiation conditions are challenging because their  
755 utilization requires hydrological conditions. LH/DF initiation depends on precipitation,  
756 lithology and weathering, slope angle and strength, pore pressure, and groundwater, all of  
757 which cannot be assessed in real time without dedicated equipment. Consequently, statistical  
758 and numerical models seek to estimate the probable flow volumes originating in source areas  
759 (Muñoz-Salinas et al., 2009a, 2010; Mead et al., 2016). Mead et al. (2016) combined shallow  
760 landslide and overland erosion models as well as a probabilistic measure of rainfall intensity-  
761 frequency-duration relationships. LH volume was controlled by a characteristic timescale  
762 relating deposit depth  $H$  to hydraulic diffusivity  $D_0$  in the ratio  $H^2/D_0$ . As a result, rainfall  
763 duration is the most important factor determining initial LH sediment volume (e.g., Van  
764 Westen and Daag, 2005).

765 Forecasting of LH/DF timing is critical for issuing hazard warnings, and is focused largely on  
766 rainfall as a triggering event. Rainfall duration-intensity thresholds have been used by  
767 Japanese and Chinese engineers to compute 'critical rainfall' able to trigger LH/DFs (Yu et  
768 al., 2015), but recent refinements in evaluating the role of rainfall have been made through the  
769 application of Bayesian methods to identify the probability of future events (Berti et al.,  
770 2012). Rainfall return periods (Destro et al., 2017) and probability rainfall intensity-  
771 frequency-duration curves (Mead and Magill, 2017) have been added to susceptibility models  
772 to delineate LH hazard zones probabilistically, using the calculated mobilized volumes as an  
773 input to shallow-layer flow models. SIG-based maps coupled with probabilistic analysis of  
774 susceptible areas, and rainfall duration and intensity thresholds, are automated to assess how a  
775 given parameter (landslide, slope angle, groundwater) may lead to DF triggering (Mead et al.,  
776 2017; Bauman et al., 2018). DF triggering processes were tested by studying natural DF  
777 events using rheological and field tests and/or numerical models (Sosio et al., 2007, 2011;  
778 Bauman et al., 2018). Numerical models were applied to terrain within a GIS framework to

779 simulate the physical behavior of LHs and to map their distribution and length. GIS was also  
780 used to estimate LH volumes, and methods utilizing field surveys and modeling were  
781 compared (Muñoz-Salinas et al., 2009a, 2010).

782 Forecasting debris-flow speeds and inundation areas commonly entails the use of physically  
783 based, deterministic flow dynamic simulations (Iverson, 2014). Models that describe flow  
784 mechanics can incorporate probabilistic components by adopting a range of plausible values  
785 for material properties and initial conditions, computing a corresponding range of possible  
786 outcomes (Córdoba et al., 2015, 2018). Probabilistic DF inundation forecasts can be  
787 accomplished by exploiting statistical patterns exhibited by prior events. Both channel cross-  
788 sectional areas and planimetric areas inundated by DFs in diverse settings are commonly  
789 proportional to flow volume raised to the power of 2/3 (Iverson, 2014). Statistically calibrated  
790 relationships of the form:  $\text{area} \propto \text{volume}^{2/3}$  thus can be used in algorithms that employ a range  
791 of hypothetical flow volumes and initiation sites to compute the limits of prospective  
792 inundation areas and display them on DEMs. Such algorithms can thereby generate  
793 gradational hazard zonation maps (Griswold and Iverson, 2008).

794

#### 795 **4. FLOW PROCESSES AND DAMAGE**

796

797 We review the ways by which lahars and debris flows can damage buildings, networks/  
798 lifelines and other infrastructure.

799

##### 800 **4.1 Flow physical processes and properties leading to impact**

801

802 LHs/DFs can denude slopes, bury floodplains, cause significant mortality and devastate  
803 property –maximum speeds surpass 10 m/s, runout distance can exceed 100 km, and volumes  
804 can reach  $\sim 10^9 \text{m}^3$  (Iverson, 2014). LHs and DFs generate more damage than floods for a  
805 given area because the dense solid-fluid mixtures moving at high velocities exert much  
806 stronger pressures and generate block collisions. Due to flow durations of 1–2 hours on  
807 average, followed by dewatering and induration spanning up to a few days, LH/DFs induce  
808 long-lasting hydrostatic effects (**Table 5**).

809 In many publications, the consideration of LH impact processes is restricted to dynamic  
810 pressure that results in mechanical failure, and inundation depth that induces physical actions  
811 (Wilson et al., 2014; Deligne et al., 2017). A few studies report details on the range of  
812 physical and non-physical mass flow properties that lead to destruction of valuables through

813 direct and indirect processes (e.g. Zanchetta et al., 2004; Toyos et al., 2007, 2008), namely  
814 energy transfer, forces, pressures, and the consequences of water or contaminant contact.  
815 **Table 5** that depict damage mechanisms reveals that LH/DF impacts are due to multiple  
816 direct and indirect processes imposed by unsteady behavior and changing dynamics during  
817 extended events. Furthermore, these processes are distributed unevenly across catchments. As  
818 a result, impacts to valuables result from a complex set of spatial and temporal variations in  
819 volume, velocity, solid concentration, particle-size distribution and segregation, pore-fluid  
820 pressure, dilatancy and solid-fluid interactions (Manville et al., 2013).

- 821 1. There is little difference between LHs and DFs in terms of damage processes except for  
822 temperature. However, viscosity in hot, syn-eruptive LHs can increase if flows are cohesive  
823 (Scott, 1988; Bardou et al, 2007). Hence, the dynamic pressure of viscous flows likely  
824 increases, leading to larger amounts of damage.
- 825 2. Hydrodynamic pressure, influenced by turbulence, increases logarithmically with velocity  
826 during an impact (Zanchetta et al., 2004). Pressure exerted on structures induces wall  
827 deformation and failure. Upon building failure, roofs can collapse and material can  
828 disaggregate and be removed by flows.
- 829 3. Deposition induces long-lasting burial and subsequent induration depending on the  
830 concentration of fine-grained material (Armanini, 1997). Accumulation of flow material may  
831 block doors and prevent evacuation of residents. Recurrent or high rate deposition leads to  
832 prolonged burial and suppresses soil infiltration.
- 833 4. Flow depth and mass trigger hydrostatic pressure, which persists longer than hydrodynamic  
834 pressure, acting either normal or lateral to the obstacle – from depth differential between the  
835 inside and outside of buildings – and vertical upon burial (Mead et al., 2017).
- 836 5. Buoyancy of the viscous and dense fluid/solid mixture can lift up edifices, which is usually  
837 followed by capillary rise, hence dampness can soak and weaken the structure, and deform  
838 construction materials of low density (Talon et al., 2012).
- 839 7. Soil or substrate can deform under foundations and further increase capillary rise from  
840 below.
- 841 8. The duration of the flow, or residence time within the invaded structure, will eventually  
842 soak and weaken material, in particular wooden structures due to water infiltration.
- 843 9. Erosion processes undercut or scour buildings and bridge foundations. Removal of soil  
844 under edifices leads to deformation by edifice load. Flows can also remove protruding house  
845 elements.

846 10. Boulders act as missiles, inducing dynamic and erosion processes. Block and boulder  
847 impacts lead to wall, pillars and roof deformation, particularly if impacts are repeated. Block  
848 impacts creating cavities in edifices may lead to collapse.

849 11. The temperature of hot, primary LHs can also cause injuries and affect some structures.  
850 Hot LHs weaken wood and fragile elements, scald people, burn inflammable tissues and  
851 corrode structures.

852 12. Non-physical processes, such as chemical or biological reactions from hot LHs, low pH  
853 water, spillover from industrial plants, all contribute to weaken structures and cause delayed  
854 deformation. Low pH material may corrode metal, and badly affects crops and soil fertility.

855

## 856 **4.2 Forces, regime and dynamics of impact**

857

858 LHs and DFs exert impacts on structures, with pressure and inundation depth being the key  
859 parameters of hazard intensity used to better define physical impacts (Zanchetta et al., 2004;  
860 Mead et al., 2017). Hydrodynamic pressure exerted by an incompressible fluid flow is  
861 proportional to velocity squared (Faella and Nigro, 2003; Federico and Amoruso, 2008), and  
862 together with the hydrostatic force (Armanini, 1997), represents the impulsive action at the  
863 flow front.

### 864 **4.2.1 Forces that exert impacts**

865 Damage is induced by a combination of three principal forces: (1) hydrodynamic pressure, (2)  
866 hydrostatic pressure, and (3) the collisional force of boulders (Xianbin et al., 2016; He et al.,  
867 2016; Ng et al., 2016; Huang Y. et al., 2017).

868 1. Hydrodynamic pressure ( $kPa$ ), having horizontal and vertical components, is the kinetic  
869 energy per unit volume of the flow, which changes with flow density. Dynamic pressure is  
870 mostly a function of flow speed and density. It is complicated to analyze as dynamic pressure  
871 depends on the flow mixture, the geometry and volume of the flow, and the characteristics of  
872 obstacles. Material inhomogeneity creates important variations in the impact force with time,  
873 while the presence of boulders increases local pressures (Bugnion et al., 2012a). The impact  
874 pressures are not determined by flow height, but correlated with the square of the front speed,  
875 which in turn depends on the grain-size distribution and water content.

876 The ratio of the hydrodynamic pressure to the momentum flow density, i.e. the product of DF  
877 density and mean velocity squared, was tested in Chinese examples. Hu et al. (2011)  
878 constructed an experimental system using three strain sensors implemented at different flow

879 depths, within the natural laboratory of the Jiangjia ravine, a well-studied experimental site  
880 dubbed the ‘debris museum’ in SW China. The system recorded for the first time long-lived  
881 and real time impact forces associated with 38 large DF surges that occurred in 2004. The  
882 authors found that the peak particle impacts at different depths were non-synchronous, and  
883 that the impact loadings were far greater than, but not proportional to, fluid pressures.

884 2. Hydrostatic pressure ( $kPa$ ), depends on the weight of the wet flow until it solidifies, and  
885 acts towards the end of the event once the deposit is stabilized. LH and DF hydrostatic  
886 pressures depend on the flow depth. Hydrostatic pressures can be much higher than the pure  
887 water pressure. This force weakens structures (especially joints in masonry), and plays an  
888 extended role in damage assessment (Mead et al., 2017) in addition to the instantaneous  
889 dynamic pressure.

890 3. Boulders act as missiles, hitting structures and obstacles (Zanchetta et al., 2004).  
891 Collisional forces depend on the concentration of boulders, particularly at the flow front and  
892 at the channel bends, and on the flow velocity (e.g., Martinez et al., 2011). The kinetic energy  
893 produced by the impact of a boulder is a function of the boulder’s mass and terminal velocity  
894 (Mavrouli and Corominas, 2010), and thus, the total energy impacting the structure includes  
895 the addition of the kinetic energy of every boulder. More commonly, the total pressure  
896 exerted by the boulders  $q_e$  is described as:

$$897 \quad q_e = Q_e / A \quad (5)$$

898 where  $Q_e$  is the equivalent static force ( $kN$ ) estimated for a runoff velocity of  $1 \text{ m}\cdot\text{s}^{-1}$  and an  
899 impact surface area ( $A$ ) of  $0.9 \text{ m}^2$  (Talon et al., 2012).

900 Secondly, the hydrostatic force due to flooding  $q_{he}$  is:

$$901 \quad q_{he} = \rho_f \cdot g \cdot (h_f + h_e) \quad (6)$$

902 where  $q_{he}$  is the hydrostatic force,  $\rho_f$  the density of flow,  $h_f$  flow height,  $h_e$  height of building  
903 foundation and  $g$  gravitational acceleration (Talon et al., 2012).

904 Then, the total pressure exerted by a flow on an obstacle is then given by:

$$905 \quad P_t = (1/2)\rho gh + \rho v^2 \quad (7)$$

906 where  $(1/2)\rho gh$  is the mean hydrostatic pressure and  $\rho v^2$  the dynamic overpressure member  
907 (Zanchetta et al., 2004).

908

### 909 *Impact regimes*

910 Two impact regimes can be distinguished in the incident flow hitting a rigid structure (Fig.

911 **6A-B**): either a vertical jet-like bulge or a wave that propagates upstream (Armanini and

912 Scotton, 1993). Under both regimes the dynamic overpressure is proportional to the square of

913 the frontal velocity as shown by two equations (Armanini and Scotton, 1993; Zhang, 1993;  
914 Coussot, 1997):

$$915 \quad Pdy = k\rho dfv^2 \quad (8)$$

916 where  $Pdy$  is dynamic pressure,  $k$  is a constant, which depends on the density of the granular  
917 material, flow dynamics and flow homogeneity and constituents,  $\rho df$  is the mean density of  
918 the mixture, and  $v$  is the velocity of the flow front (Toyos et al., 2008), and:

$$919 \quad p_{max} = k \cdot p_{Mu} \cdot g \cdot h_{Mu} \quad (9)$$

920 with  $P_{max}$  being the maximum debris flow impact pressure in N,  $k$  an empirical factor,  $h_{Mu}$   
921 the flow density in  $\text{kg/m}^3$ ,  $g$  gravity in  $\text{m/s}^2$ , and  $h_{Mu}$  flow height in m. The empirical factor  $k$   
922 is in the range of 1 to 13 for different models (Hübl et al., 2009).

923 In contrast, hydrodynamic pressure formulas have the appearance:

$$924 \quad P_{max} = a \cdot \rho_{Mu} \cdot v \quad (10)$$

925 with  $p_{max}$  being maximum flow impact pressure in N,  $a$  an empirical factor, and  $v$  the velocity  
926 of the flow in  $\text{m/s}$ . The empirical factor  $a$  depends on the flow type. Hu et al. (2011)

927 compared hydrodynamic models with data measured during real-time load sensor tests in the  
928 experimental site of Jiangjia Ravine in China. A general form of the impact pressure, which is  
929 related to the hydrodynamic force, is:

$$930 \quad P = k\rho v \text{ or } P = k\rho v^2 \cos^2 \theta \quad (11)$$

931 where  $P$  is the dynamic pressure in  $\text{N.m}^{-2}$ ,  $v$  the flow velocity,  $\theta$  the angle between the  
932 direction normal to the face of the barrier and the flow direction, and  $k$  an empirical factor  
933 depending on the flow type (Zeng et al., 2015). Hu et al. (2011) summarized a list of seven  
934 formulae elaborated by several authors to define the pressure  $P$  ( $\text{N m}^{-2}$ ) as follows:

935

$c_d \rho v^2 \sin \varphi$	$c_s \rho g H$	$c_d \rho v^2 \cos^2 \alpha$	$0.5 \rho g H + \rho c v_c v$ ; $c_s \rho g H$	$c_m (0.5 \rho g H + \rho v^2)$	$5 \rho (g H)^{0.6} v^{0.8}$
$\rho g \cos \theta h + \rho g \sin \theta L_0 - \tau_0 L_0 / h + \rho / 2 v^2   \tau_{-L_0} + \rho v_f v  _{-L_0}$					(Eq. 12a- g)

936

937 The most significant parameters to account for include flow density  $\rho$ , velocity  $v$ , depth  $H$ ,  
938 gravity acceleration  $g$ , and  $\varphi$ , the angle between the flow direction and the obstacle. The  
939 coefficients  $c_d$ ,  $c_s$  and  $c_m$  are dimensionless and describe hydrodynamic, hydrostatic and  
940 mixed models. What also matters, albeit less accounted for in studies, are the shock wave  
941 velocity  $v_c$ , the yield stress  $\tau_0$ , the slope angle  $\theta$ , the speed of the flow front  $v_f$ , the maximum  
942 density  $\rho_c$  of the impacting DF, the angle  $\alpha$  between the flow direction and the direction  
943 normal to the impacting plane, and the flow depth  $h$  at a distance  $L_0$  from the obstacle. This

944 second set of parameters has been identified using load impact sensors in a small number of  
945 experimental sites (Proske et al., 2011; Bugnion et al., 2012b; Canelli et al., 2012), but have  
946 not yet been applied to risk assessment.

947

#### 948 *Impact dynamics*

949 Lahar/debris flow impact dynamics depends on the kinetic characteristics of the flow, hence  
950 the Froude number  $F$  (see section 2.1) is a key parameter that directly influences the  
951 calculated dynamic pressure at which the flow front hits an obstacle.  $F$  reflects the contrasted  
952 behavior of subcritical ( $<1$ ) and supercritical ( $>1$ ) flows, which exert fundamentally different  
953 impact forces. Another mechanical reason is that a liquid-granular wave hitting a vertical  
954 obstacle produces two different impact dynamics (Armanini et al., 2011): having high-  
955 velocity fronts, supercritical DFs are deviated in the vertical direction, producing a vertical  
956 jet-like bulge, whereas subcritical DFs with low-velocity fronts are reflected in direction  
957 normal to the obstacle. This contrast has profound consequences on the exposure of obstacles  
958 with respect to incoming flows.

959 Tiberghien et al. (2007) and Armanini et al. (2011) experimentally unravelled impact  
960 dynamics by examining the relationship between  $F$  and the formation of the dead zone (**Fig.**  
961 **6B**). A ‘dead zone’ located in the internal corner of a building between the floor and the  
962 vertical wall (**Fig. 6A**) is an area where a total absence of mobility is due to yield stress. At  
963 this location, shear rate at the bottom of the flow diminishes and fluid is trapped. Two  
964 different impact regimes were observed: (1) for a subcritical flow, a slow increase of the  
965 dynamic pressure led to a maximum that corresponds with the stabilization of the dead zone  
966 (**Fig. 6A**), and (2) for a supercritical flow, a sharp increase and decrease in the dynamic  
967 pressure coincides with the formation of a jet. In both cases, the maximum dynamic pressure  
968 increased and was reached when the dead zone was entirely developed (**Fig. 6B**). Hübl et al.  
969 (2009) and Proske et al. (2011) explored the role of the  $Fr$  number in relation to both  
970 hydrodynamic and hydrostatic pressure using analogue experiments and natural channels  
971 (**Fig. 7**). They found that the use of  $Fr$  did not reconcile the miniaturized impact tests with  
972 real world DF impacts, revealing that miniaturized tests underestimate hydrodynamic  
973 pressures.

974 Kattel et al. (2018) categorized the impact pressure  $P$  of a DF on an obstacle into three phases  
975 according to the three flow segments: (i) strong and rapid  $P$  during the sudden impact of the  
976 coarse head, (ii) steady  $P$  of the debris body, and (iii) slight static pressure of the debris tail. In

977 quasi-static flows or hydrostatic models, the maximum DF pressure ( $P_H$ ) on an obstacle was  
978 calculated as:

$$979 P_H = k\rho_mgh \quad (13)$$

980 where  $k$  is an empirical factor depending on the dynamic behavior of the DF,  $\rho_m$  is the mixture  
981 density and  $h$  is the total depth of the debris mixture. The hydrodynamic model for rigid  
982 obstacles calculates the dynamic pressure ( $P_D$ ) of the DF as:

$$983 P_D = C_0\rho_m v_m^2 \quad (14)$$

984 where  $v_m$  is the velocity of the debris mixture.  $C_0$  is a factor describing the influence of the  
985 shape of the obstacle and is generally taken to be 0.5, but can range between 0.4 and 10  
986 (Bugnion et al., 2012a,b; Cui et al., 2015). Uncertainties thus abound in calculating the  
987 pressure of a DF impacting a structure. The case of DFs hitting an obstacle at some angle is  
988 still very poorly understood as it is very difficult to estimate the actual surface area of the  
989 obstacle hit by debris during the flow. Kattel et al. (2018), following Cui et al. (2015), thus  
990 estimated the dynamic impact pressure as:

$$991 P_D = \rho_m v_m^2 \sin^2\theta \quad (15)$$

992 where  $\theta$  is the acute angle between the direction of the DF and the surface of the obstacle that  
993 is impacted. In Eq. 15,  $\sin^2\theta$  arises because the authors replaced  $v_m^2$  by its component  $v_m^2 \sin^2\theta$   
994  $\sin^2\theta$  in the direction of impact, with the upstream surface of the obstacle measured from the  
995 normal direction.

996

#### 997 ***4.2.2 Impact dynamics and flow regime in space and time***

998

999 Impacts will differ in space and time according to the sections of the flow (head, body or tail)  
1000 that encounter an obstacle. Previous studies incorporating the impact force assumed a constant  
1001 value. But in reality both laboratory experiments and back analysis reveal that the impact  
1002 force evolves with the flow sections, within the flow head itself, and vertically within the  
1003 flow. Using miniaturized experiments to record the impact dynamics of viscous DFs against  
1004 obstacles, Cui et al. (2015) described both *the chronology and the location of evolving*  
1005 *damage processes*.

1006 Firstly, the detailed chronology included three steps: (1) the bottom of the structure is  
1007 damaged first when it is submitted to the maximum impact pressure, located at the lowermost  
1008 third of the flow depth, (2) the structure is damaged sustainably due to the continuous  
1009 dynamic pressure, with a maximum stress point at two thirds of the depth, and (3) the

1010 discharge and velocity of the DF decreases triggering deposition, which subsequently creates  
1011 damage by burial and infiltration.

1012 Secondly, Cui et al (2015) divided the impact processes of DFs into three phases by analyzing  
1013 variations of impact signals in conjunction with flow regimes. These authors introduced the  
1014 power function relationship  $\alpha$  and the Froude number for DFs, and proposed a universal  
1015 model for calculating dynamic pressure. The peak impact pressure of particles at different  
1016 flow depths was 40–160 kPa, which was about  $3 \pm 1.5$  times the impact pressure of the slurry  
1017 at the bottom of the flow, and about 2.5–4.5 times that of the flow in the middle, and at the  
1018 surface. The differences in impact frequency indicate that most of the large particles  
1019 concentrate in the DF head, and the number of particles in the DF head increases with flow  
1020 height. This agrees with Federico and Amoroso (2008) who proposed a theoretical and  
1021 numerical analysis of impact pressure.

1022 Analytical or numerical studies considering the evolution with time of the impact force  
1023 against an obstacle are now being conducted by cutting-edge finite element methods (e.g., Li  
1024 et al., 2017; Kwan et al., 2018). To study the dynamic response of structures to DFs, finite  
1025 element models of different masonry edifices were established by means of LS-DYNA  
1026 software. LS-DYNA, used to simulate boulders in DFs, is a general explicit dynamic finite  
1027 element analysis program capable of simulating complex real-world problems. It is especially  
1028 suitable for coping with fluid–solid interaction problems and nonlinear collision problems.

1029

### 1030 **4.3 Analyzing the distribution of impacts**

1031

1032 In recent years, a wealth of small- and medium-scale experiments have been conducted on  
1033 both incoming flows and structures resisting their impacts (Zanuttigh and Lamberti, 2006; Cui  
1034 et al., 2015; Li et al., 2017; Gao et al., 2017), and validated through load sensor measurements  
1035 on natural or artificial obstacles (Wendeler et al., 2007; Hu et al., 2011; Bugnion et al.,  
1036 2012b). Many of these experiments were adapted from controlled, large-scale experiments  
1037 considering snow avalanche impacts in laboratory and natural sites (e.g., WLS in Davos,  
1038 Switzerland; De Biagi et al., 2015). Two research directions were taken: (1) relationships  
1039 between the statistical distribution of damage and flow characteristics, and (2) the distribution  
1040 of dynamic pressures over an area affected by these flows.

1041 1. The statistical and probabilistic analysis of damage is a response to challenging theoretical  
1042 predictions of impact pressure and discharge due to limited field data at the local scale. Using  
1043 probabilistic analyses, Hong et al. (2015) measured the maximum impact pressure ( $P_{max}$ ) and

1044 total discharge ( $Q_{tot}$ ) of a set of 139 DF events over the period 1961–2000 in the Jiangjia  
1045 Ravine, China. The authors distinguished continuous (body) flows from instantaneous surge  
1046 (head) flows and found that: (1) The surge flow exhibited much higher values of  $P_{max}$  (744  
1047  $kPa$ ) and  $Q_{tot}$  ( $12,601m^3/s$ ), but these were much more variable than those of continuous  
1048 flows. (2) The Weibull and Gamma probability distributions were the most statistically  
1049 suitable for simulating the  $P_{max}$  of both surge and continuous flows, but only the Weibull  
1050 distribution was statistically suitable for simulating  $Q_{tot}$  of both flows. (3) Regressions  
1051 between  $P_{max}$  and  $Q_{tot}$ , established by means of power laws, suggested that  $Q_{tot}$  of a surge flow  
1052 had a stronger dependency on  $P_{max}$  than a continuous flow. Because discharge and impact  
1053 pressures of DF events strongly depend on the rainfall threshold, the authors suggested to  
1054 correlate the two parameters  $Q_{tot}$  and  $P_{max}$  with rainfall intensity, duration and return period.

1055 2. The second approach using SIG is illustrated by a computational, depth-integrated scheme  
1056 for estimating the impact pressure of a DF against buildings along the flow path in the  
1057 metropolitan Hong Kong (Gao et al., 2017). The calculation scheme, validated by flume tests,  
1058 employed a two-dimensional continuum model and considered building blockage effects, bed  
1059 erosion, and debris deposition, using a 3D high-resolution DEM, discretized into a grid of 5 m  
1060 square cells. The authors drew the following conclusions: (1) The presence of densely packed  
1061 buildings enlarged DF intensity significantly. The flow patterns were affected by the layout of  
1062 the buildings: the maximum flow depth and velocity around the buildings increased as the  
1063 debris tended to run up and deposit in front of the largest buildings while the flow path tended  
1064 to be narrowed due to building blockage; and (2) Large impact pressures developed on  
1065 building facades that faced the main path of the DF. These locations of stress concentration  
1066 corresponded to the largest perpendicular velocities.

1067

#### 1068 **4.4. Damage from lahars and debris flows**

1069 Based on field surveys, Zeng et al. (2015) distinguished three principal damage categories for  
1070 reinforced concrete and masonry structures by linking flow processes with hazard intensity  
1071 (Fig. 8): (1) Inundation or burial (Figs. 8-1 and -2) including damage to the ground floor or  
1072 external walls of a building together with debris entering rooms, but without significant  
1073 damage to structural components; (2) Serious structural damage owing to flow front impact or  
1074 boulder impacts triggering the failure of single structural elements (Figs. 8-3, -4 and -5), or  
1075 the collapse of the whole structure (Figs. 8-6 and -7); and (3) Undercutting where soil erosion  
1076 and/or liquefaction deforms foundations and subsequently buildings tilt or collapse (Figs. 8-8)  
1077 (Zeng et al., 2015). This dataset only included structures made of reinforced concrete (RC) or

1078 masonry; the impacts on other edifices and lifelines have not been adequately studied, except  
1079 from lahars around Merapi volcano (Jenkins et al., 2015). These authors studied the horizontal  
1080 failure pressure exerted on buildings, representing the impact pressure at which the resistance  
1081 of the wall was exceeded. The values found were 18 to 58 kPa for rubble stone buildings, but  
1082 much lower (2 to 7 kPa) for weak squared block masonry. The reason is that buildings were  
1083 mostly poorly constructed houses on the flank of the Merapi volcano, while the reinforced  
1084 structures analyzed by Zhang et al. (2007, 2018) in China were more robust, mostly RC  
1085 buildings resisting impact pressures up to 90 kPa. Most structures impacted by LHs in  
1086 developing countries are similar to those at Merapi, and so more vulnerable.

1087 Faella and Nigro (2003) and Nigro and Faella (2008) stated that the severity of LH/DF  
1088 impacts largely depended on the orientation and structural types of edifices, and the kinetic  
1089 energy of flows (a function of velocity, density and Froude number). Collapse mechanisms of  
1090 RC and masonry buildings for a single impact load were divided into six categories (**Fig. 9**):

- 1091 1. The collapse of ground floor external walls that does not cause significant damage to the  
1092 columns and beams.
- 1093 2. Serious damage or collapse of a single structural element without the collapse of the whole  
1094 structure. Three plastic hinges form at the ends and/or at the midspan of RC columns.
- 1095 3. Serious damage and/or the collapse of the structure leading to the formation of two plastic  
1096 hinges at the top and bottom of the column. RC columns experience a free horizontal  
1097 displacement.
- 1098 4. Part of the building is translated as the consequence of the collapse of ground floor bearing  
1099 structures.
- 1100 5. Serious damage and/or the collapse of bearing walls at the ground floor that does not result  
1101 in the collapse of the overall structure. This consists of superposition at the ultimate state of  
1102 two resistant schemes: the bending-type resistant vertical scheme, related to the collapse  
1103 mechanism of the vertical panel with formation of three plastic hinges, and the shear-type  
1104 horizontally resistant scheme, related to the shear resistance of the horizontal panel of the  
1105 wall.
- 1106 6. Complete structural failure of the building resulting in collapse.

1107 Prieto et al. (2018) quantified the relationship between hazard intensity and building  
1108 performance. The structural characteristics bearing on the resistance of buildings to DF  
1109 hazards include: weight to breadth ratio ( $W/B$ ), structural yield ( $A_y$ ) and/or ultimate lateral  
1110 capacity ( $A_u$ ), and associated model parameters ( $\alpha_l$ , and  $\lambda$ ). The parameter  $\alpha_l$  was taken as  
1111 0.90 for unreinforced masonry low-rise (URML) buildings following the seismic design of

1112 structures in Italy. To compute this ultimate parameter for building resistance, a handful of  
1113 variables need to be collected in the field and from imagery: building height, length and  
1114 weight/breadth, inter-storey height, thickness and density of walls, slab weight over the floor  
1115 area ratio, the vertical axial stress on the base of walls, and masonry shear resistance (Prieto et  
1116 al., 2018).

1117 Based on this set of variables, DF 'force' can be computed as:

$$1118 \quad FDF = Kd (0.5\rho C_d B (hv^2)) \quad (16)$$

1119 This was combined with lateral building capacity functions to solve the momentum flux term  
1120 ( $hv^2$ ) for each damage state using a threefold gradient: complete, extensive, and moderate  
1121 damage, quantified by three equations  $hvc^2$ ,  $hve^2$  and  $hvm^2$  (Prieto et al., 2018).

1122 The maximum estimated values of LH impact pressure in Sarno, Italy ranged between 400  
1123 and 600 kPa, but rapidly decreased to about 100 kPa at a distance of between 500-1,500 m  
1124 from the alluvial fan apex (Zanchetta et al., 2004). The complete destruction of a building  
1125 required a pressure exceeding 90 kPa. Below this value, structures were generally heavily (35-  
1126 90 kPa) or moderately (<35 kPa) damaged. The required pressure to break a large single-  
1127 glazed window was as low as 1 to 2 kPa and it was little more than 3 kPa for a wooden door.  
1128 Therefore, an important point is that openings are the weakest points of buildings and are a  
1129 critical parameter to quantify in buildings surveys.

1130 Exploring collapse mechanisms further, Zeng et al. (2015) linked the models of Nigro and  
1131 Faella (2008) with the concentration of the flow and boulder size. The results suggested that  
1132 DF type, the size of particles in the flow, and the impacted location significantly influenced  
1133 the critical collapse conditions. By comparing the failure curves for both models, these  
1134 authors found that columns that were fixed at both ends were more resistant than columns  
1135 fixed only at the base, and that the critical velocity for a three plastic hinge collapse was twice  
1136 that of a two plastic hinge model. The failure curve representing a dilute HCF was far below  
1137 that of a viscous DF with a higher kinetic energy.

1138 It was also found that when the size of the boulders exceeded 0.5 m, the damage caused by  
1139 both viscous and dilute flows was similar. Thus, this critical 0.5 m size can determine if  
1140 impacts are due to the force of particles or to the pressure of LHs/DFs (Zeng et al., 2015).

1141 Differences in flow type may contribute to differences in critical failure conditions. Compared  
1142 to dilute flows in which boulders frequently move at the bottom of the flow, the boulders in  
1143 viscous DFs move in the middle or the top of the flow due to higher fine sediment  
1144 concentrations and stronger floating forces. For viscous DFs, columns are more vulnerable  
1145 when large boulders are concentrated in the lower half of the maximum depth, whereas for

1146 dilute/turbulent DFs, columns are more vulnerable when large boulders are concentrated in  
1147 the lower third.

1148

## 1149 **5. LAHAR AND DEBRIS-FLOW RISK ASSESSMENT**

1150

1151 To assess the physical vulnerability of valuables threatened by mass flows, scientists have  
1152 explored probabilistic approaches and calculated vulnerability and fragility functions within  
1153 the framework of Quantitative Risk Assessment (QRA). QRA was defined by Blong (2000)  
1154 and quoted by Aspinall and Blong (2015) as “a numerical estimate of the probability that a  
1155 defined harm will result from the occurrence of a particular event”. QRA applies to a wide  
1156 range of assets, including the social fabric and economic valuables, but the majority of QRAs  
1157 related to LH/DF impacts and damage have dealt with buildings and infrastructure. Wilson et  
1158 al. (2014, 2017) distinguished three categories of tools used for QRAs: (1) vulnerability  
1159 indicators, the properties of a system that provide information regarding susceptibility to  
1160 hazard impacts, (2) damage matrix, defines the probability of specific damage levels being  
1161 reached for a valuable at specific hazard intensity levels, and (3) fragility functions,  
1162 quantitatively estimate the probability of a damage state being exceeded as a function of  
1163 hazard intensity. Taking the DF hazard intensity parameter as computed by the momentum  
1164 flux, and estimating damage classes from post-event inventories of affected buildings, Jakob  
1165 et al. (2012) proposed a useful damage relationship (**Fig. 10**) expressed as a DF damage index  
1166 ( $I_{DF}$ ) that leads the way to damage probabilities, the basis for quantitative risk assessment.  
1167 In their review of physical vulnerability to DFs, Papathoma-Köhle et al. (2017) described  
1168 three tools: matrices, curves, and indicators. Vulnerability matrices are a semi-quantitative  
1169 method, with no need for ex-ante data or detailed information. Vulnerability curves proceed  
1170 from a quantitative method, which may “translate” a disastrous event into a monetary cost.  
1171 Fragility functions describe the range of possible damage outcomes and their associated  
1172 probability of occurrence (Figs. **11** and **12**).

1173 Most risk assessment research on mass flows have developed empirical vulnerability  
1174 functions that express a relationship between economic loss and hazard intensity (i.e. a loss-  
1175 intensity relationship, e.g., Zhang et al., 2018), while a reduced number of authors have  
1176 focused on fragility functions, i.e. the probability of damage-intensity relationships. Though  
1177 grounded in observed cause-effect relationships, empirical vulnerability functions are not  
1178 designed to predict the capacity of a building to withstand the physical impacts from LH/DFs,

1179 or the related uncertainties associated with modelling building performance as a function of  
1180 variable flow parameters.

1181 A more rigorous analysis based on a geo-mechanical approach, advocated by Prieto et al.  
1182 (2018), involves the development of fragility functions, i.e. damage-intensity functions that  
1183 model the probability of exceeding a damage state threshold for a given hazard intensity  
1184 parameter such as the momentum flux (see **Fig. 11** and subsection 5.2). Hence, damage state  
1185 probabilities provide the necessary foundation for estimating socioeconomic consequences  
1186 and can be used in conjunction with empirical loss data to derive quantitative risk  
1187 assessments. If we consider QRAs of LH/DF scenarios, both vulnerability and fragility  
1188 functions, expressed as probabilistic curves, can help assess losses caused by future  
1189 destructive flows.

1190

### 1191 **5.1 Physical vulnerability of buildings**

1192

1193 Physical vulnerability assessment of valuables is a key component for risk assessment, and  
1194 the physical vulnerability of a building depends on its structural characteristics. Building  
1195 vulnerability is defined as the ratio of the cost of repairing the damage and the value of the  
1196 building, or as the loss over the individual reconstruction value (Quan Luna et al., 2011). For  
1197 example Kang and Kim (2016) constructed physical vulnerability curves for different types of  
1198 buildings in Korea in order to devise a quantitative assessment of DF risk. They analyzed the  
1199 relationships between the degree of damage of 25 buildings and the intensity of 11 DF events  
1200 occurring in 2011 through field survey information, spatial data, and empirical formulae.

1201 Three different empirical vulnerability curves were obtained as functions of DF depth,  
1202 velocity, and impact pressure, to which viscosity can be added (Quan Luna et al., 2011). The  
1203 vulnerability function were further characterized according to the structural type of the  
1204 buildings. Most of the masonry buildings were completely destroyed or seriously damaged in  
1205 2011, attributed to a greater vulnerability of brick buildings to lateral loads. In the case of  
1206 non-RC buildings, complete destruction occurred with impact pressures greater than 30 kPa.  
1207 For RC buildings, slight damage occurred with impact pressures under 35 kPa (see Zanchetta  
1208 et al., 2004 for comparison). The impact pressures of DFs corresponding to slight damage to  
1209 RC buildings can result in complete destruction of non-RC buildings. The vulnerability curves  
1210 of non-RC buildings worsened with increasing flow depth, flow velocity, and impact pressure  
1211 more rapidly than those of RC buildings. However, the proposed vulnerability curves have  
1212 limitations because of the limited amount of data available in this study.

1213 In QRA, physical vulnerability is expressed as the degree of loss or damage to a given  
1214 valuable within an area affected by a hazard, which is a representation of the expected level of  
1215 damage (Quan Luna et al., 2011). Following this principle, a structural classification of  
1216 buildings was produced by Zuccaro (2013a) for Naples near to Vesuvius volcano, and adapted  
1217 to the case study of Arequipa at the foot of El Misti volcano in Peru (Vargas Franco et al.,  
1218 2010; Thouret et al., 2014b). This classification of nine construction types uses three  
1219 categories of criteria: 1) architecture, 2) historical growth stages, including construction  
1220 techniques throughout city districts, and 3) structural design, ping for buildings, infrastructure,  
1221 networks, and protection works.

1222 Dealing with exposure and response of buildings damaged by LHs around Merapi volcano,  
1223 Indonesia, Jenkins et al. (2015) elaborated building damage scales, following the empirical  
1224 vulnerability approach that links damage levels (i.e. reflecting LH hazard intensity including  
1225 velocity) with the range of impacts (determined by hydrodynamic and static pressures)  
1226 according to expected building resistance. This approach is similar to the physical  
1227 vulnerability curves inferred from the pattern of buildings damaged by tsunami (Tarbotton et  
1228 al., 2015). As a result, most weak masonry low-rise (i.e. WMLR) buildings on Merapi would  
1229 be destroyed by dilute HCFs with relatively low velocities (ca. 3 m/s) and pressures (ca. 5  
1230 kPa); however, the majority of stronger rubble stone buildings may be expected to withstand  
1231 higher velocities (up to 6 m/s) and pressures (up to 20 kPa). Impact pressures vary  
1232 significantly, predominantly linked to the thickness of walls and the strength of bonds  
1233 between mortar and blocks. These values at Merapi are much lower than those of RC masonry  
1234 and concrete buildings in Korea and Italy, but similar to figures calculated for WMLR in rural  
1235 Colombia and for brick walls of different thickness in the city of Arequipa (**Figs. 11B and**  
1236 **12**).

1237

### 1238 *5.1.1 Vulnerability indicators*

1239 Vulnerability indicators may be attributed to each valuable at risk. This approach includes the  
1240 selection of relevant indicators, the identification of variables, their weighting and their  
1241 aggregation in a vulnerability index. Results may be the basis for local vulnerability reduction  
1242 actions.

1243 For example, Thouret et al. (2013, 2014b) and Ettinger et al. (2015) assessed the physical  
1244 vulnerability of buildings and bridges to flash flood and HCF hazard in the city of Arequipa.  
1245 They used indicators such as building type, number of floors, percentage and type of openings  
1246 and roof type to assess the physical vulnerability using an indicator-based method. The study

1247 area was large (3015 city blocks), requiring much data. The authors solved the problem by  
1248 interpolating field surveys with the use of high-spatial resolution satellite images, this method  
1249 being ‘ideal’ for large Latin American cities where access is limited. Logistic regression  
1250 allowed these authors to examine the relationship of these indicators to damage recorded in  
1251 the wake of one disastrous event in 2013 in order to estimate damage probabilities. Although  
1252 more research is needed on the evaluation of parameters and their interactions, the method  
1253 employed by Ettinger et al (2015) demonstrated that by calculating damage probabilities,  
1254 vulnerability can be assessed for buildings that have not yet been sampled, as long as some of  
1255 their characteristics can be estimated via remote sensing and verified by direct observations.  
1256 This makes the method suitable for large urban areas with many buildings.  
1257 Vulnerability functions for buildings, expressed as curves, aim to relate thresholds to hazard  
1258 intensity, i.e. inundation depth and impact pressure (Zhang et al., 2018; Fig. **11A**). However,  
1259 ranges of flow depth and impact pressures vary widely. The proposed vulnerability curves  
1260 also have limitations: the types of damaged buildings should be diverse, building geometry  
1261 and direction must be considered, and different building codes apply in different countries.

1262

## 1263 **5.2 Fragility functions**

1264

1265 Fragility curves, representing the potential damage state related to the intensity of a given  
1266 hazard, are used for the probabilistic estimate of the structural resistance of a building affected  
1267 by a destructive flow. These curves are produced by the combination of structural damage  
1268 data, from reconnaissance studies or insurance assessments according to estimated losses, and  
1269 the LH/DF characteristics ( $h$ ,  $P$ ,  $v$  and  $\mu$ ), to which the momentum flux  $hv^2$  (Prieto et al.,  
1270 2018; Fig. **11B**) and the dynamic force per unit width  $v^2d$  may be added (Zhang et al., 2018).  
1271 Considering that the vibratory motion of a LH during an impact is comparable to the dynamic  
1272 response of simple structures to earthquakes, Haugen and Kaynia (2008) used the HAZUS  
1273 damage state probabilities to produce fragility curves for un-reinforced structures. Elaborating  
1274 on Haugen and Kaynia’s paper and implementing a ‘geo-mechanical’ methodology for  
1275 quantitative risk assessments, Prieto et al. (2018) developed fragility functions (see Eq. 16 and  
1276 Fig. 11A) that relate hazard intensity to the probability of structural damage, based on the  
1277 combined hydrodynamic forces of a DF event (hazard level: momentum flux  $hv^2$ , material  
1278 density and related flow characteristics including drag and impact coefficient) and the  
1279 inherent structural resistance of building typologies (building performance: yield strength,  
1280 ultimate lateral capacity and weight to breadth ratios).

## 1281 **5.3 Risk analysis based on impact metrics**

1282  
1283 Risk analysis is a move from impact and damage studies to cross-referencing hazard intensity  
1284 and damage categories with impact metrics. Impact metrics are determined through the  
1285 combination of hazard intensities and damage to valuables (**Table 6**). Post-disaster damage  
1286 identified from images and field surveys has been translated into a scale of damage ‘levels’ or  
1287 ‘intensities’ (Wilson et al., 2014, 2017) for the purpose of risk analysis. Typically, five damage  
1288 categories help rank hazard metrics such as DF/LH intensities, measured in kPa for dynamic  
1289 and hydrostatic pressure, m for inundation depth, and Joule for boulder collision. The following  
1290 section will assist in applying impact metrics to quantify damage and loss caused by LHs/DFs.

1291

### 1292 ***5.3.1 Critical depth–pressure curves for QRA***

1293  
1294 Quantification of building damage has proven to be difficult due to the complexity of flow  
1295 behavior (*hazard*), the varying number and type of buildings exposed to these flows  
1296 (*exposure*) and the uncertain susceptibility of buildings to their impacts (*vulnerability*).  
1297 Recently, Mead et al. (2017) quantified these matters in determining building damage, with  
1298 reference to a case study in the city of Arequipa, Peru. Numerical modelling was used to  
1299 investigate LH/DF properties that are important in determining the inundation area and forces  
1300 applied to buildings. Building vulnerability was quantified through the development of critical  
1301 depth–pressure curves based on the ultimate bending moment of masonry structures. Results  
1302 suggest that building strength plays a minor role in overall building losses in comparison to  
1303 the effects of building exposure and hydraulic characteristics of the flow.

1304

#### 1305 *Pressure actions and critical depth-pressure curves*

1306 The complexity of lahar flows within urban environments with intricate geometry and  
1307 obstacles means that broad generalizations and assumptions about flow dynamics, such as the  
1308 assumption of a ‘surge depth’, are often limited in their validity. Both hydrostatic and  
1309 dynamic pressures have been considered in bending moment calculations for Arequipa’s  
1310 buildings (Mead et al., 2017). The applied depth at the time of maximum pressure was used to  
1311 create depth-pressure combinations to determine building loss. Maximum depths generally  
1312 occurred at later times in the simulations when hydrostatic pressure may have equalised inside  
1313 and outside buildings.

1314 A critical depth-pressure curve is the contour where the ratio of applied pressure moment  
1315 equals the ultimate failure moment of a given masonry wall. The range of design compressive  
1316 stresses for each building typology for Arequipa is shown in **Figure 12**: it was obtained by  
1317 calculating the design compressive stress for every configuration of masonry compressive  
1318 strength ( $f_c$ ), wall thickness ( $b$ ) and thickness coefficient ( $kt$ ). Wall thickness was found to  
1319 have a large effect on building strength, which is consistent with observations of Jenkins et al.  
1320 (2015). Notably, the design compressive stresses were similar for building types that shared  
1321 the same simplified structural classes identified in Thouret et al. (2014b). Given these  
1322 similarities, Mead et al. used the simplified structural classes (A0, A, and B) from these  
1323 authors. The critical depth (i.e. hydrostatic pressure) and dynamic pressure required to  
1324 overcome the ultimate bending moment are:

$$1325 \quad Mu = (f_t + f_d) \frac{wb^2}{6} \quad (16)$$

1326 where  $f_t$  is the tensile strength of the masonry wall,  $f_d$  the design compressive stress acting on  
1327 the wall,  $w$  the width of the wall facing the flow, and  $b$  the thickness of the wall, which is  
1328 assumed equal to the brick width for each structural class, and shown in **Figure 12**. These  
1329 curves assume that both hydrostatic and dynamic pressure acts on walls. The curves in Figure  
1330 **12A** indicate the structural limit of each class; combinations of depth and pressure that fall  
1331 above the curves indicate an applied moment greater than the building can withstand, and  
1332 conversely, Figures **12B and C** show that the critical depth decreases with the density of  
1333 flows, as the hydrostatic pressure gradient is much larger for sediment-rich lahars. The critical  
1334 depths and pressures are also affected by the structural class, with A0 structures being much  
1335 less resilient than A and B structures. The depth-pressure curves assume a binary damage  
1336 state, where failure is total when the applied pressure moment equals the ultimate failure  
1337 moment. Most of the flow scenarios in this study caused depths and pressures that exceeded  
1338 critical curves by a large margin and resulted in an almost total loss; conversely, flow  
1339 scenarios that did not result in total or near-total losses usually had depth and pressure values  
1340 that were well below the critical curves.

1341

### 1342 **5.3.2. Fragility functions: depth-pressure curves**

1343 Development of fragility functions in the form of critical depth-pressure curves for building  
1344 classes within Arequipa helped provide insight into possible building losses and their cause.  
1345 Building vulnerability is largely controlled by economic, social, cultural and institutional  
1346 factors (Künzler et al., 2012), so the depth-pressure curves were necessarily specific to

1347 Arequipa building typologies. However, given sufficient data on building strength, depth-  
1348 pressure curves can be generated through the same approach and used to quantify masonry  
1349 building loss in terms of flow depth and pressure.

1350 Building losses in Arequipa (Figs. 12D, E) are caused by the intersection of LH hazard with  
1351 building exposure and vulnerability. Cost-benefit of a valuable is defined as the ratio of the  
1352 cost of repairing the damage and the value of a building, for example, or as loss over the  
1353 individual reconstruction value (Quan Luna et al., 2011). The simulated building loss for all  
1354 scenarios indicated that substantial losses can be expected in the event of inundation.

1355 Furthermore, LH depths and pressures obtained from simulations were much greater than  
1356 most buildings in the study area could withstand, even if retrofitting to improve structural  
1357 strength was undertaken. This suggests that, in this study area at least, building exposure and  
1358 LH hazard have a larger role in determining building loss than structural vulnerability.

1359

#### 1360 **5.4. Loss evaluation**

1361

1362 Loss can be defined as the amount of money needed for recovery after disaster (Grigg and  
1363 Heiweg, 1975) or the minimum compensation required for returning to the pre-disaster  
1364 welfare level (Hicks 1946; Freeman et al., 2014). Two categories of loss are: direct and  
1365 indirect, to which economists have added long-term socio-economic losses at a regional or  
1366 larger scale. Losses encompass human (and other organisms), and property, including  
1367 buildings and land. Although this review will not consider them, losses should also include  
1368 intangible, sociological, psychological and cultural valuables. Here, we focus on the direct  
1369 and indirect losses related to the structural damage of buildings, and strategic infrastructure  
1370 (roads and bridges), and lifelines (water and electricity networks.) Many loss estimates in the  
1371 wake of natural disasters have been rooted in insurance-industry practices developed by  
1372 insurance companies, but these studies are lacking in many lower-income countries where  
1373 insurance coverage tends to be low.

1374

##### 1375 **5.4.1 Direct and indirect loss assessment**

1376

1377 Liu and Li (2007), Li and Liu (2010), and Liu et al. (2009) proposed a damage assessment  
1378 method for DFs that claimed to be a holistic assessment of direct and indirect losses.

1379 Assessing loss due to DFs in Taiwan, Liu et al. (2009) advocated a simple threefold, GIS-

1380 based approach that consists of data collection, delineation of the affected area, and land use

1381 analysis. They calculated loss over two return periods: after one single event, and after  
 1382 different flow events. Liu et al. (2009) considered two broad categories of loss: (1) human life  
 1383 and (2) property that was divided into land loss and loss above the ground, which  
 1384 encompassed several subcategories: (a) ground surface property including houses, commerce  
 1385 and industry, (b) direct resources such as agriculture and forest, (c) tourism, (d) other  
 1386 productions, (e) transportation and hydraulic facilities, and (f) ‘other use’.

1387 Human life loss was calculated as follows:

$$1388 \quad HL = HLV \times N, \quad (18)$$

1389 where HL is human life assessed as human life value (HLV) (dollar per person), and  $N$ , death  
 1390 toll. Although the value of human life depends on several assumptions and varies according to  
 1391 socio-cultural perspectives, Liu et al. nevertheless evaluated human life to be in the order of  
 1392 0.8 million US dollar in 2009 for the case of DF fatalities in Taiwan. Among different types  
 1393 of loss, one of the most reported losses consisted of construction, termed building loss (BL, in  
 1394 US dollars):

$$1395 \quad \sum_{i=1}^N \sum_{j=1}^M BC_{ij} \times BA_{ij} \quad (19)$$

1396 where BC is the cost of the different floor areas in dollar/m<sup>2</sup> and BA is the area of the floor  $i$   
 1397 in the building  $j$  (Liu and Li, 2007; Li and Liu, 2010).

1398 As a result, total loss was computed as:

$$1399 \quad HL + LL \text{ (land loss)} + BL + CL \text{ (Agricultural use)} + FL \text{ (Forest use)} + THL \text{ (Transportation} \\ 1400 \text{ and hydraulic use)} + TL \text{ (Tourism use)} \quad (20)$$

1401 The result was incorporated into the probable (expected) loss:

$$1402 \quad \sum_{t=1}^{\infty} p(x_t) [\beta_t C_t] \quad t = 1, 2, 3 \dots \infty \quad (21)$$

1403 where  $p(x_t)$  is the probability distribution function of rainfall,  $\beta_t$ , the probability coefficient of  
 1404 a DF to occur under the given return period,  $C_t$  the total loss under a specified return period,  
 1405 calculated from Eq. 21 and  $t$ , the recurrence interval of rainfall.

1406 Some authors take into consideration not only direct disaster-induced economic losses, but  
 1407 pursue the inventory post-disaster, including indirect losses such as the production capacity  
 1408 loss rate (Li et al., 2018). They use macro-scale econometric models, such as input-output and  
 1409 Computable General Equilibrium (CGE), to simulate disaster impact propagation, and  
 1410 evaluate the resulting GDP losses. CGE models not only capture direct impacts caused  
 1411 through physical damage/loss of life, but also follow indirect, cascading or so-called higher  
 1412 order effects. They consider dynamic feedbacks that exist within an economy including price  
 1413 change, substitution and reallocation of scarce resources through time (McDonald et al., 2017).

1414 These authors presented one of the first attempts to assess the economic consequences of  
1415 disruptive volcanic impacts at a range of temporal and spatial scales using multi-regional and  
1416 dynamic computable general equilibrium modelling. They elaborated on many regional and  
1417 national scale impacts in terms of potential losses caused by three eruption scenarios at Mt.  
1418 Taranaki, New Zealand. This study can be exploited for further research on socio-economic  
1419 impacts of LHs/DFs in the short and long term. Economic effects considered included: (1) the  
1420 evacuation of people from affected valleys; (2) business and industry interruption, and  
1421 reduction of labor and capital for production; (3) damage or destruction to principal resources  
1422 (e.g. high value crops, irrigation systems, oil, gas and transportation), and; (4) recovery costs,  
1423 including clearing of tephra and LH deposits, reclamation of land and reconstruction. In  
1424 contrast, studies of LH impacts in Indonesia and the Philippines have shown that positive  
1425 impacts have also resulted from land burial, such as extraction activities and tourism after an  
1426 eruption (De Belizal et al., 2013), and has sometimes enhanced agricultural productivity in the  
1427 long term.

1428 Loss can be estimated in a simple way to offer engineering options for decision makers. Li et  
1429 al. (2013) calculated loss functions in one watershed affected by DFs in Taiwan based on  
1430 rainfall duration (in hours) and DF volume ( $10^5 \text{ m}^3$ ) using formulae from Liu and Li (2007),  
1431 Liu et al. (2009) and Li and Liu (2010). One comprehensive loss field encompassed curves  
1432 (rainfall duration x DF volume) defined by return periods from 25 to 1,000 years (**Fig. 13**).  
1433 According to the return periods of DF events, cost-benefit ratios for engineering designs can  
1434 be calculated and emergency decisions taken. For example, a common 24-hour rainfall  
1435 duration and a 50-year return period would determine a DF volume of  $39,000 \text{ m}^3$ , which  
1436 would cause a loss of 2.167 million US\$ for the Taiwanese case study. The planned  
1437 engineering budget can be compared to this expected loss to provide a cost-benefit estimate,  
1438 which would assist decision makers in choosing adequate designs in DF disaster-prone areas.  
1439 Loss can be modelled probabilistically and is mostly useful for insurance and government  
1440 planning purposes. Such models have not yet been developed for LH-driven damage, but  
1441 Magill et al. (2006) provided a methodological framework including the development of a  
1442 probabilistic volcanic loss model for ash fallout in the Auckland region, New Zealand.

1443

#### 1444 *5.4.2 Predictive loss functions*

1445

1446 Risk-based decisions play an ever more important role in natural hazard management and  
1447 there is growing interest in predictive loss functions that can help quantify damage potential.

1448 QRA of LHs/DFs requires the analyst to predict damage potential, which can be done using  
1449 proportional loss functions.

1450 Rheinberger et al. (2013) analyzed a dataset of 132 buildings that were damaged by a large  
1451 DF in Switzerland using a ‘double Generalized Linear Model’ adapted from the GLM  
1452 framework to model proportional loss functions. The standard GLM framework consists of  
1453 three components: (1) the loss function,  $\eta_i = X_i \times \beta$ , where  $X_i$  is a linear combination of  
1454 predictor variables for object  $i$ , and  $\beta$  is the corresponding vector of coefficients; (2) a  
1455 probability distribution of proportional loss from the exponential family; and (3) an invertible  
1456 link function  $g$  that maps the expected proportional loss  $E[y_i] = \mu_i$  onto the predictors so that  
1457  $g(\mu_i) = \eta_i$ . These estimated proportional loss functions may be used for various prediction  
1458 purposes including hazard mapping, landscape planning, and insurance pricing. The results  
1459 suggested that process intensity parameters, such as flow depth, flow velocity, and  
1460 interactions, are the most meaningful predictors of relative damage and proportional loss.

1461 Industrial and agricultural buildings tended to suffer higher losses than residential buildings  
1462 because they are usually single-storey edifices. Results found by Rheinberger et al. (2013),  
1463 with regard to building structural characteristics, are of particular interest because property  
1464 owners can retrofit them through self-protection efforts. Using the risk ratios for two models,  
1465 the damage to a building without local protection measures, such as sheet pilings or concrete  
1466 enforcements, was predicted to be 1.6–1.8 times as high as the damage to an otherwise  
1467 identical protected building. Similarly, the damage predicted to a concrete building was only  
1468 about 60% of the damage expected to an otherwise identical non-concrete building,  
1469 suggesting that structural adaptation to the local environment is an effective means of  
1470 reducing DF damage.

1471 Cross-validation tests suggested that proportional loss predictions generated with the DGLM  
1472 approach are precise. The authors proposed several ways to make use of proportional loss  
1473 predictions. First, modern GIS techniques allow for combining proportional loss functions  
1474 with hazard maps and databases of insurance contracts to create risk maps. Such risk maps  
1475 could allow hazard managers to identify at-risk areas and to prioritize among mitigation needs  
1476 based on damage potential. Second, private property insurers could use the loss predictions to  
1477 offer individualized contracts that better reflect each homeowner’s risk. State building  
1478 insurers could use these results to provide an overview of where house owners should  
1479 consider local protection measures.

1480 A simpler application of risk and monetary loss applicable to lahars was presented by  
1481 Rodriguez et al. (2017) for Cotapaxi volcano, Ecuador. An economic evaluation of the

1482 infrastructure above or close to historical LH deposits was undertaken to determine the values  
1483 of damages. Strategic resources included buildings and other constructions, highways and  
1484 hydroelectric plants and many other valuables. Indirect damage included loss in revenues of  
1485 water, food, energy and gasoline supply, among others. The total losses of such damages were  
1486 calculated to potentially reach about 17 billion US\$, representing as much as 16.8 % of  
1487 Ecuadorian GDP. Simultaneously, the construction of mitigation structures able to retain LHs  
1488 was calculated to be about 150 million US\$. The calculated benefit–cost ratio (1:114) was  
1489 significant and the authors therefore concluded that construction of mitigation structures was  
1490 the best choice for authorities.

1491

## 1492 **6. SUMMARY AND CONCLUSION**

1493

### 1494 **6.1 Lessons gleaned**

1495

1496 The principal lessons gleaned from our review are as follows:

- 1497 1. Because their volumetric sediment concentrations exceed 40%, maximum speeds surpass  
1498 10 m/s, and volumes can range up to  $\sim 10^9 \text{m}^3$ , LH destructive power ranks second after PDCs  
1499 in volcanic environments worldwide. DFs and shallow landslides rank third after earthquakes  
1500 and floods in terms of overall natural hazard fatalities and economic loss.
- 1501 2. Arrays of methods implemented in the field and laboratory settings help monitor hydraulic  
1502 characteristics, rheological properties and flow impacts with obstacles. Mechanical testing of  
1503 flow deposits and construction materials, and numerical modelling help understand how  
1504 LHs/DFs behave.
- 1505 3. Critical conditions enabling LH/DF events to cause damage at distances from the source  
1506 are: flow momentum and composition, grain-size distribution, bulking/debulking and  
1507 segregation that affect flow dynamics, channel morphology, and variability in flow  
1508 path/channel topography.
- 1509 4. Flow emplacement not only cause flooding and land burial, but also scouring and  
1510 undercutting, and chemical and thermal effects. Long-lasting inundations, besides the  
1511 structural quality of valuables, play a critical role in favoring hydrostatic pressure on  
1512 buildings, infrastructure, and lifelines.
- 1513 5. LH/DF damages are induced by three principal forces driving impacts: (1) hydrodynamic  
1514 pressure, both lateral and vertical components, (2) hydrostatic pressure, and (3) the collisional  
1515 forces of boulders acting as missiles.

1516 6. LH/DF impact dynamics depend on the kinetics of flows, hence the Froude number. Two  
1517 impact regimes can be distinguished in the incident flow upon impacting a rigid structure,  
1518 governing the hydrodynamic pressure. Flow density, velocity, depth, and the least angle  
1519 between the flow direction and an obstacle are the significant parameters to account for the  
1520 impact pressure.

1521 7. Damage mechanisms are complex in space and time. The severity of damage and the  
1522 collapse mechanisms of buildings due to LH/DF impacts mostly depend on the position and  
1523 structure of buildings with respect to the impact direction and the kinetic energy of the flow.  
1524 Three principal damage categories for reinforced concrete or masonry structures were  
1525 distinguished by linking flow processes with hazard intensity: (1) inundation or burial  
1526 damage; (2) major structural damage owing to flow front impact and collisions from boulders,  
1527 and (3) undercutting when soil erosion and/or liquefaction deforms the foundations.

1528 8. Vulnerability assessment methods combine damage and intensity, resulting in measures of  
1529 damage states and probabilities. Fragility functions that combine hazard intensity parameters  
1530 with building and infrastructure performance provide reliable models in quantitative risk  
1531 assessment.

1532 9. Despite remarkable advances, our understanding of LH and DF behavior is far from  
1533 complete. Uncertainties plague hazard evaluation, exposure assessments, and the calculation  
1534 of potential loss.

1535 10. Hazards and impacts from LH/DFs are closely related to socio-cultural factors. The most  
1536 effective technology and mitigation procedures must be selected with local socio-cultural  
1537 characteristics in mind.

1538

## 1539 **6.2. Best practices and the Human factor**

1540

1541 Strategies to mitigate damage or loss from LHs and DFs, aptly summarized by Pierson et al.  
1542 (2014), encompass four categories: (1) avoidance of hazards through land-use planning  
1543 especially for dense population concentrations, (2) modification of hazards through  
1544 engineered protection structures; (3) establishment of warning systems to enable evacuations,  
1545 and; (4) effective response to LH/DFs when they do occur. Pierson et al. (2014) argued that  
1546 the human and institutional factors leading to successful application of these strategies can be  
1547 even more important: (a) engagement of all stakeholders in hazard education and risk-  
1548 reduction planning; (b) good communication of hazard and risk information between all  
1549 actors, (c) sustained response training, and (d) adequate funding for risk-reduction efforts. LH

1550 risk-reduction efforts cannot be effectively accomplished without the active involvement of  
1551 scientists working in partnership with local people including elected officials and emergency  
1552 managers.

1553 We emphasize that engineered protection structures, although desirable in general, can lead to  
1554 counterproductive effects. Key lessons were gleaned for future hazard mitigation in valleys  
1555 subject to confined versus valley-escaping mass flows. To decrease the chances for avulsion  
1556 from large LHs/DFs, check dams in confined and sinuous channels should be removed to  
1557 widen and deepen the valley, curved banks should be straightened and valley-filling  
1558 sediments should be removed. In contrast, novel constructions can modify hazards by  
1559 reducing intensities, thereby providing sustainable livelihoods. Li et al. (2017) proposed a  
1560 novel masonry structure with strong resistance to DFs using walls that are set with braces and  
1561 filled with straw bricks. Consequently, this design may benefit the sustainable development of  
1562 local communities in disaster-prone rural regions.

1563 What renders the analysis of LH/DF impact very complex is the fact that risk is closely  
1564 related to a combination of socio-cultural and economic factors, such as the exposure of  
1565 people and social vulnerability (Birkman, 2006). The most vulnerable populations tend to be  
1566 economically restricted to live in relatively inexpensive and more dangerous locations (Santi  
1567 et al., 2011). Space restrictions, often caused by expansion and development, force people to  
1568 live in topographically cramped areas, where they have limited influence and power to bring  
1569 about mitigation efforts. Especially in low-income countries, socio-cultural problems are as  
1570 important as technical choices in the effectiveness of hazard and risk-reduction efforts.

1571 Mitigation procedures that can enhance the chance of success are: (a) collaboration between  
1572 scientists, administrators and the local population, (b) advance warning to the highest degree  
1573 possible, and (c) interception and cleaning of debris in check dams.

1574

### 1575 **Acknowledgments**

1576 Our colleagues D.S. Hadmoko, Estuning W.T. Mei (Office of Natural Disaster Studies,  
1577 University Gadjah Mada, Yogyakarta, Indonesia), A. Solikhin (CVGHM, Bandung), and A.  
1578 Arguedas and J. Vásquez (INDECI, Defensa Civil) as well as UNSA students in Arequipa,  
1579 Peru have provided critical assistance in the field. This paper has greatly benefited from  
1580 constructive comments and valuable suggestions provided by Dr. Lucia Capra and Dr. S.  
1581 Charbonnier. This article is a CLERVOLC Labex contribution no. 372. This research was  
1582 funded by the French government IDEX-ISITE initiative 16-IDEX-0001 (CAP 20-25),  
1583 Challenge 4.

1584 **References**

- 1585 Ancey, C., 2007. Plasticity and geophysical flows: A review. *J. Non-Newt. Fluid Mech.* 142, 4  
1586 -35.
- 1587 Arattano, M., Marchi, L., 2008. Systems and sensors for debris-flow monitoring and warning.  
1588 *Sensors* 8, 4, 2436-2452.
- 1589 Arenas Lopez, M.A., 2017. Evaluación del riesgo producido por lahares del volcán Misti en el  
1590 entorno urbano de la ciudad de Arequipa, Perú. (Unpubl.) Trabajo fin de grado, Escuela  
1591 técnica superior de ingeniería de caminos, canales y puertos, Universidad de Granada, España,  
1592 178 p.
- 1593 Arguden, A.T., Rodolfo, K.S., 1990. Sedimentologic and dynamic differences between hot  
1594 and cold laharc debris flows of Mayon Volcano, Philippines. *Geol. Soc. Am. Bull.* 102, 865-  
1595 876.
- 1596 Armanini, A., 1997. On the dynamic impact of debris flows. Recent developments on debris  
1597 flows, pp. 208-224, *in*: Armanini, A., Michieu, M. (eds.), *Lecture Notes in Earth Sci.* 64,  
1598 Springer.
- 1599 Armanini, A., Scotton, P., 1993. On the dynamic impact of a debris flow on structures.  
1600 *Proceed. XXV IAHR Congress, Tokyo, Techn. Session B, Debris flows and landslides* 3,  
1601 203-220.
- 1602 Armanini, A., Larcher, M., Odorizzi, M., 2011. Dynamic impact of a debris flow against a  
1603 vertical wall. *Ital. J. Eng. Geol. Env.* 3B, 1041-1049.
- 1604 Aspinall, W., Blong, R.S. 2015. Volcanic Risk Assessment, pp. 1215-1234, *in*: Sigurdsson, H.  
1605 et al. (eds.), *Encyclopedia of Volcanoes*, 2nd edit., Academic Press-Elsevier,
- 1606 Auken, M.R., Sparks, R.S.J., Siebert, L., Crosweller, H.S., Hewert, J., 2013. A statistical  
1607 analysis of the global historical volcanic fatalities record. *J. Appl. Volc.* 2, 2, 1-24.
- 1608 Ballandras, S., 1993. Les crues torrentielles de l'été 1987 dans les Alpes françaises.  
1609 *Interprétation et enseignements. Rev. Géogr. Alpine* 81, 3, 13-32.
- 1610 Bänziger, R., Burch, H., 1990. Acoustic sensors (hydrophones) as indicators for bed load  
1611 transport in a mountain torrent. *IAHS Publ.* 193, 207-214, Lausanne.
- 1612 Barberi, F., Caruso, P., Macedonio, G., Pareschi, M.T., Rosi, M., 1992. Reconstruction and  
1613 numerical simulations of the lahar of the 1877 eruption of Cotopaxi volcano (Ecuador). *Acta*  
1614 *Vulcanol.* 2, 35-44.
- 1615 Bardou, E., Bowen, P., Boivin, P., Banfil P., 2007. Impact of small amounts of swelling clays  
1616 on the physical properties of debris-flow-like granular materials. Implications for the study of  
1617 alpine debris flows. *Earth Surf. Proc. Landf.* 32, 5 698-710.

1618 Baum, R.L., Godt, J.W., Savage, W.Z., 2010. Estimating the timing and location of shallow  
1619 rainfall-induced landslides using a model for transient, unsaturated infiltration. *J. Geophys.*  
1620 *Res.* 115, F03013.

1621 Bauman, V., Bonadonna, C., Cuomo, S., Moscariello, M., Manzella, I., 2018. Slope stability  
1622 models for rainfall-induced lahars during long-lasting eruptions. *J. Volc. Geoth. Res.* 359, 78-  
1623 94.

1624 Baxter, P.J., Horwell, C.J., 2015. Impacts of eruptions on human health. pp. 1035-1043, *in:*  
1625 Sigurdsson, H., et al. (eds.) *Encyclopedia of Volcanoes*, 2nd ed., Academic Press, San Diego.

1626 Beguería, S., Van Asch, Th.W.J., Malet, J.-P., Grondah, S., 2009. A GIS-based numerical  
1627 model for simulating the kinematics of mud and debris flows over complex terrain. *Nat. Haz.*  
1628 *Earth Syst. Sci.* 9, 1897-1909.

1629 Bellet, R., 1988. La crue du Saint-Antoine. *Bulletin Municipal de Modane*, Compagnie  
1630 générale des éditions officielles, Aix-en-Provence, 9-26.

1631 Berti, M., Martina, M.L.V., Franceschini, S., Pignone, S., Simoni, A., Pizziolo, M., 2012.  
1632 Probabilistic rainfall thresholds for landslide occurrence using a Bayesian approach. *J.*  
1633 *Geophys. Res.* 117, F04006.

1634 Bettella, F., Bisantino, T., D'Agostino, V., Gentile, F., 2012. Debris-flow runout distance:  
1635 laboratory experiments on the role of Bagnold, Savage and Friction numbers. *Monitoring,*  
1636 *Stimulation, Prevention and Remediation of Dense and Debris Flows IV*, 4, 27.

1637 Beverage, J.P., Culbertson, J.K., 1964. Hyperconcentrations of suspended sediment. *J. Hydr*  
1638 *Div, ASCE* 90, 117-128.

1639 Birkmann, J. (ed.), 2006. *Measuring Vulnerability to Natural Hazards. Towards Disaster-*  
1640 *Resilient Societies.* UNU Press, Tokyo, New York.

1641 Blong, R.S., 1984. *Volcanic hazards: a sourcebook on the effects of eruptions.* Academic  
1642 Press, Sydney, 484 pp.

1643 Blong, R.S., 2000. *Volcanic Hazards and Risk Management*, pp. 1215-1228, *in:* Sigurdsson,  
1644 H. et al. (eds.), *Encyclopedia of Volcanoes*, First edit., Academic Press, San Diego.

1645 Brown, S.K., Jenkins, S.F., Sparks, R.S.J., Odbert, H., Auker, M.R., 2017. Volcanic fatalities  
1646 database: analysis of volcanic threat with distance and victim classification. *J Appl. Volcanol.*  
1647 6, 15, 1-20.

1648 Bugnion, L., McArdell, B.W., Bartelt, P., Wendeler, C., 2012a. Measurements of hillslope  
1649 debris flow impact pressure on obstacles. *Landslides* 9, 179-187.

1650 Bugnion, L., von Boetticher, A., Wendeler, C., 2012b. Large scale field testing of hillslope  
1651 debris flows resulting in the design of flexible protection barriers. 12th Congress  
1652 INTERPRAEVENT 2012 Grenoble, France, Extended Abstracts, 59-66.

1653 Burtin, A., Hovius, N., McArdell, B., Turowski, J., Vergne, J., 2013. Seismic constraints on  
1654 dynamic links between geomorphic processes and routing of sediment in a steep mountain  
1655 catchment. *Earth Surf. Dyn. Disc.* 1, 1, 783-816.

1656 Caballero L, Capra L., 2014. The use of FLO2D numerical code in lahar hazard evaluation  
1657 at Popocatepetl volcano: a 2001 lahar scenario. *Nat Haz. Earth Syst. Sci.* 14, 12, 3345-  
1658 3355.

1659 Caliano, M., Ruin, I., Gourley, J.J., 2013. Supplementing flash flood reports with impact  
1660 classifications. *J. Hydrol.* 477, 1-16.

1661 Canelli, L., Ferrero, A.M., Migliazza, M., Segalini, A. 2012. Debris flow risk mitigation by  
1662 the means of rigid and flexible barriers – experimental tests and impact analysis. *Nat. Haz.*  
1663 *Earth Syst. Sci.* 12, 1693-1699

1664 Capra, L., Borselli, L., Varley, N., Gavilanes-Ruiz, J., Norini, G., Sarocchi, D., Caballero,  
1665 L., Cortes, A., 2010. Rainfall-triggered lahars at Volcán de Colima, Mexico: surface hydro-  
1666 repellency as initiation process. *J Volcanol. Geoth. Res.* 189, 1-2, 105-117.

1667 Cesca, M., D’Agostino, V., 2008. Comparison between FLO-2D and RAMMS in debris-flow  
1668 modelling: a case study in the Dolomites. *Monitoring, Simulation, Prevention and*  
1669 *Remediation of Dense Debris Flows II.* WIT Trans. Eng. Sci. 60, 197-206.

1670 Charbonnier, S.J., Macorps, E., C. B. Connor, L.J. Connor, J.A. Richardson, 2018a. How to  
1671 correctly evaluate the performance of volcanic mass flow models used for hazard assessment?  
1672 15-20, *in*: Thouret, J.-C. (dir.), Hazard and risk mapping – The Arequipa–El Misti case study  
1673 and other threatened cities. Presses universitaires Université Clermont-Auvergne, Territoires  
1674 H.-S. 1, 153 pp.

1675 Charbonnier, S.J., Connor, C.B., Connor, L.J., Sheridan, M.F., Oliva Hernández, J.P.,  
1676 Richardson, J.A., 2018b. Modeling the October 2005 lahars at Panabaj (Guatemala). *Bull.*  
1677 *Volc.* 80, 4.

1678 Chen, H.X., Zhang, L.M., 2015. EDDA 1.0: integrated simulation of debris flow erosion,  
1679 deposition and property changes. *Geosci. Model. Dev.* 8, 3, 829-844.

1680 Christen, M, Kowalski, J, Bartelt P, 2010. RAMMS: numerical simulation of dense snow  
1681 avalanches in three-dimensional terrain. *Cold Reg. Sci. Technol.* 63, 1-14.

1682 Cole, S. E., 2011. Geophysical investigation into the internal dynamics of moving lahars. PhD  
1683 dissertation, Massey University, Palmerston North, New Zealand.

1684 Cole, S., S. Cronin, S. Sherburn, S., Manville, V., 2009. Seismic signals of snow-slurry  
1685 lahars in motion: 25 September 2007, Mt. Ruapehu, New Zealand. *Geophys. Res. Lett.* 36,  
1686 L09405, 9.

1687 Cooley, M.E., Aldridge, B.N., Euler, R.C., 1977. Effects of the catastrophic flood of  
1688 December 1966, North rim area, eastern Grand Canyon, Arizona. *U.S. Geol. Surv. Prof. Paper*  
1689 980, 43.

1690 Córdoba, G, Villarosa, G, Sheridan, MF, Viramonte, JG, Beigt, D, Salmuni, G, 2015.  
1691 Secondary lahar hazard assessment for Villa la Angostura, Argentina, using Two-Phase-  
1692 Titan modelling code during 2011 Cordón Caulle eruption. *Nat. Haz. Earth Syst. Sci.* 15, 4,  
1693 757-766.

1694 Córdoba, G.A., Sheridan, M.F., Pitman, B.E., 2018. Titan2F code for lahar hazard  
1695 assessment: derivation, validation and verification. *Rev. Soc. Geol. Mexic.* 70, 3, 611-631.

1696 Costa J., 1984. Physical Geomorphology of debris flows, chap. 9, 268-317, *in*: Costa, J.,  
1697 Fleisher, P.J. (Eds.), *Developments and Applications of Geomorphology*, Springer-Verlag,  
1698 Berlin, 386 pp.

1699 Costa, J.E., 1988. Rheologic, geomorphic, and sedimentologic differentiation of water floods,  
1700 hyperconcentrated flows, and debris flow, pp. 268-317, *in*: Baker, V.R., Kochel, R.C., Patton,  
1701 P.C. (eds.), *Flood Geomorphology*, Wiley, New York.

1702 Coussot, P., 1997. *Mudflow Rheology and Dynamics*. Balkema, Rotterdam: Internat. Assoc.  
1703 Hydr. Eng. Res. Monograph, 255 pp.

1704 Coussot, P., Meunier, M., 1996. Recognition, classification and mechanical description of  
1705 debris flows. *Earth-Sci. Rev.* 40, 209 182-227.

1706 Coviello, V., Capra, L., Vázquez, R., Márquez-Ramirez, V-H, 2018. Seismic characterization  
1707 of hyperconcentrated flows in a volcanic environment. *Earth Surf. Proc. Landf.* 43, 10, 2219-  
1708 2231.

1709 Creutin, J.D., Muste, M., Bradley, A.A., Kim, S.C., Kruger, A., 2003. River gauging using  
1710 PIV techniques: a proof of concept experiment on the Iowa River. *J. Hydrol.* 277, 3-4, 182-  
1711 194.

1712 Cronin, S. J., Neall, V. E., 1997. A late Quaternary stratigraphic framework for the  
1713 northeastern Ruapehu and eastern Tongariro ring plains, New Zealand. *New Zeal. J. Geol.*  
1714 *Geophys.* 40, 185-197.

1715 Cronin, S.J., Neall, V.E., Lecointre, J.A., Palmer, A.S., 1996. Unusual “snow slurry” lahars  
1716 from Ruapehu volcano, New Zealand, September 1995. *Geology* 24, 12, 1107-1110.

1717 Cronin, J., Neall, V.E., Lecointre, J.A., Palmer, A.S., 1999. Changes in Whangaehu River  
1718 lahar characteristics during the 1995 eruption sequence, Ruapehu volcano, New Zealand. *J.*  
1719 *Volcanol. Geoth. Res.* 76, 47-61.

1720 Cronin, S.J., Lecointre, J. A., Palmer, A.S., Neall, V.E., 2000. Transformation, internal  
1721 stratification, and depositional processes within a channelised, multi-peaked lahar flow. *New*  
1722 *Zeal. J. Geol. Geophys.* 43, 1, 117-128.

1723 Crosta, G.B., Imposimato, S., Roddeman, D., 2009. Numerical modeling of 2-D granular step  
1724 collapse on erodible and nonerodible surface. *J. Geophys. Res., Earth Surf.* 114(F3), F03020.

1725 Cui, P., Zeng, C., Lei, Y., 2015. Experimental analysis on the impact force of viscous debris  
1726 flow. *Earth Surf. Proc. Landf.* 40, 1644-1655.

1727 D’Ambrosio, D., Di Gregorio, S., Iovine, G., Lupiano, V., Rongo, R., Spataro, W., 2003. First  
1728 simulations of the Sarno debris flows through Cellular Automata modelling. *Geomorph.* 54,  
1729 91-117.

1730 **De Bélizal, E., Lavigne, F., Hadmoko, D.S., Degeai, J.-P., Dipayana, G.A., Mutaqin,**  
1731 **B.W., Marfai, M.A., Coquet, M., Le Mauff, B., Robin, A.K., Cholikh, N., Nurnaning, A.**  
1732 **2013.** Rain-triggered lahars following the 2010 eruption of Merapi Volcano, Central Java,  
1733 Indonesia. *J. Volc. Geoth. Res.* 261, 330-347.

1734 De Biagi, V., Chiaia, B., Frigo, B., 2015. Impact of snow avalanche on buildings: Forces  
1735 estimation from structural back-analyses. *Engin. Struct.* 92, 15-28.

1736 De Haas, T., Braat, L., Leuven, J. R.F.W., Lokhorst, I.R., Kleinhans, M.G., 2015. Effects of  
1737 debris flow composition on runout, depositional mechanisms, and deposit morphology in  
1738 laboratory experiments. *J. Geophys. Res. Earth Surf.*, 120, 1949-1972.

1739 Delaite, G., Thouret, J.-C., Sheridan, M., Labazuy, Ph., Stinton, A., Souriot, T., Van Westen,  
1740 C., 2005. Assessment of volcanic hazards of El Misti and in the city of Arequipa, Peru, based  
1741 on GIS and simulations, with emphasis on lahars. *Zeit. Geomorph. N.F., Suppl. Vol.* 140,  
1742 209-231.

1743 Deligne, N.I., Horspool, N., Canessa, S., Matcham, I., Williams, G.T., Wilson, G., Wilson,  
1744 T.M., 2017. Evaluating the impacts of volcanic eruptions using RiskScape. *J. Appl. Volcanol.*  
1745 6, 18, 1-21.

1746 Destro, E., Marra, F., Nikolopoulos, E.I., Zocatelli, D., Creutin, J.D., Borga, M., 2017.  
1747 Spatial estimation of debris flows-triggering rainfall and its dependence on rainfall return  
1748 period. *Geomorphology* 278, 269-279.

1749 De Vekey, R.C. (ed.), 1996. RILEM TC 127-MS: Test for masonry materials and structures.  
1750 Rilem Technical Committees, Materials and Structures 29, 459-475.

1751 Devoli, G., Cepeda, J., Kerle, N., 2009. The 1998 Casita volcano flank failure revisited. New  
1752 insights into geological setting and failure mechanisms. *Engin. Geol.* 105, 1-2, 65-83.

1753 Dong, L., Shan, J., 2013. A comprehensive review of earthquake-induced building damage  
1754 detection with remote sensing techniques. *ISPRS J. Photogramm. Rem. Sens.* 84, 85-99.

1755 Dowling, C.A., Santi, P.M., 2014. Debris flows and their toll on human life: a global analysis  
1756 of debris-flow fatalities from 1950 to 2011. *Nat. Haz.* 71, 1, 203-227.

1757 Doyle, E.E., Huppert, H.E., Lube, G., Mader H.M., Sparks, R.S.J., 2007. Static and flowing  
1758 regions in granular collapses down channels: Insights from a sedimenting shallow water  
1759 model. *Phys. Fluids* 19, 10, 106601-106616.

1760 Doyle, E.E., Cronin, S.J., Cole, S.E., Thouret, J.-C., 2010. The coalescence and organization  
1761 of lahars at Semeru, Indonesia. *Bull. Volc.* 72, 8, 961-970.

1762 Doyle, E., Cronin, S.J., Thouret, J.-C., 2011. Cycles of bulking and debulking in lahars at  
1763 Semeru, Indonesia. *Geol. Soc. Amer. Bull.* 123, 1234-1246.

1764 Dumaisnil, C., Thouret, J.-C., Chambon, G., Doyle, E.E., Cronin, S.J., 2010. Hydraulic,  
1765 physical and rheological characteristics of rain-triggered lahars at Semeru volcano, Indonesia.  
1766 *Earth Surf. Proc. Landf.* 35, 573-590.

1767 Ettinger, S., Zeghdousi, M., Llerena, N.M., Yao-Lafourcade, A.-F., Thouret, J.-C., 2014.  
1768 L'apport de l'imagerie Pléiades à la cartographie des enjeux et de leur vulnérabilité face aux  
1769 crues torrentielles : la ville d'Arequipa, Pérou. *Rev. Franç. Photogram. Télédét.* 209, 74-77.

1770 Ettinger, S., Mounaud, L., Magill, C., Yao-Lafourcade, A.-F., Thouret, J.-C., Manville, V.,  
1771 Negulescu, C., Zuccaro, G., De Gregorio, D., Nardone, S., Uchuchoque, J. A. L., Arguedas,  
1772 A., Macedo, L., Manrique Llerena, N., 2015. Building vulnerability to hydro-geomorphic  
1773 hazards: Estimating damage probability from qualitative vulnerability assessment using  
1774 logistic regression. *J. Hydrol.* 541A, 563-581.

1775 Faella, C., Nigro, E., 2003. Dynamic impact of the debris flows on the construction during the  
1776 hydrogeological disaster in Campania 1998: 1. Description and analysis of the damage, 2.  
1777 Failure mechanical models and evaluation of impact velocity, *in*: Picarelli, L. (ed.), *Proc. Int.*  
1778 *Conf. on fast slope movements prediction and prevention for risk mitigation*, Patron, Bologna.

1779 Fagents, S. A., Baloga, S. M., 2006. Toward a model for the bulking and debulking of lahars.  
1780 *J. Geophys. Res., Solid Earth* 111, 21.

1781 Fan, R.L., Zhang, L.M., Wang, H.J., Fan, X.M., 2018. Evolution of debris flow activities in  
1782 Gaojiagou Ravine during 2008–2016 after the Wenchuan earthquake. *Eng. Geol.* 235, 1-10.

1783 Federico, F., Amoruso, A., 2008. Simulation of mechanical effects due to the impact of fluid-  
1784 like debris flows on structures. *Ital. J. Eng. Geol. Environ.* 1, 24 p.

1785 Fink, J.H., Malin, C.M., D'Alli, R.E., Greeley, R., 1981. Rheological properties of mudflows  
1786 associated with the spring 1980 eruptions of Mount St. Helens volcano, Washington.  
1787 *Geophys. Res. Lett.* 8, 1, 43-46.

1788 Freeman, A.M.III, Herriges, J.A., Kling, C.L., 2014. The measurement of environmental and  
1789 resource values, Theory and methods. Third edit., RFF Press, Routledge, New York, 459 pp.

1790 Gao, L., Zhang, L.M., Chen, H.X., 2017. Two-dimensional simulation of debris flow impact  
1791 pressures on buildings. *Eng. Geol.* 226, 236-244.

1792 George, D.L., Iverson, R.M., 2011. A two-phase debris-flow model that includes coupled  
1793 evolution of volume fractions, granular dilatancy and pore fluid pressure. *Ital. J. Eng. Geol.*  
1794 *Envir.* 43, 415-424.

1795 George, D.L., Iverson, R.M., 2014. A depth-averaged debris-flow model that includes the  
1796 effects of evolving dilatancy. II. Numerical predictions and experimental tests. *Proc. Royal*  
1797 *Soc. London, Ser. A*, 470, doi: 10.1098/rspa.2013.0820.

1798 Goodman, R.E., 1989. Introduction to rock mechanics. Second edit., New York, J. Wiley &  
1799 Sons, 562 pp.

1800 Graettinger, A.H., Manville, V., Briggs, R.M., 2010. Depositional record of historic lahars in  
1801 the upper Whangaehu Valley, Mt. Ruapehu, New Zealand: implications for trigger  
1802 mechanisms, flow dynamics and lahar hazards. *Bull. Volcanol.* 72, 279-296.

1803 Grattan, J., Torrence, R., 2007. *Living Under the Shadow: Cultural Impacts of Volcanic*  
1804 *Eruptions.* Left Coast Press, Walnut Creek, California, 307 pp.

1805 Grigg, N.S., Helweg O.J., 1975. State-of-the art of estimating flood damage in urban areas.  
1806 *Water Resour. Bull.* 11, 2, 379-390.

1807 Griswold, D.I., Iverson, R.M., 2008. Mobility statistics and automated hazard mapping for  
1808 debris flows and rock avalanches. U.S. Geol. Survey Scient. Invest. Report 2007-5276.

1809 Gudmundsson, M., 2015. Hazards from lahars and jökulhlaups, pp. 971-984, *in*: Sigurdsson  
1810 H. et al. (Eds.), *Encyclopedia of Volcanoes*, 2nd Edition, Academic Press-Elsevier.

1811 Haddad, B., Pastor, M., Palacios, D., Muñoz-Salinas, E., 2010. A SPH integrated model for  
1812 Popocatepetl 2001 lahar (Mexico): sensitivity analysis and runout simulation. *Eng. Geol.* 114,  
1813 312-329.

1814 Hampton, M. A., 1979. Buoyancy in debris flows. *J. Sediment. Petrol.* 49, 3, 753-758.

1815 Han, Z., Chen, G., Li, Y., Zheng, L., Zhang, Y., Xu, L.R., 2013. A numerical simulation of  
1816 volumetric enlargement for seismic debris flow using integrated DDA and KANAKO 2D,

1817 281-287, *in*: Chen, G.Q., Ohnishi, Y., Zheng, L., Sasaki, T. (eds), *Frontiers of discontinuous*  
1818 *numerical methods and practical simulations in engineering and disaster prevention*. CRC  
1819 Press, London.

1820 Han, Z., Chen, G., Li, Y., Wang, W., Zhang, H., 2015. Exploring the velocity distribution of  
1821 debris flows: an iteration algorithm based approach for complex cross-sections.  
1822 *Geomorphology* 241, 72-82

1823 Han, Z., Li, L., Huang, J., Chen, G., Xu, L., Tang, C., Zhang, H., Shang, Y., 2017a.  
1824 Numerical simulation for run-out extent of debris flows using an improved cellular automaton  
1825 model. *Bull. Eng. Geol. Environ.* 76, 961-974.

1826 Han, Z., Chen, J., Xu, P., Zhan, J., 2017b. A well-balanced numerical scheme for debris flow  
1827 run-out prediction in Xiaojia Gully considering different hydrological designs. *Landslides* 14,  
1828 2105-2114.

1829 Harris, A.J.L., Vallance, J.W., Kimberly, P.G., Rose, W.I., Matías, O., Flynn, L.P., Garbeil,  
1830 H., 2006. Downstream aggradation owing to lava dome extrusion and rainfall runoff at  
1831 Volcan Santiaguito, Guatemala. *Geol. Soc. Amer. Spec. Paper* 412, 85-104.

1832 Haugen, E.D., Kaynia, A.M., 2008. Vulnerability of structures impacted by debris flow, pp.  
1833 381-387, *in*: Chen et al. (eds), *Landslides and Engineered Slopes*, Taylor & Francis Group.

1834 Hayes, S.K., Montgomery, D.R., Newhall, C.G., 2002. Fluvial sediment transport and  
1835 deposition following the 1991 eruption of Mount Pinatubo. *Geomorphology* 45, 3-4, 211-224.

1836 He, S., Liu, W., Li, X., 2016. Prediction of impact force of debris flows based on distribution  
1837 and size of particles. *Environ. Earth Sci.* 75, 4, 298.

1838 Hicks, J.R., 1946. *Value and Capital: An inquiry into some fundamental principles of*  
1839 *economic theory*. Oxford, Clarendon Press, 364 pp.

1840 Hoeck, E., Brown, E.T., 1980. *Underground excavation in rock*. Institution of mineralogy and  
1841 metallurgy, London, pp. 527.

1842 Hong, Y., Wang, J.P., Li, D.Q., Cao, Z.J., Ng, C.W.W., Cui, P., 2015. Statistical and  
1843 probabilistic analyses of impact pressure and discharge of debris flow from 139 events during  
1844 1961 and 2000 at Jiangjia Ravine, China. *Eng. Geol.* 187, 122-134.

1845 Horton, P., Jaboyedoff, M., Rudaz, B., Zimmermann, M., 2013. Flow-R, a model for  
1846 susceptibility mapping of debris flows and other gravitational hazards at a regional scale. *Nat.*  
1847 *Haz. Earth Syst. Sci.* 13, 869-885.

1848 Hu, K., Wie, F., Li, Y., 2011. Real-time measurement and preliminary analysis of debris-flow  
1849 impact force at Jiangjia ravine, China. *Earth Surf Process Landf* 36, 1268-1278.

1850 Huang, C.-J., Shieh, C.-L., Yin, H.-Y., 2004. Laboratory study of the underground sound  
1851 generated by debris flows. *J. Geophys. Res.* 109 (F1), F01, 008.

1852 Huang, C.-J., Yin, H.-Y., Chen, C.-Y., Yeh, C.-H., Wang, C.-L., 2007. Ground vibrations  
1853 produced by rock motions and debris flows. *J. Geophys. Res. Earth Surf.* 112 (F2).

1854 Huang, Y., Cheng, H., Dai, Z., Xu, Q., Liu, F., Sawada, K., Moriguchi, S., Yasima, A., 2015.  
1855 SPH-based numerical simulation of catastrophic debris flows after the 2008 Wenchuan  
1856 earthquake. *Bull. Eng. Geol. Envir.* 74, 1137-1151.

1857 Huang Y, Cheng H, Dai, Z., Hu, K., Wei, F., Li, Y., 2017. Real-time measurement and  
1858 preliminary analysis of debris-flow impact force at Jiangjia Ravine, China. *Earth Surf. Proc.*  
1859 *Land.* 36, 1268-1278.

1860 Hubbard, B. E., Sheridan, M. F., Carrasco-Núñez, G., Díaz-Castellón, R., Rodríguez, S. R.,  
1861 2007. Comparative lahar hazard mapping at Volcan Citlaltépetl, Mexico using SRTM,  
1862 ASTER and DTED-1 digital topographic data. *J. Volcanol. Geotherm. Res.* 160, 99-124.

1863 Hübl, J., Suda, J., Proske, D., Kaitna, R., Scheidl, C., 2009. Debris Flow Impact Estimation.  
1864 International Symposium on Water Management and Hydraulic Engineering, Ohrid,  
1865 Macedonia, 1-5 September 2009, A56, 137-148.

1866 Hungr, O., 1995. A model for the runout analysis of rapid flow slides, debris flows, and  
1867 avalanches. *Can. Geotech. J.* 32, 4, 610-623.

1868 Hungr, O., 2008. Numerical modelling of the dynamics of debris flows and rock avalanches,  
1869 *Geomech. Tunn.* 1, 112-119.

1870 Hungr., O., 2010. DAN-W Release 10. Dynamic analysis of landslides. User's Manual. O.  
1871 Hungr Geotechnical Research Inc., Canada.

1872 Hungr, O., Jakob, M., 2005. Debris flows hazards and related phenomena. Praxis, Springer,  
1873 pp. 728.

1874 Hürlimann, M., Rickenmann, D., Medina, V., Bateman, A. 2008. Evaluation of approaches to  
1875 calculate debris-flow parameters for hazard assessment. *Eng. Geol.* 102, 3-4, 152-163.

1876 Itakura, Y., Kamei, N., Takahama, J., Nowa, Y., 1997. Real time estimation of discharge of  
1877 debris flow by an acoustic sensor, 127-131, *in: 14th IMEKO world Congress, New*  
1878 *Measurements—Challenges and Visions, Tampere, Finland, Vol. XA.*

1879 Itakura, Y., Inaba, H., Sawada, T., 2005. A debris-flow monitoring devices and methods  
1880 bibliography. *Nat. Haz. Earth Syst. Sci.* 5, 6, 971-977.

1881 Iverson, R.M., 1997. The physics of debris flows. *Reviews of Geophysics* 35, 3, 245-296.

1882 Iverson, R.M., 2014. Debris flows: behavior and hazard assessment. *Geol. Today* 30, 1, 15-20.

1883 Iverson, R.M., 2015. Scaling and design of landslides and debris flow experiments.  
1884 *Geomorphology* 244, 9-20.

1885 Iverson, R. M., George, D.L., 2014. A depth-averaged debris-flow model that includes the  
1886 effects of evolving dilatancy. I. Physical basis, *Proc. R. Soc. London, Ser. A*, 470, 20130819,  
1887 doi:10.1098/rspa.2013.0819

1888 Iverson, R.M., George, D.L., 2016. Modelling landslide liquefaction, mobility bifurcation and  
1889 the dynamics of the 2014 Oso disaster. *Geotechnique* 66, 175-187.

1890 Iverson, R.M., Schilling, S.P., Vallance, J.W., 1998. Objective delineation of lahar inundation  
1891 hazard zones. *Geol Soc Am Bull* 110, 8, 972-984.

1892 Iverson, R.M., George, D.L., Logan, M., 2016. Debris-flow run-up on vertical barriers and  
1893 adverse slopes. *J. Geoph. Res., Earth Surf.* 121, 2333-2357.

1894 Iverson, R.M., Logan, M., LaHusen, R.G., Berti, M., 2010. The perfect debris flow?  
1895 Aggregated results from 28 large-scale experiments. *J. Geophys. Res.* 115 (F3), 1-29.

1896 Iverson, R.M., Reid, M.E., Logan, M., LaHusen, R.G., Godt, J.W., Griswold, J.P., 2011.  
1897 Positive feedback and momentum growth during debris-flow entrainment of wet bed  
1898 sediment. *Nature Geosc.* 4, 2, 116-121.

1899 Jakob, M, Stein, D, Ulmi, M, 2012. Vulnerability of buildings to debris flow impact. *Nat Haz.*  
1900 60, 2, 241-261.

1901 Jenkins, S., Komorowski, J.-C., Baxter, P.J., Spence, R., Picquout, A., Lavigne, F., Surono,  
1902 2013. The Merapi 2010 eruption: An interdisciplinary impact assessment methodology for  
1903 studying pyroclastic density current dynamics. *J. Volcanol. Geoth. Res.* 261, 316-329.

1904 Jenkins, S.F., Spence, R.J.S., Fonseca, J.F.B.D, Solidum, R.U., Wilson, T.M., 2014. Volcanic  
1905 risk assessment: quantifying physical vulnerability in the built environment. *J. Volcanol.*  
1906 *Geoth. Res.* 276, 105-120.

1907 Jenkins, S.F., Phillips, J.C., Price, R., Feloy, K., Baxter P.J., Sri Hadmoko, D., de Bélizal, E.,  
1908 2015. Developing building-damage scales for lahars: application to Merapi volcano,  
1909 Indonesia. *Bull. Volcanol.* 77, 75, 1-17.

1910 Johnson, A.M., 1970. *Physical process in geology*. Freeman and Cooper, San Francisco, 577  
1911 pp.

1912 Johnston, D.M., Houghton, B.F., Neall V.E., Ronan K.R., Paton D., 2000. Impacts of the  
1913 1945 and 1995-1996 Ruapehu eruptions, New Zealand: an example of increasing societal  
1914 vulnerability. *Geol. Soc. Amer. Bull.* 112, 5, 720-726.

1915 Jones, R., Thomas, R.E., Peakall, J., Manville, V., 2017. Rainfall-runoff properties of tephra:  
1916 Simulated effects of grain-size and antecedent rainfall. *Geomorph.* 282, 39-51.

1917 Kang, H.-S., Kim Y.-T., 2016. The physical vulnerability of different types of building  
1918 structure to debris flow events. *Nat. Haz.* 80, 3, 1475-1493.

1919 Kaku, K., Aso, N., Takiguchi, F., 2015. Space-based response to the 2011 Great East Japan  
1920 Earthquake: Lessons learnt from JAXA's support using earth observation satellites. *Int. J. Dis.*  
1921 *Risk Red.* 12, 134-153.

1922 Kattel, P., Kafle, J., Fischer, J.T., Mergilie, M., Tuladhara, B.M., Pudasaini, S.P., 2018.  
1923 Interaction of two-phase debris flow with obstacles. *Eng. Geol.* 242, 197-217.

1924 Keigler, R., Thouret, J.-C., Hodgson, K., Neall, V., Lecointre, J., Procter, J.N., Cronin, S.J.,  
1925 2011. The Whangaehu Formation: Debris-avalanche and lahar deposits from ancestral  
1926 Ruapehu volcano, New Zealand. *Geomorphology* 133, 1, 57-79.

1927 Kelfoun, K., Druitt, T.H., 2005. Numerical modeling of the emplacement of Socompa rock  
1928 avalanche, Chile. *J. Geophys. Res.* 110, B12202.1-12202.13.

1929 Kerle, N., 2002. Volume estimation of the 1998 flank collapse at Casita volcano, Nicaragua: a  
1930 comparison of photogrammetric and conventional techniques. *Earth Surf. Proc. Landf.* 27, 7,  
1931 759-772.

1932 Kerle, N., Oppenheimer, C., 2002. Satellite remote sensing as a tool in lahar disaster  
1933 management. *Disasters* 26, 2, 140-160.

1934 Kerle, N., Hoffman, R.R., 2013. Collaborative damage mapping for emergency response: The  
1935 role of Cognitive Systems Engineering. *Nat. Hazards Earth Syst. Sci.* 13, 97-113.

1936 Kerle, N., Froger, J.L., Oppenheimer, C., Van Wyk de Vries, B., 2003. Remote sensing of the  
1937 1998 mudflow at Casita volcano, Nicaragua. *Int. J. Remote Sens.* 1-26.

1938 Kilgour, G., Manville, V., Della Pasqua, F., Graettinger, A., Hodgson, K.A., Jolly, G.E.,  
1939 2010. The 25 September 2007 eruption of Mount Ruapehu, New Zealand: Directed ballistics,  
1940 surtseyan jets, and ice-slurry lahars. *J. Volcanol. Geoth. Res.* 191, 1, 1-14.

1941 Künzler, M., Huggel, C., Ramirez, J.M., 2012. A risk analysis for floods and lahars: case  
1942 study in the Cordillera Central of Colombia. *Nat Hazards* 64, 767-796.

1943 Kwan, J.S.H., Sze, E.H.Y., Lam, C., 2018. Finite element analysis for rockfall and debris flow  
1944 mitigation works. *Advances in landslide understanding, Canadian Geotech. J.*, doi.org/  
1945 10.1139/cgj-2017-0628.

1946 Lai, V. H., Tsai, V.C., Lamb, M.P., Ulizio, T.P., Beer, A.R., 2018. The seismic signature of  
1947 debris flows: Flow mechanics and early warning at Montecito, California. *Geophys. Res. Lett.*  
1948 45, 5528-5535, doi:10.1029/2018GL0077

1949 Larcher, M., Fraccarollo, L., Armanini, A., Capart, H., 2007. Set of measurement data from  
1950 flume experiments on steady uniform debris flows. *J. Hydraul. Res.* 45, 59-71.

1951 Larsen, M.C., Wieczorek, G.F., 2006. Geomorphic effects of large debris flows and flash  
1952 floods, northern Venezuela (1999). *Z. Geomorph. N.F. Suppl.*-Vol. 145, 147-175.

1953 Lavigne, F., Thouret, J.-C., 2000. Les lahars: dépôts, origines et dynamique. *Bull. Soc. Géol.*  
1954 *Fra.* 1741, 5, 545-557.

1955 Lavigne, F., Thouret, J.-C., 2003. Sediment transportation and deposition by rain-triggered  
1956 lahars at Merapi volcano, central Java, Indonesia. *Geomorph* 49, 1-2, 45-69.

1957 Lavigne, F., Suwa, H. 2004. Contrasts between debris flows, hyperconcentrated flows and  
1958 stream flows at a channel of Mount Semeru, East Java, Indonesia. *Geomorph.* 61, 1-2, 41-58.

1959 Lavigne, F., Thouret, J.-C., Suwa, H., 2000a. Lahars at Merapi volcano, Central Java,  
1960 Indonesia: an overview. *J. Volcanol. Geoth. Res., Merapi Volcano spec.* vol. 100, 423-456.

1961 Lavigne, F., Thouret, J.-C., Suwa, Voight, B., Young, K., Lahusen, R., Sumaryano, A.,  
1962 Dejean, M., Sayudi, M., 2000b. Instrumental lahar monitoring at Merapi volcano, Central  
1963 Java, Indonesia. *J. Volcanol. Geoth. Res., Merapi Volcano spec.* vol. 100, 457-478.

1964 Léone, F., Gaillard, J.-C., 1999. Analysis of the institutional and social responses to the  
1965 eruption and the lahars of Mount Pinatubo volcano from 1991 to 1998 (Central Luzon,  
1966 Philippines). *GeoJournal* 49, 223-238.

1967 Li, H.C., Liu, K.F., 2010. The study on the indirect damage estimation of debris flow: a case  
1968 study in Song-He village, Taichung county. *J. Chinese Inst. Eng. (JCIE)* 22, 2, 159-166.

1969 Li, H.C., Liu, K.F., Hsu, Y.C., 2013. Loss curve analysis of a debris flow: a case study on the  
1970 Daiano Tribe watershed. *Applied Mechanics and Materials (Trans Tech Publications)* 284-  
1971 287, 1499-1513.

1972 Li, J., Luo, D., 1981. The formation and characteristics of mudflow and flood in the mountain  
1973 area of the Dachao River and its prevention. *Zeit. für Geomorph.* 25, 470-484.

1974 Li, P., Li, T., Lu, Z., Li, J., 2017. Study on dynamic response of novel masonry structures  
1975 impacted by debris flow. *Sustainability* 9, 7, 1122.

1976 Li, W., Wen J., Li X., 2018. Progress of research on economic loss assessment of disasters in  
1977 industrial networks. *Progress in Geography* 37, 3, 330-341.

1978 Liu, K.F., Li, H.C., 2007. Direct damage assessment for debris flows, pp. 423-432, *in*: Chen,  
1979 C.L. and Major, J.J., (eds.), *Debris Flow Hazard Mitigation: Mechanics, Prediction and*  
1980 *Assessment.* Millpress.

1981 Liu, K-F., Li, H-C., Hsu, Y-C., 2009. Debris flow hazard assessment with numerical  
1982 simulation. *Nat. Haz.*, 49, 137-161.

1983 Lube, G., Cronin, S.J., Procter, J.N., 2009. Explaining the extreme mobility of volcanic ice-  
1984 slurry flows, Ruapehu volcano, New Zealand. *Geology* 37, 1, 15-18.

1985 Lube, G., Cronin, J.S., Thouret, J.-C., Surono, 2011. Kinematic characteristics of pyroclastic  
1986 density currents at Merapi and controls on their avulsion from natural and engineered  
1987 channels. *Geol. Soc. Amer. Bull.* 123, 1127-1140.

1988 Lube, G., Cronin, S.J., Manville, V., Procter, J.N., Cole, S.E., Freundt, A., 2012. Energy  
1989 growth in laharcic mass flows. *Geology* 40, 5, 475-478.

1990 McCoy, S.W., Kean, J.W., Coe, J.A., Staley, D.M., Wasklewicz, T.A., Tucker, G.E., 2010.  
1991 Evolution of a natural debris flow: In situ measurements of flow dynamics, video imagery,  
1992 and terrestrial laser scanning. *Geology* 38, 8, 735-738.

1993 McDonald, G. W., Cronin, S.J., Kim, J-H., Smith, N.J., Murray, C.A., Procter, J.N., 2017.  
1994 Computable general equilibrium modelling of economic impacts from volcanic event  
1995 scenarios at regional and national scale, Mt. Taranaki, New Zealand. *Bull. Volc.* 79, 87.

1996 Magill, C., Blong, R., McAneney, J., 2006. VolcaNZ – A volcanic loss model for Auckland,  
1997 New Zealand. *J. Volcanol. Geoth. Res.* 149, 329-345.

1998 Mainsant, G., 2014. Etude géophysique des lahars. Rapport post-doc AXA (Unpubl., in  
1999 French with English summary), Laboratoire Magmas et Volcans, Université Clermont-  
2000 Auvergne, 89 pp.

2001 Major, J.J., 1997. Depositional processes in large-scale debris-flow experiments. *J. Geology*  
2002 105, 345-366.

2003 Major, J. J., 2000. Gravity-driven consolidation of granular slurries—Implications for debris-  
2004 flow deposition and deposit characteristics. *J. Sediment. Res.* 70, 1, 64-83.

2005 Major, J.J., Pierson, T.C., 1992. Debris flow rheology: experimental analysis of fine-grained  
2006 slurries. *Wat. Res. Res.* 28, 3, 841-857.

2007 Major, J.J., Iverson, R.M., 1999. Debris-flow deposition: effects of pore-fluid pressure and  
2008 friction concentrated at flow margins. *Geol. Soc. Amer. Bull.* 111, 1424-1434.

2009 Major, J.J., Janda, R.J., Daag, A.S., 1996. Watershed disturbance and lahars on the East side  
2010 of Mount Pinatubo during the mid-June 1991 eruptions, pp. 885-920, *in*: Newhall and  
2011 Punongbayan (Eds.), *Fire and Mud. Eruptions and lahars of Mount Pinatubo*, Philippines,  
2012 Phivolcs and University of Washington.

2013 Major, J.J., Bertin, D., Pierson, T.C., Amigo, A., Iroumé, A., Ulloa, H., Castro, J., 2016.  
2014 Extraordinary sediment delivery and rapid geomorphic response following the 2008-2009  
2015 eruption of Chaitén volcano, Chile. *Wat. Res. Res.* 52, 7, 5075-5094.

2016 Manville, V. 2004. Palaeohydraulic analysis of the 1953 Tangiwai lahar: the New Zealand  
2017 worst volcanic disaster. *Acta Vulcanol.* 16, 137-152.

2018 Manville, V., Cronin, S.J., 2007. Break-out lahar from New Zealand's Crater Lake. *EOS*,

2019 Transactions, AGU 88, 43, 441-442.

2020 Manville, V., Hodgson, K.A., White, J.D.L., 1998. Rheological properties of a remobilized  
2021 tephra lahar associated with the 1995 eruptions of Ruapehu volcano, New Zealand. New  
2022 Zealand J. Geol. Geophys. 41, 157-164.

2023 Manville, V., Nemeth, K., Kano, K., 2009. Source to sink: a review of three decades of  
2024 progress in the understanding of processes, deposits and hazards. Sedim. Geol. 220, 136-161.

2025 Manville, V. Major, J.J., Fagents, S.A., 2013. Modeling lahar behavior and hazards. Chap. 4,  
2026 pp. 300-330, in: Fagents, S.A., Gregg, T.K.P., Lopes, R.M.C. (Eds.), Modeling Volcanic  
2027 Processes. Cambridge University Press.

2028 Marcial, S., Melosantos, A. A., Hadley, K. C., LaHusen, R. G., Marso, J. N., 1996.  
2029 Instrumental lahar monitoring at Mount Pinatubo, pp. 1015-1022, *in*: Punongbayan and  
2030 Newhall (eds.), Fire and Mud: Eruptions and Lahars of Mount Pinatubo, Philippines,  
2031 University of Seattle and Phivolcs, Quezon City.

2032 Marchi, L., Arattano, M., Deganutti, A.M., 2002. Ten years of debris-flow monitoring in the  
2033 Moscardo Torrent (Italian Alps). Geomorphology 46, 1-17.

2034 Martelli, K., 2011. The physical vulnerability of urban areas facing the threat of inundation  
2035 from lahars and ash floods: application to the case study of Arequipa, Peru. Unpubl. PhD  
2036 thesis, Dept. Earth Sciences, Université Blaise Pascal, Clermont-Ferrand II, 341 pp.

2037 Martinez, C., Miralles-Wilhelm, F., Garcia-Martinez, R., 2011. Quasi-three dimensional  
2038 two-phase debris flow model accounting for boulder transport. Ital. J. Eng. Geol. Environ.  
2039 3, 457-466.

2040 Mavrouli, O., Corominas, J., 2010. Rockfall vulnerability assessment for reinforced concrete  
2041 buildings. Nat. Haz. Earth Syst. Sci. 10, 2055-2066.

2042 Mead, S., Magill, C., 2017. Probabilistic hazard modelling of rain-triggered lahars. J. Appl.  
2043 Volcanol. 6, 8.

2044 Mead, S., Magill, C., Hilton, J., 2016. Rain-triggered lahar susceptibility using a shallow  
2045 landslide and surface erosion model. Geomorphology 273, 168-177.

2046 Mead, S.R.M., Prakash, M., Magill, C., Bolger, M., Thouret, J.-C., 2015. A Distributed  
2047 Computing Workflow for Modelling Environmental Flows in Complex Terrain.  
2048 Environmental Software Systems. Infrastructures, Services and Applications. IFIP Advances  
2049 in Information and Communication Technology, Springer 448, pp. 321-332.

2050 Mead, S.R.M., Magill, C., Lemiale, V., Thouret, J.-C., Prakash, M., 2017. Quantifying lahar  
2051 damage using numerical modelling. Nat. Hazards Earth Sci. Sys. 17, 703-719.

2052 Mercado, R.A., Lacsamana, J.B.T., Pineda, G.L., 1996. Socio-economic impacts of the Mt.  
2053 Pinatubo eruptions, pp. 1063-1070, *in*: Fire and Mud. Eruptions and lahars of Mount  
2054 Pinatubo, Philippines. PHIVOLCS, Quezon City and University of Washington, Seattle.

2055 Meunier M., 1988. La lave torrentielle du Saint-Antoine à Modane, le 24 août 1987. O.N.F.–  
2056 CEMAGREF référence 3121, 14 p., annexes.

2057 Miyazaki, H., Nagai, M., Shibasaki, R., 2015. Reviews of Geospatial Information Technology  
2058 and Collaborative Data Delivery for Disaster Risk Management. ISPRS Int. J. Geo-Inf. 4,  
2059 1936-1964.

2060 Mothes, P.A., Hall, M.L., Janda, R.J., 1998. The enormous Chillos Valley lahar: an ash-flow-  
2061 generated debris flow from Cotopaxi Volcano, Ecuador. Bull. Volc. 59, 233-244.

2062 Mulder, T., Alexander, J. 2001. The physical character of subaqueous sedimentary density  
2063 flows and their deposits. Sedimentology 48, 269-299.

2064 Muñoz-Salinas, E., Renschler, C., Palacios, D, 2009a. A GIS-based model to determine the  
2065 volume of lahars: Popocatépetl volcano, Mexico. Geomorphology 111, 61-69.

2066 Muñoz-Salinas, E., Castillo-Rodríguez, M., Manea, V., Manea, M., Palacios, D, 2009b. Lahar  
2067 flow simulations using LAHARZ program: application for the Popocatépetl volcano, Mexico.  
2068 J. Volc. Geoth. Res. 182, 13-22.

2069 Muñoz-Salinas, E., Castillo-Rodríguez, M., Manea, V., Manea, M., Palacios, D, 2010. On the  
2070 geochronological method versus automated based models to obtain a lahar risk map of  
2071 Santiago Xalitzintla Town, Mexico. Geogr. Ann. Series A, 92, 311-328.

2072 Neall, V.E., 1976. Lahars. Global occurrence and annotated bibliography. Victoria University,  
2073 Wellington, NZ, Geol. Dept. Publ. 5, 1-18.

2074 Newhall, C.G., Solidum, R.U., 2015. Eruptions and lahars of Mount Pinatubo, 1991 to 2000,  
2075 pp. 249-253, *in*: Loughlin, S.C., Sparks, R.S.J., Brown, S.K., Jenkins, S.F., Vye-Brown, C.  
2076 (eds.), Global Volcanic Hazards and Risk, Cambridge University Press.

2077 Ng, C.W.W., Choi, C.E., Su, A.Y., Kwan, J.S.H., Lam, C., 2016. Large-scale successive  
2078 boulder impacts on a rigid barrier shielded by gabions. Can. Geotech. J. cgj-2016-0073.R2, 46  
2079 p.

2080 Nigro, E., Faella, C., 2008. Effects of debris flow on buildings, pp. 420-429, *in*: Mazzolani,  
2081 F.M. et al. (eds.), Urban Habitat under Catastrophic Events. Proceedings COST Action 26,  
2082 Final Conference, CRC Press.

2083 O'Brien, J.S., Julien, P.Y., Fullerton, W.T., Members ASCE, 1993. Two-dimensional water  
2084 flood and mudflow simulation. J. Hydraul. Eng. 119, 2, 244-261.

2085 O'Brien, J.S., Julien, P.Y., 2000. Flo-2D User's Manual, Version 2000.01; Flo-Engineering:  
2086 Nutrioso, AZ, USA, 170 pp.

2087 Okano, K., Suwa, H., Kanno, T., 2012. Characterization of debris flows by rainstorm  
2088 condition at a torrent on the Mount Yakedake volcano, Japan. *Geomorphology* 136, 1, 88-94.

2089 Oramas Dorta, D., Toyos, G., Oppenheimer C., Pareschi, M.T., R. Sulpizio, R., Zanchetta, G.,  
2090 2007. Empirical modelling of the May 1998 small debris flows in Sarno (Italy) using  
2091 LAHARZ. *Nat. Haz.* 40, 381-396.

2092 Paguican, E.M.R, Lagmay, A.M.F, Rodolfo, K.S., Rodolfo, R.S., Tengonciang, A.M.P.,  
2093 Lapus, M.R., Baliatan, E.G., Obille, Jr. E.C., 2009. Extreme rainfall induced lahars and dike  
2094 breaching, 30 November 2006, Mayon volcano, Philippines. *Bull. Volcanol.* 71, 845-857.

2095 Papathoma-Köhle, M., Gems, B., Sturm, M., Fuchs, S., 2017. Matrices, curves and indicators:  
2096 A review of approaches to assess physical vulnerability to debris flows. *Earth-Sci. Rev.* 171,  
2097 272-288.

2098 Pasculli, A., Minatti, L., Audisio, C., Sciarra, N., 2013. Insights on the application of some  
2099 current SPH approaches for the study of muddy debris flow: numerical and experimental  
2100 comparison. *WIT Trans. on Eng. Sci.*, 82, Advances in fluid mechanics, 14 p.

2101 Pastor, M., Haddad, B. Sorbino, G., Cuomo, S., Drempetic, V., 2009. A depth-integrated,  
2102 coupled SPH model for flow-like landslides and related phenomena. *Internat. J. Numer.*  
2103 *Analyt. Meth. Geomech.* 33, 2, 143-172.

2104 Patra, A.K., Bauer, A.C., Nichita, C.C., Pitman, E.B., Sheridan, M.F., Bursik, M., Rupp, B.,  
2105 Webber, A., Stinton, A.J., Namikawa, L.M., Renschler, C.S., 2005. Parallel adaptive  
2106 numerical simulation of dry avalanches over natural terrain. *J. Volc. Geoth. Res.* 139, 1-2, 89-  
2107 102.

2108 Petrucci, O., 2012. The impact of natural disasters: simplified procedures and open problems,  
2109 Chap. 6, pp. 109-132, *in*: Tiefenbacher, J. (Ed.), *Approaches to Managing Disaster, Assessing*  
2110 *Hazards, Emergencies and Disaster Impacts*, Intechopen, Doi: 10.5772/29147.

2111 Pierson, T.C., 1980. Debris flows: An important process in high country gully erosion. *J. of*  
2112 *the Tussok Grassland and Mountain Lands Institute (N.Z.)* 39, 3-14.

2113 Pierson, T.C., 1986. Flow behavior of channelized debris flows, Mount St. Helens,  
2114 Washington, pp. 269-296, *in*: Abrahams, A.D. (Ed.), *Hillslope Processes*, Allen and Unwin.

2115 Pierson, T.C., 1995. Flow characteristics of large eruption-triggered debris flows at snow-clad  
2116 volcanoes: constraints for debris-flow models. *J. Volcanol. Geoth. Res.* 66, 1-4, 283-294.

2117 Pierson, T.C., 2005. Hyperconcentrated flow – transitional process between water flow and  
2118 debris flow. Chapt. 8, pp. 159-208, in: Jakob, M., Hungr, O. (Eds.). Debris-flow hazards and  
2119 related phenomena, Springer.

2120 Pierson, T.C., Scott K.M., 1985. Downstream dilution of a lahar: Transition from debris flow  
2121 to hyperconcentrated streamflow. *Water Res. Res.* 21, 10, 1511-1524.

2122 Pierson, T.C., Costa, J.E., 1987. A rheologic classification of subaerial sediment-water flows.  
2123 *Rev. Eng. Geol.* VII, 1-12.

2124 Pierson, T.C., Janda, R.J., 1992. Immediate and long-term hazards from lahars and excess  
2125 sedimentation in rivers draining Mt. Pinatubo, Philippines. *Water-Res. Investig. Report* 92-9.

2126 Pierson, T.C., Major, J.J., 2014. Hydrogeomorphic effects of explosive volcanic eruptions on  
2127 drainage basins. *Annu. Rev. Earth Planet. Sci.* 42, 469-507.

2128 Pierson, T.C., Wood, N., Driedger, C.L., 2014. Reducing risk from lahar hazards: concepts,  
2129 case studies, and roles for scientists. *J. Appl. Volcanol.* 3, 16, 1-25.

2130 Pierson, T.C., Janda, R.J., Thouret, J.-C., Borrero, C.A., 1990. Perturbation and melting of  
2131 snow and ice by the 13 November 1985 eruption of Nevado del Ruiz, Colombia, and  
2132 consequent mobilization, flow and deposition of lahars. *J. Volc. Geoth. Res.* 41, 17-66.

2133 Pierson, T. C., Major, J. J., Amigo, A., Moreno, H., 2013. Acute sedimentation response to  
2134 rainfall following the explosive phase of the 2008-2009 eruption of Chaitén volcano, Chile.  
2135 *Bull. Volcanol.* 75, 1-17, doi: 10.1007/s00445-013-0723-4

2136 Pierson, T.C., Daag, A.S., Delos Reyes, P.J., Regalado, M.T.A., Solidum, R.U., Tubianosa,  
2137 B.S. 1996. Flow and deposition of posteruption hot lahar on the east side of Mount Pinatubo,  
2138 July-October 1991, pp. 921-950, *in*: Newhall C.G. and Punugbayan R.S. (Eds), *Fire and Mud:  
2139 Eruptions and Lahars of Mount Pinatubo, Philippines*. PHIVOLCS, Quezon City and  
2140 University of Washington Press, Seattle.

2141 Pitman, E.B., Le L., 2005. A two-fluid model for avalanche and debris flows. *Philos. Trans.*  
2142 *R. Soc. London, A Math Phys. Eng. Sci.* 363, 1832, 1573-1601.

2143 Prieto, J.A., Journeay, M., Acevedo, A.B., Arbelaez, J.D., Ulmi, M., 2018. Development of  
2144 structural debris flow fragility curves (debris flow buildings resistance) using momentum flux  
2145 rate as a hazard parameter. *Eng. Geol.* 239, 144-157.

2146 Procter, J., Cronin, S.J., Sheridan, M., 2012. Evaluation of Titan2D modelling forecasts for  
2147 the 2007 Crater Lake break-out lahar, Mt. Ruapehu, New Zealand. *Geomorphology* 136, 1,  
2148 95-105.

2149 Procter, J.N., Cronin, S.J., Fuller, I.C., Lube, G., Manville, V., 2010a. Quantifying the  
2150 geomorphic impacts of a lake-breakout lahar, Mount Ruapehu, New Zealand. *Geology* 38, 1,  
2151 67-70.

2152 Procter, J.N., Cronin, S.J., Fuller, I.C., Sheridan, M., Neall, V.E., Keys, H., 2010b. Lahar  
2153 hazard assessment using Titan2D for an alluvial fan with rapidly changing geomorphology:  
2154 Whangaehu River, Mt. Ruapehu. *Geomorphology* 116, 162-174.

2155 Proske, D., Suda, J., Hübl, J., 2011. Debris flow impact estimation for breakers. *GeoRisk,*  
2156 *Assessment and Management of Risk for Engineered Systems and Geohazards* 5, 2, 143-155.

2157 Punongbayan, R.S., Newhall, C.G., (Eds.), 1996. *Fire and Mud. Eruptions and lahars of*  
2158 *Mount Pinatubo, Philippines.* PHIVOLCS, Quezon City and University of Washington,  
2159 Seattle, 1126 pp.

2160 Quan Luna, B., Blahut, J., van Westen, C.J., Sterlacchini, S., van Asch, T.W.J., Akbas, S.O.,  
2161 2011. The application of numerical debris flow modelling for the generation of physical  
2162 vulnerability curves. *Nat. Haz. Earth Syst. Sci.* 11, 2047-2060.

2163 Rheinberger, C.M., Romang, H.E., M. Bründl, M., 2013. Proportional loss functions for  
2164 debris flow events. *Nat. Haz. Earth Syst. Sci.* 13, 2147-2156.

2165 Rickenmann, D., 1999. Empirical Relationships for Debris Flows. *Nat. Haz.* 19, 47-77.

2166 Rickenmann, D., 2005. Runout prediction methods, pp. 305-324, *in: Jakob, M, Hungr, O.*  
2167 *(eds.), Debris-Flow Hazards and Related Phenomena, Praxis Springer.*

2168 Rodolfo, K.S., 1995. *Pinatubo and the Politics of Lahar. Eruption and aftermath, 1991.*  
2169 *University of the Philippines Press, Quezon City, 341 pp.*

2170 Rodolfo, K.S., Arguden, A.T., 1991. Rain-lahar generation and sediment delivery systems at  
2171 Mayon Volcano, Philippines, pp. 71-87, *in: Fisher, RV, Smith, GA (eds), Sedimentation in*  
2172 *Volcanic Settings, SEPM, Special Publ. 45.*

2173 Rodriguez, F., Toulkeridis, T., Sandoval, W., Padilla, O., Mato, F., 2017. Economic risk  
2174 assessment of Cotopaxi volcano, Ecuador, in case of a future lahar emplacement. *Nat. Haz.*  
2175 *85, 605-618.*

2176 Rodríguez-Espinosa, D.M., Córdoba-Guerrero, G., Delgado-Granados, H., 2017. Evaluación  
2177 probabilística del peligro por lahares en el flanco NE del volcán Popocatepetl, *Bol. Soc. Geol.*  
2178 *Mexic.* 69, 1, 243-260.

2179 Santi, P.M., Hewitt, K., VanDine, D.F., Cruz, E.B., 2011. Debris flow impact, vulnerability  
2180 and response. *Nat. Haz.* 56, 1, 371-402.

2181 Scheidl, C., Rickenmann D., 2010. Empirical prediction of debris-flow mobility and  
2182 deposition on fans. *Earth Surf. Proc. Landf.* 35, 157-173.

2183 Scheidl, C., Rickenmann D., 2011. TopFlowDF--a simple GIS- based model to simulate  
2184 debris-flows runout on fans. *Ital. J. Eng. Geol. Envir.*, 5th Int. Conf. Debris-Flow Haz. Mitig.,  
2185 Mecha. Pred. Assess, Padua, Cada Edit. Univ. La Sapienza, 253-262.

2186 Schilling, S.P., 1998. LAHARZ; GIS programs for automated mapping of lahar-inundation  
2187 hazard zones. U.S. Geol. Surv. Open File Report 98-638, 80 pp.

2188 Schilling, S.P., 2014. Laharz\_py: GIS tools for automated mapping of lahar inundation  
2189 hazard zones. U.S. Open File Report 2014-1073, 78 pp.

2190 Scott, G.A.J., 2010. An overview of destruction and recovery in the Mt. Mayon volcano  
2191 region, Bicol, Philippines, resulting from lahars initiated by Supertyphon Reming. *Prairie*  
2192 *Perspectives, Geogr. Essays* 13, 67-77.

2193 Scott, K.M., 1988. Origins, behavior, and sedimentology of lahars and lahar-runout flows in  
2194 the Toutle-Cowlitz river system. U.S. Geol. Surv. Prof. Paper 1447-A, 74 pp.

2195 Scott, K.M, Vallance, J.W., Pringle, P.T., 1995. Sedimentology, behavior, and hazards of  
2196 debris flows at Mount Rainier, Washington. U.S. Geol. Surv. Prof. Paper 1547, 56 pp.

2197 Scott, K.M., Macias, J.L., Naranjo, J.A., Rodriguez, S., McGeehin, J.P., 2001. Catastrophic  
2198 debris flows transformed from landslides in volcanic terrains: mobility, hazard assessment,  
2199 and mitigation strategies. U.S. Geol. Survey Prof. Paper 1630, 59 pp.

2200 Scott, K.M., Vallance, J.W., Kerle, N., Macías, J.L., Strauch, W., Devoli, G., 2005.  
2201 Catastrophic precipitation-triggered lahar at Casita volcano, Nicaragua: occurrence, bulking  
2202 and transformation. *Earth Surf. Proc. Land.* 30, 1, 59-79.

2203 Sheridan, M., Stinton, A., Patra, A., Pitman, E., Bauer, A., Nichita, C., 2005. Evaluating  
2204 Titan2D mass-flow model using the 1963 Little Tahoma Peak avalanches, Mount Rainier,  
2205 Washington. *J. Volc. Geoth. Res.* 139, 1-2, 89-102.

2206 Solikhin, A., Thouret, J-C., Liew, S.C., Gupta, A., Sri Sayudi, D., Oehler, J-F., 2015. Deposits  
2207 and effects from the 2010 pyroclastic density currents and lahars at Merapi Volcano: Mapped  
2208 and analyzed from high-spatial resolution imagery. *Bull. Volc.* 77, 20.

2209 Sosio, R., Crosta, G.B., 2009. Rheology of concentrated granular suspensions and possible  
2210 implications for debris flow modeling. *Water Res. Res.* 45, W03412.

2211 Sosio, R., Crosta, G.B., 2011. Data uncertainty and variability in modeling debris flow  
2212 propagation. *Ital. J. Engin. Geol. Envir.* 3(B), 219-228.

2213 Sosio, R., Crosta, G.B., Frattini, P., 2007. Field observations, rheological testing and  
2214 numerical modelling of a debris-flow event. *Earth Surf. Proc. Landf.* 32, 2, 290-306.

2215 Starheim C.A., Gomez, C., Davies, T., Lavigne, F., Wassmer, P., 2013. In-flow evolution of  
2216 lahar deposits from video-imagery with implications for post-event deposit interpretation,  
2217 Mount Semeru, Indonesia. *J. Volcanol. Geoth. Res.* 256, 96-104.

2218 Suroño, P., Jousset, J., Pallister, M., Boichu, M.F., Buongiorno, A., Budisantoso, F., Costa, S.,  
2219 Andreastuti, F., Prata, D., Schneider, L., Clarisse, H., Humaida, S., Sumarti, C., Bignami, J.,  
2220 Griswold, S., Carn, C., Oppenheimer, C., Lavigne F., 2012. The 2010 explosive eruption of  
2221 Java's Merapi volcano—a "100-year" event. *J. Volc. Geoth. Res.* 241-242, 121-135.

2222 Suwa, H., Yamakoshi, T., Sato, K., 2000. Relationship between debris-flow discharge and  
2223 ground vibration, pp. 16-18, *in: Proc. 2nd Internat. Conf. Debris-flow Hazards Mitigation:*  
2224 *Mechanics, Prediction, and Assessment*, Taipei.

2225 Swiss Re, 1998. *Floods -- an insurable risk?* Zurich, 48 pp.

2226 Talon, A., Bacconnet, C., Fabre D., Cespedes, X., Thouret, J.-C., 2012. Evaluation de la  
2227 vulnérabilité des constructions de la ville d'Arequipa (Pérou) face aux impacts de lahar.  
2228 XXXe Rencontres AUGC-IBPSA, 1-10.

2229 Takahashi, T., 2014. *Debris Flow, Mechanics, Prediction and Countermeasures*. CRC Press  
2230 Taylor and Francis Group, 2nd edition, Balkema, 448 pp.

2231 Tarbotton, C., Dall'osso, F., Dominey-Howes, D., Goff, J., 2015. The use of empirical  
2232 vulnerability functions to assess the response of buildings to tsunami impact: comparative  
2233 review and summary of best practice. *Earth Sci. Rev.* 142, 120-134.

2234 Thouret, J.-C., Lavigne, F., Suwa, H., Sukatja, B., Suroño, 2007. Volcanic hazards at Mount  
2235 Semeru, East Java (Indonesia), with emphasis on lahars. *Bull. Volcanol.* 70, 221-244.

2236 Thouret J.-C., Gupta A., Lube G., Liew S.C., Cronin S.J., Suroño, 2010. Analysis of the 2006  
2237 eruption deposits of Merapi Volcano, Java, Indonesia, using high-resolution IKONOS images  
2238 and complementary ground based observations. *Remote Sens. Environ.* 114, 1949-1967.

2239 Thouret, J.-C., Enjolras, G., Martelli, K., Santoni, O., Luque, J.A., Nagata, M., Arguedas, A.,  
2240 Macedo, L., 2013. Combining criteria for delineating lahar- and flash flood-prone hazard and  
2241 risk zones in the city of Arequipa, Peru. *Nat. Hazards Earth Syst. Sci.* 13, 339-360.

2242 Thouret, J.-C., Oehler, J.-F., Gupta, A., Solikhin, A., Procter, J.N., 2014a. Erosion and  
2243 aggradation on persistently active volcanoes—a case study from Semeru Volcano, Indonesia.  
2244 *Bull. Volcanol.* 76, 857.

2245 Thouret, J.-C., Ettinger, S., Guitton, M., Santoni, O., Magill, C., Martelli, K., Zuccaro, G.,  
2246 Revilla, V., Charca, J.A., Arguedas, A., 2014b. Assessing physical vulnerability in large cities  
2247 exposed to flash floods and debris flows: the case of Arequipa (Peru). *Nat. Haz.* 73, 3, 1771-  
2248 1815.

2249 Thouret, J.-C., Kassouk, Z., Gupta, A., Liew, SC., Solikhin, A., 2015. Tracing the evolution  
2250 of 2010 Merapi volcanic deposits (Indonesia) based on object-oriented classification and  
2251 analysis of multi-temporal, very high resolution images. *Rem. Sens. Envir.* 70, 350-371.

2252 Tiberghien, D., Laigle, D., Naaïm, N., Thibert, E., Ousset F., 2007. Experimental  
2253 investigations of interaction between mudflow and an obstacle, pp. 281-292, *in*: Chen, C.L.,  
2254 Major, J.J. (eds.), *Debris Flow Hazard Mitigation: Mechanics, Prediction and Assessment*.  
2255 Millpress Science Publishers.

2256 Tierz, P., Woodhouse, M.J., Phillips, J.C., Sandri, L., Selva, J., Marzocchi, W., Odbert, H.M.,  
2257 2017. A framework for probabilistic multi-hazard assessment of rain-triggered lahars using  
2258 Bayesian belief networks. *Front. Earth Sci.* 5, 73.

2259 Tonnellier, A., Helmstetter, A., Malet, J.P., Schmittbuhl, J., Corsini, A., Joswig, M., 2013.  
2260 Seismic monitoring of soft-rock landslides: the Super-Sauze and Valoria case studies,  
2261 *Geophys. J. Internat.* 193, 3, 1515-1536.

2262 Tost, M., Cronin, S.J., 2015. Linking distal volcanoclastic sedimentation and stratigraphy with  
2263 the development of Ruapehu volcano, New Zealand. *Bull. Volc.* 77, 95.

2264 Toyos, G., Oramas Dorta, D., Oppenheimer, C., Pareschi, MT, Sulpizio, R, Zanchetta, G., 2007.  
2265 GIS-assisted modelling for debris flow hazard assessment based on the events of May 1998 in  
2266 the area of Sarno, Southern Italy: I. Maximum run-out. *Earth Surf. Proc. Landf.* 32, 1491-  
2267 1502.

2268 Toyos G., Gunasekera R., Zanchetta G., Oppenheimer C. Sulpizio R., Favalli M, Pareschi  
2269 M.T., 2008. GIS-assisted modelling for debris-flow hazard assessment based on the events of  
2270 May 1998 in the area of Sarno, Southern Italy: II. Velocity and dynamic pressure. *Earth Surf.*  
2271 *Landf. Proc.* 33, 1693-1708.

2272 Turnbull, B., Bowman, E.T., McElwaine, J.N., 2015. Debris flows: Experiments and  
2273 modelling. *C.R. Physics* 16, 86-96.

2274 Vallance, J.W., 2000. Lahars, pp. 601-615, *in*: Sigurdsson, H. et al. (eds.), *Encyclopedia of*  
2275 *Volcanoes*, First edit., Academic Press, San Diego.

2276 Vallance, J.W., Iverson, R., 2015. Lahars and their deposits, pp. 649-664, *in*: Sigurdsson, H.  
2277 et al. (eds.), *Encyclopedia of Volcanoes*, 2nd edit., Academic Press, San Diego.

2278 Vallance, J.W., Scott, K.M., 1997. The Osceola Mudflow from Mount Rainier:  
2279 Sedimentology and hazard implications of a huge clay-rich debris flow. *Geol. Soc. Am. Bul.*  
2280 109, 143-163.

2281 Van Westen, C., Daag, A., 2005. Analysing the relation between rainfall characteristics and  
2282 lahar activity at Mount Pinatubo, Philippines. *Earth Surf. Process. Landf.* 30, 13, 1663-  
2283 1674.

2284 Vargas Franco, R., Thouret, J.-C., Delaite, G., van Westen, C., Sheridan, M.F., Siebe, C.,  
2285 Mariño, J., Souriot, T., Stinton, A., 2010. Mapping and Assessing Volcanic Hazards and  
2286 Risks in the city of Arequipa, Peru, based on GIS techniques, pp. 265-280, *in*: Groppelli, G.,  
2287 Viereck-Goette, L. (eds.), *Stratigraphy and Geology of volcanic areas*, Geol. Soc. Amer. Spec.  
2288 Paper 464.

2289 Vázquez, R., Capra, L., Caballero, L., Arámbula-Mendoza, R., Reyes-Dávila, G., 2014. The  
2290 anatomy of a lahar: Deciphering the 15th September 2012 lahar at Volcán de Colima, México.  
2291 *J. Volc. Geoth. Res.* 272, 126-136.

2292 Vázquez, R., Suriñach, E., Capra, L., Arámbula-Mendoza, R., Reyes-Dávila, G., 2016.  
2293 Seismic characterisation of lahars at Volcán de Colima, Mexico. *Bull. Volcanol.* 78, 8.

2294 Vetrivel, A., Gerke, M., Kerle, N., Vosselman, G., 2016. Identification of structurally  
2295 damaged areas in airborne oblique images using a visual-bag-of-words approach. *Rem. Sens.*  
2296 8, 231, 22.

2297 Vetrivel, A., Gerke, M., **Kerle, N.**, Nex, F.C., Vosselman, G., 2018. Disaster damage  
2298 detection through synergistic use of deep learning and 3D point cloud features derived from  
2299 very high resolution oblique aerial images, and multiple-kernel-learning. *ISPRS J. Photogram.*  
2300 *Rem. Sens.* 140, 45-59.

2301 Voigt, S., Schneiderhan, T., Twele, A., Gähler, M., Stein, E., Mehl, H., 2011. Rapid damage  
2302 assessment and situation mapping: Learning from the 2010 Haiti earthquake. *Photogram. Eng.*  
2303 *Rem. Sens.* 77, 9, 923-931.

2304 Waldron, H.H., 1967. Debris flow and erosion control problems caused by the ash eruptions  
2305 of Irazu volcano, Costa Rica. *U.S. Geol. Surv. Bull.* 1241, 1, 1-37.

2306 Wang, C., Esaki, T., Xie, M., Qiu, C., 2006. Landslide and debris-flow hazard analysis and  
2307 prediction using GIS in Minamata–Hougawachi area, Japan. *Envir. Geol.* 51, 1, 91-102.

2308 Wang, D., Chen, Z., He, S., Liu, Y., Tang, H., 2018. Measuring and estimating the impact  
2309 pressure of debris flows on bridge piers based on large-scale laboratory experiments.  
2310 *Landslides*, DOI 10.1007/s10346-018-0944-x

2311 Wendeler, C., Volkwein, A., Denk, M., Roth A., Wartmann, S., 2007. Field measurements  
2312 used for numerical modeling of flexible debris flow barriers, pp. 681-687, *in*: Chen, C.L.,  
2313 Major, J.J. (eds.), *Debris-Flow Hazard Mitigation: Mechanics, prediction and assessment*,  
2314 Millpress.

2315 Wibowo, S.B., Lavigne, F., Mourot, P., Metaxian, J.-P., Zeghdoudi, M., Virmoux, C.,  
2316 Sukatja, C.B., Hadmoko, D.S., Mutaqin, B.W., 2015. Analyse couplée d'images video et de  
2317 données sismiques pour l'étude de la dynamique d'écoulement des lahars sur le volcan  
2318 Merapi, Indonésie. *Geomorph., Relief, Proc. Environ.* 21, 3, 251-266.

2319 Wieczorek, G.F., Larsen, M.C., Eaton, L.S., Morgan, B.A., Blair, J. L., 2003. Debris-flow and  
2320 flooding hazards associated with the December 1999 storm in coastal Venezuela and  
2321 strategies for mitigation. U.S. Geol. Survey, Open File Report 01-014.

2322 Wignaux, M., Weir, J.J., 1990. A general model for Mt. Ruapehu lahars. *Bull. Volc.* 52, 381-  
2323 390.

2324 Williams, R., Stinton, A.J., Sheridan, M.F., 2008. Evaluation of the Titan2D two-phase flow  
2325 model using an actual event: case study of the 2005 Vazcún Valley Lahar. *J. Volc. Geoth.*  
2326 *Res.* 177, 4, 760-766.

2327 Wilson, T.M., Stewart, C., Sword-Daniels, V., Leonard, G.S., Johnston, D.M., Cole, J.,  
2328 Wardman, J., Wilson, G., Barnard, S.T., 2012. Volcanic ash impacts on critical infrastructure.  
2329 *Phys. Chem. Earth* 45-46, 5-23.

2330 Wilson, G., Wilson, T.M., Deligne, N.J., Cole, J.V., 2014. Volcanic hazard impacts to critical  
2331 infrastructure: A review. *J. Volc. Geoth. Res.* 286, 148-182.

2332 Wilson, G., Wilson, T.M., Deligne, N.I., Blake, D.M., Cole, J.W., 2017. Framework for  
2333 developing volcanic fragility and vulnerability functions for critical infrastructure. *J. Appl.*  
2334 *Volcanol.* 6, 14, 1-24.

2335 Wignaux, M., Weir, G.J., 1990. A general model for Mt. Ruapehu lahars. *Bull. Volc.* 52, 381-  
2336 390.

2337 Wörni, R., Huggel, C., Stoffel, M., Pulgarín, B., 2012. Challenges of modeling current very  
2338 large lahars at Nevado del Huila Volcano, Colombia. *Bull. Volc.* 74, 309-324.

2339 Xianbin, Y., Chen, X.Q., Chen, J., 2016. Finite element analysis of the concrete gravity debris  
2340 dam by impact effect of the massive stone in the debris flow. *Electronic J. Geotech. Eng.* 19,  
2341 2779-2790.

2342 Yésou, H., Chastanet, P., Maxant, J., Huber, C., Clandillon, S., Battison, S., Proy, C., de  
2343 Fraipont, P., 2015. Contribution de l'imagerie Pléiades à la cartographie rapide des dégâts  
2344 suite à des catastrophes majeures : retour d'expérience après deux ans d'action de  
2345 cartographie rapide localisée en Asie, en Afrique, en Europe et aux Caraïbes. *Rev. Franç.*  
2346 *Photogram. Télédét.* 209, 81-87.

2347 Yu, G., Zhang, M., Cong, K., Pei, L., 2015. Critical rainfall thresholds for debris flows in Sanyanyu,  
2348 Zhouqu County, Gansu Province, China. *Quart. J. Eng. Geol. Hydrogeol.* 48, 224-233.

- 2349 Yulianto, F., Sofan, P., Rokhis Khomarudin, M., Haidar, M., 2013. Extracting the damaging  
2350 effects of the 2010 eruption of Merapi volcano in Central Java, Indonesia. *Nat. Haz.* 66, 229-  
2351 247.
- 2352 Zanchetta, G., Sulpizio, R., Pareschi, M.T., Leoni, F.M., Santacroce, R., 2004. Characteristics  
2353 of May 5-6, 1998 volcanoclastic debris flows in the Sarno area (Campania, southern Italy):  
2354 relationships to structural damage and hazard zonation. *J. Volc. Geoth. Res.* 133, 377-393.
- 2355 Zanuttigh, B., Lamberti, A., 2006. Experimental analysis of the impact of dry avalanches on  
2356 structures and implication for debris flows. *Int. J. Hydraul. Res.* 44, 4, 522-534.
- 2357 Zeng, C., Cui, P., Su, Z., Lei, Y., Chen, R., 2015. Failure modes of reinforced concrete  
2358 columns of buildings under debris flow impact. *Landslides* 12, 561-571.
- 2359 Zhang, S., 1993. A comprehensive approach to the observation and prevention of debris flows  
2360 in China. *Nat. Haz.* 7, 1-23.
- 2361 Zhang, Y., Wei, F.Q., Wang Q., 2006. Impact force calculation of viscous debris flow based  
2362 on momentum conservation. *J. Sed. Res.* 3, 24-27.
- 2363 Zhang, Y., Wei, F.Q., Wang Q., 2007. Dynamic response of buildings struck by debris flows,  
2364 pp. 293-304, *in*: Chen, C.L., Major, J.J. (eds.), *Debris Flow Hazard Mitigation: Mechanics,*  
2365 *Prediction and Assessment.* MillPress.
- 2366 Zhang, S., Zhang, L., Li, X., Xu, Q., 2018. Physical vulnerability models for assessing  
2367 building damage by debris flows. *Eng. Geol.* 247, 145-158.
- 2368 Zhou, G. G., Ng, C.W., 2010. Dimensional analysis of natural debris flows. *Can. Geotech. J.*  
2369 47, 7, 719-729.
- 2370 Zobin, V. M., Plascencia, I., Reyes, G., C. Navarro, C., 2009. The characteristics of seismic  
2371 signals produced by lahars and pyroclastic flows: Volcán de Colima, México. *J. Volc. Geoth.*  
2372 *Res.* 179, 1, 157-167.
- 2373 Zuccaro, G., De Gregorio, D., 2013a. Time and space dependency in impact damage  
2374 evaluation of a sub-Plinian eruption at Mount Vesuvius. *Nat. Haz.* 68, 1399-423.
- 2375 Zuccaro, G., Leone, M. F., Del Cogliano, D., Sgroi, A., 2013b. Economic impact of explosive  
2376 volcanic eruptions: A simulation-based assessment model applied to Campania region  
2377 volcanoes. *J. Volc. Geoth. Res.* 266, 1-15.
- 2378 Zuccaro, G., De Gregorio, D., Baxter, P.J., 2015. Human and structural vulnerability to  
2379 volcanic processes, pp. 261-288, *in*: Papale, P. (ed.), *Volcanic hazards, risks, and disasters,*  
2380 *Hazards and disasters series,* Elsevier.

2381

2382 **Table captions**

2383 **Table 1.** A selection of lahar and debris-flow events showing hydraulic, physical, and  
2384 rheological characteristics and related impacts. Symbol meaning: LH Lahars with HCF  
2385 hyperconcentrated flow subtype –DF, when not indicated–, and occurrence: p primary (syn-  
2386 eruptive) lahar, pe post-eruptive lahar, s secondary rain-triggered lahar. Grey rows are non-  
2387 volcanic DFs; \*reconstructed value. References No.: 1 Vallance (2000); 2 Neall (1976); 3  
2388 Barberi et al. (1992); 4 Arguden and Rodolfo (1990); 5 Wignaux and Weir (1990), Manville  
2389 (2004); 6 Cronin et al. (1999, 2000); Johnston et al. (2000), Graettinger et al. (2010); 7 Manville  
2390 et al. (2007), Procter et al. (2010a,b), Kilgour et al. (2010); 8 Waldron (1967); 9 Fink et al.  
2391 (1981), Pierson and Scott (1985); 10 Pierson et al. (1990), Pierson (1995); 11 Major et al.  
2392 (1996), Mercado et al. (1996), Pierson et al. (1996), Leone and Gaillard (1999), Pierson (2005);  
2393 12 Pierson et al. (2014); 13 Kerle et al. (2003), Scott et al. (2005); 14 Zanchetta et al., (2004),  
2394 Toyos et al. (2007, 2008); 15 Paguican et al. (2009), Scott (2010); 16 Lavigne and Suwa (2004),  
2395 Thouret et al. (2007); 17 Dumaisnil et al. (2010), Doyle et al. (2010, 2011); 18 Pierson et al.  
2396 (2013), Major et al. (2016); 19 De Belizal (2013), De Belizal et al. (2013), Yulianto et al.  
2397 (2013), Solikhin et al. (2015); 20 Rickenmann (1999); Hübl et al. (2009, including ref. from  
2398 Costa 1984), Proske et al. (2011); 21 Cooley et al. (1977); 22 Li and Luo (1981); 23 Pierson  
2399 (1980); 24 Ballandras (1993); 25 Bellet (1988), Meunier (1988); 26 Rickenmann (1999), Santi  
2400 et al. (2011); 27 Wieczorek et al. (2003), Larsen and Wieczorek (2006); 28 Sosio and Crosta  
2401 (2011); 29 Kang and Kim (2006), *in* Hong et al. (2015); 30 Cesca and D’Agostino (2008); 31  
2402 Fan et al. (2018).

2403

2404 **Table 2.** Actions, processes, and effects of LH and DF for people and living organisms.

2405

2406 **Table 3.** Geomorphic impacts and changes due to LHs and DFs and excess sedimentation (see  
2407 Pierson and Major, 2014 for a review of explosive eruption impacts on drainage basins, and  
2408 Manville et al., 2009 for a review of volcanoclastic processes, deposits and hazards).

2409

2410 **Table 4.** Numerical codes and programs used for LHs/DFs modelling, parameters used and  
2411 outputs, usefulness, applications and limitations.

2412

2413 **Table 5.** Mechanisms of impacts exerted by LH/DFs on buildings, infrastructure, and other  
2414 valuables. \*Young Modulus (elasticity, in MPa) for: brick: 1400; woodpaper: 3000–4000;  
2415 plywood: 5500; wood from 9,500 to 16,000, and bamboo: 20,000; RC reinforced concrete E20:  
2416 20,000; Aluminium steel: 72,000; Carbon alloy steel: 210,000.

2417

2418 **Table 6. A.** Impact metrics (IMs) used to assess impact (damage) to critical infrastructure and  
2419 other valuables (broken into components and properties) impacted by LHs/DFs based on a  
2420 review of case studies. *Impact metrics IMs* (Wilson et al., 2017). Damage percentage or  
2421 index: percentage of damage sustained by an asset compared to pre-impact condition. Damage  
2422 ratio: the cost of repair relative to the cost of replacement. Function loss index: loss of  
2423 function compared to pre-impact condition normalised between 0 and 1 or expressed as a  
2424 percentage. Economic cost: absolute cost of impact(s) in monetary value. LH/DF hazard  
2425 metrics include: flow depth, velocity, momentum flux rate ( $h v^2$ ), dynamic and hydrostatic  
2426 pressure, collision of boulders. **B.** Four categories of event scenarios in terms of magnitude,  
2427 flow characteristics, and consequences.

2428

### 2429 **Figure captions**

2430

2431 **Figure 1.** Distribution of volcano fatalities according to hazard (a) for all fatal incidents and (b)  
2432 with the largest five disasters removed, where primary and secondary lahars (combined) ranked  
2433 as the second most lethal phenomenon after pyroclastic density currents (Auker et al., 2013,  
2434 reproduced with permission from Springer Nature via an Open Access Journal; See also Brown  
2435 et al., 2017).

2436

2437 **Figure 2.** Sketch of a lahar flow including head, body and tail, each having specific hydraulic  
2438 and sedimentary characteristics (Pierson, 1986, reproduced with permission from  
2439 HarperCollins Publishers UK, 2019).

2440

2441 **Figure 3.** Schematic hydrographs showing how lahars, beginning as water floods, typically  
2442 start and behave as they move downstream. (A) Flood flow; (B) Debris flow; (C) Transitional  
2443 flow; (D) Hyperconcentrated flow. The diagram also illustrates the progressive-aggradation  
2444 model of inverse grading in panels (C) and (D) (Vallance and Iverson, 2015, reproduced with  
2445 permission from Elsevier, 24 March 2019).

2446

2447 **Figure 4.** Simplified diagram of flow regimes (After Ancey, 2007, modified, reproduced with  
2448 permission from Elsevier via Copyright Clearance Center, 7 March 2019). The transitions  
2449 between regimes are described using dimensionless numbers. The Peclet  $Pe = 6\pi\mu a^3 \dot{\gamma} / (kT)$   
2450 (with  $T$  temperature and  $k$  Boltzmann constant) for the transition between Brownian (thermal

2451 agitation of particles) and viscous regimes; the repulsion number  $Nr = \Psi / (kT)$  (with  $\Psi$  van der  
 2452 Waals interaction potential) for the transition between the colloidal and Brownian regimes;  $\Gamma =$   
 2453  $6\pi\mu a^3 \dot{\gamma} / \Psi$  is a number reflecting the ratio between viscous and colloidal interactions; the  
 2454 particle or flow Reynolds number is used for the transition toward turbulence; the Leighton  
 2455 number  $Le = \mu \dot{\gamma} a^2 / (s\sigma n)$  (with  $s$  the mean distance between the surfaces of two close particles)  
 2456 for the transition between the viscous and frictional regimes; the Bagnold number  $Ba = \rho p \dot{\gamma} s / \mu$   
 2457 is used for the transition between the viscous and collisional regimes.  $\phi_m$  denotes the maximum  
 2458 random solid concentration ( $\phi_m \approx 0.635$  for spherical particles of equal size) and  $\phi_c$  is the  
 2459 minimum concentration for a network of particles in close contact to form ( $\phi_c \approx 0.5$  for spherical  
 2460 particles of equal size). Flow regimes are enclosed in a solid (red) line field that encompasses  
 2461 debris flows surrounded by a long dashed line, while hyperconcentrated flows are enclosed by  
 2462 a short dashed line.

2463 **Figure 5.** Lahar recorded on 5 March 2008 at Semeru volcano, Indonesia (Doyle et al., 2011):  
 2464 A. The flow cross-sectional (wetted) area at the upstream ‘lava’ site; B. The associated body  
 2465 velocity as inferred from the surface velocity; C. The seismic ground velocity  $> 5\text{Hz}$   
 2466 perpendicular to the channel; D. The associated spectrogram showing the seismic frequency  
 2467 distribution; E. The approximate energy in this seismic signal; F. The wetted area at the  
 2468 downstream ‘sabo’ site and the sampled concentration (circles), and; G. The associated body  
 2469 velocity at the downstream ‘sabo’ site. Vertical dashed lines indicate packet arrivals. At the  
 2470 downstream ‘sabo’ site, packet 3 has a sampled particle concentration of 60 vol% and travels  
 2471 at  $4 \pm 0.3$  m/s between sites, whereas packets 1 and 2 have concentrations of 26 vol% and 48  
 2472 vol% and travel at  $1.5 \pm 0.1$  and  $2.9 \pm 0.2$  m/s, respectively.

2473  
 2474 **Figure 6A.** Flow upstream of an obstacle. Axes in pixels (1 pixel = 0.007 cm),  $t$  is time (s).  
 2475 Origin of the time scale: first contact of the flow to the obstacle (Thiberghien et al., 2007). **B.**  
 2476 Flow upstream of an obstacle with reference to a Froude number of 0.79 for the left model  
 2477 (subcritical flow) and 1.35 for the right model (supercritical flow). Axes in pixels (1 pixel =  
 2478 0.009 cm),  $t$  is time (s). On the left, model shows the formation of reflected waves and on the  
 2479 right, the formation of a vertical jet (Reprinted from Millpress Science Publishers, Debris Flow  
 2480 Hazard Mitigation: Mechanics, Prediction and Assessment, Tiberghien et al., Experimental  
 2481 investigations of interaction between mudflow and an obstacle, Pages 286 and 288, Copyright  
 2482 (8 March 2019), with permission from IOS Press. The publication is available at IOS Press  
 2483 through ISBN: 978 90 5966 059 5).

2484 **Figure 7.** Relationship between DF hydro-dynamic and hydrostatic pressures and Froude  
2485 number considering both field data and miniaturised laboratory tests (after Proske et al., 2011,  
2486 reproduced with permission from Taylor and Francis, 11 April 2019).

2487

2488 **Figure 8.** 1-1 Debris flow inundation or buried buildings in Longchi, Du Jiangyan, China. 1-2  
2489 Debris flow buried buildings in Qingping town, China. 1-3 Reinforced concrete structure in  
2490 Zhouqu debris flow: plastic collapse mechanism of columns (photograph: Ge Yonggang). 1-4  
2491 Reinforced concrete structure in Du-Wen motorway service station: collapse with the formation  
2492 of plastic hinges along columns under debris flow impact. 1-5 Reinforced concrete structure in  
2493 Qipan ravine debris flow, Wenchuan County, 2013: plastic collapse mechanism of columns. 1-  
2494 6 Reinforced concrete structure in Qipan ravine debris flow, Wenchuan County, 2013: plastic  
2495 collapse mechanism for most columns. 1-7 Reinforced concrete structure in Zhouqu debris  
2496 flow: failure of ground floor columns and building translation. 1-8 Building collapse caused by  
2497 erosion of foundations by debris flow (Zeng et al., 2015, reproduced with permission from  
2498 Elsevier via Copyright Clearance Center, 7 March 2019).

2499

2500 **Figure 9.** Typology of collapse mechanisms labelled **A** to **E** and their mathematical expression  
2501 (Nigro and Faella, 2008, reproduced with permission from University of Malta Press, 2019).  
2502 Type **A**. Collapse of the tuff or brick external walls. **B**. Three plastic-hinges collapse mechanism  
2503 in reinforced concrete (RC) columns. **C**. Two plastic-hinges collapse mechanism in RC  
2504 columns. **D**. Shear collapse mechanism in RC columns. **E**. Debris-flow impact against the floor  
2505 wall of masonry buildings. Parameters used in impact and collapse models are as follows: The  
2506 ultimate bending moment ( $M_u$ ); the midspan horizontal displacement ( $\delta$ ), in cm; the effective  
2507 dimension ( $a$ ) of the struts; the wall thickness ( $t$ ); the distance ( $L_I$ ) between the wall end and  
2508 the resulting horizontal load; the ultimate load ( $P_u$ ); the specific weight of the LH material ( $\gamma$ );  
2509 the collapse load of the column ( $q_u$ ); the ultimate resistance shear ( $T_u$ ); the width of the masonry  
2510 wall ( $b$ ); the length of the masonry wall ( $L$ ); the thickness of the masonry wall ( $s$ ); the collapse  
2511 pressure ( $P_{uv}$ ), and the unknown position of the central plastic hinge ( $\xi$ ).

2512

2513 **Figure 10.** Debris flow intensity index IDF (computed as  $m^3 s^{-2}$ ) against damage class. Bar  
2514 graphs indicate the number of observations in each group to illustrate group centroids. Different  
2515 building classes are indicated by unique symbols along lines (Jakob et al., 2012, Reproduced  
2516 with permission from Elsevier via Copyright Clearance Center, 7 March 2019).

2517 **Figure 11. A.** Comparison of building vulnerability functions with (a) the flow depth  
2518 functions proposed by several authors, and (b) the impact pressure functions proposed by  
2519 several authors, *in*: Zhang et al. (2018, Reproduced with permission from Elsevier, 2019).  
2520 Flow depths range from 1.7 to 4.2 m. Impact pressure range from 25 to 45.2 kPa, but three of  
2521 them were obtained from snow avalanches. The proposed vulnerability curves have  
2522 limitations: this study examines two types only, brick concrete frame and RC frame, of  
2523 damaged buildings; building geometry and direction, which have a great role on damage  
2524 levels, are not considered, and; building codes in different countries are different.

2525 **B.** Fragility curves after Prieto et al. (2018) for complete damage in un-reinforced masonry  
2526 low-rise (URML) buildings for the following three cases: Field data from South Korea (dots),  
2527 Type A building in South Korea (dashed line), and Colombia (solid line). X-axis is DF  
2528 momentum flux ( $hv^2$ , in  $m^3/s^2$ ). Y-axis is the probability of being in or exceeding a damage  
2529 state. ‘Momentum flux’ is defined as the product of water depth and the square of maximum  
2530 flow velocity at a given point ( $hv^2$ ), and is a realistic proxy for hydrodynamic forces that  
2531 result in lateral displacement of buildings and other valuables (Prieto et al., 2018, reproduced  
2532 with permission from Elsevier, 2019).

2533

2534 **Figure 12. A.** Critical depth and dynamic pressures for the failure of structural classes A0, A  
2535 and B for brick widths of 0.15 m (top) and 0.25 m (bottom) for a set of buildings along a  
2536 ravine that crosses the city of Arequipa, Peru. Shading of lines indicates flow type and  
2537 density, dotted lines and dashed lines represent the minimum and maximum forces required.  
2538 Densities are for a Newtonian flow (NF,  $\rho= 1000 \text{ kg m}^{-3}$ ), hyperconcentrated flow (HCF,  $\rho=$   
2539  $1500 \text{ kg m}^{-3}$ ) and debris flow (DF,  $\rho= 1915 \text{ kg m}^{-3}$ ). **B.** Critical depth–pressure curves for  
2540 building classes A0, A and B subjected to HCFs. Peak normal pressures and corresponding  
2541 depths applied to each city block are plotted as points for each flow rate. **C.** Critical depth–  
2542 pressure curves for building classes A0, A and B subjected to a debris flow DF. Peak normal  
2543 pressures and corresponding depths applied to each city block are plotted as points for each  
2544 flow rate. **D.** Building loss fractions for all flow scenarios where buildings are assumed to  
2545 have a brick width of 0.15 m. **E.** Building loss fraction for all flow scenarios where buildings  
2546 are assumed to have a brick width of 0.25 m (Mead et al., 2017).

2547

2548 **Figure 13.** Rainfall duration, debris flow volume and expected (probable) loss curves based on  
2549 return periods for the case study of the Diano Tribe watershed in Taiwan (Li et al., 2013,

2550 reproduced with permission from Trans Tech Publications via Copyright Clearance Center, 7  
2551 March 2019).

2552

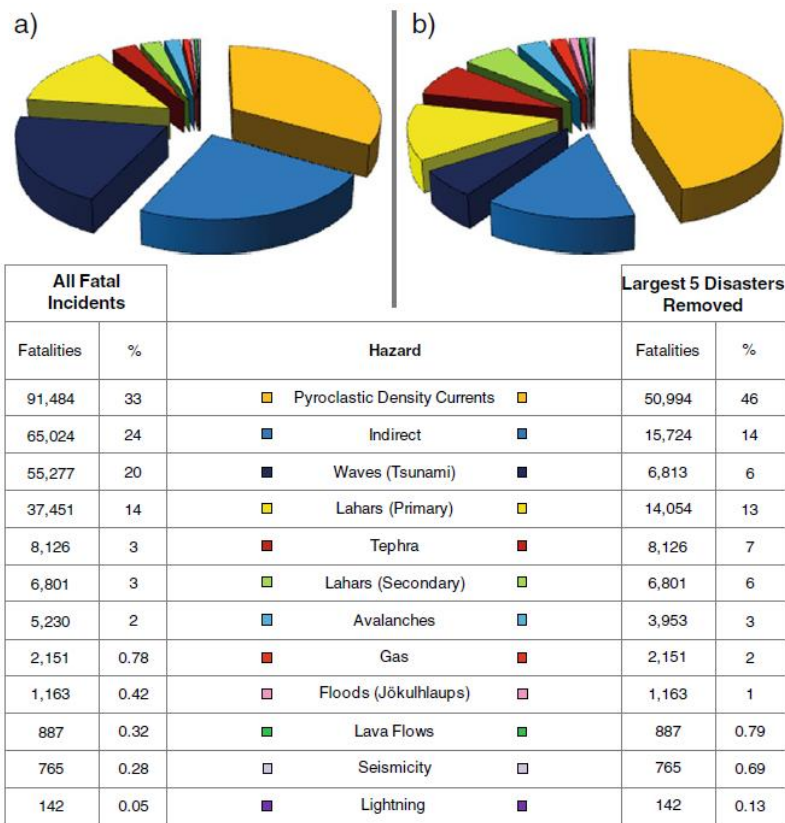
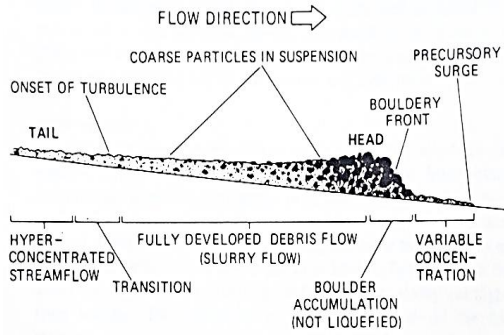
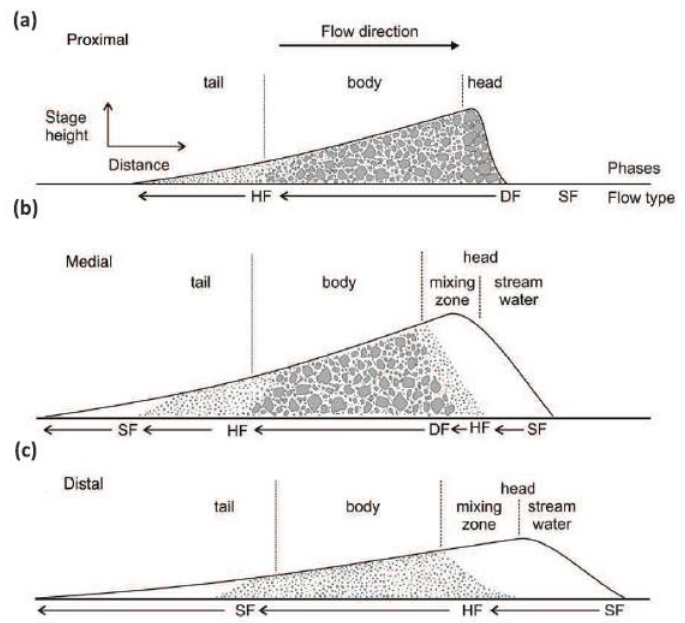


Figure 1. After Auker et al., 2013.

**A****B**

**Figure 2 A.** After Pierson, 1986. **B.** After Vallance, 2000.

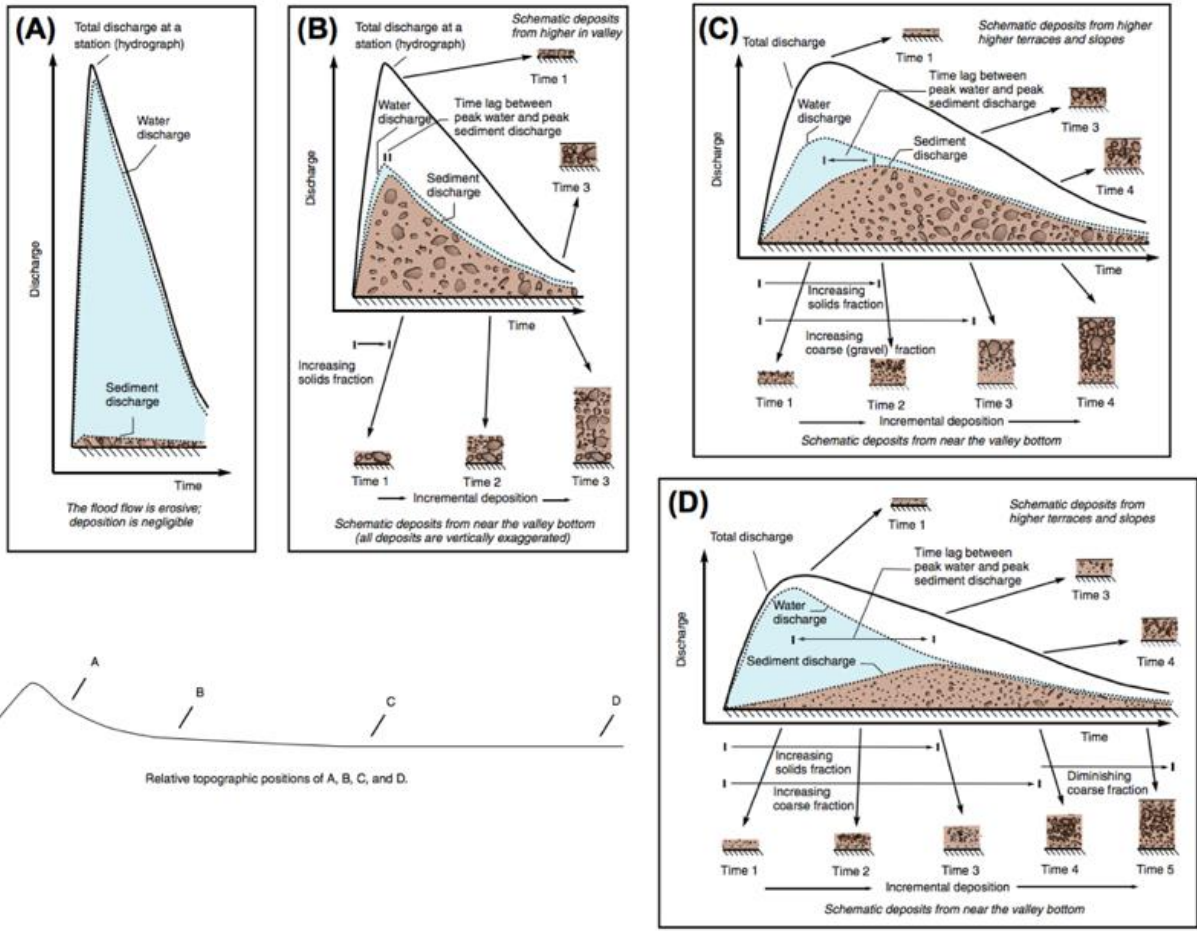
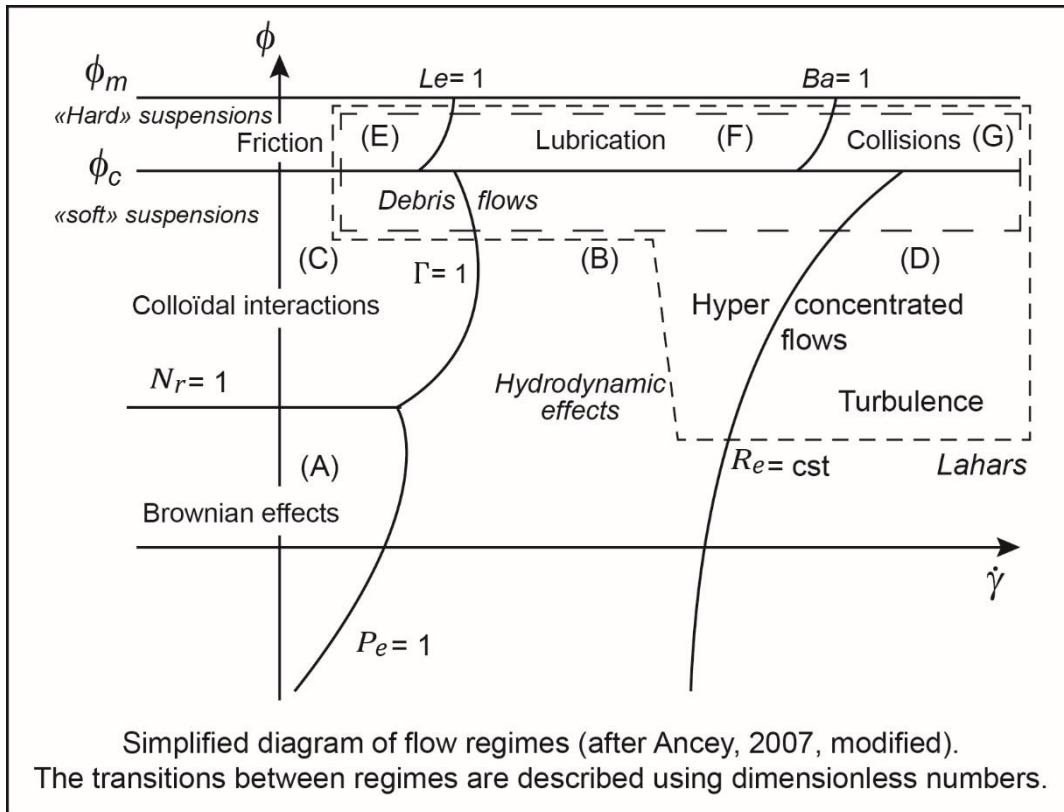
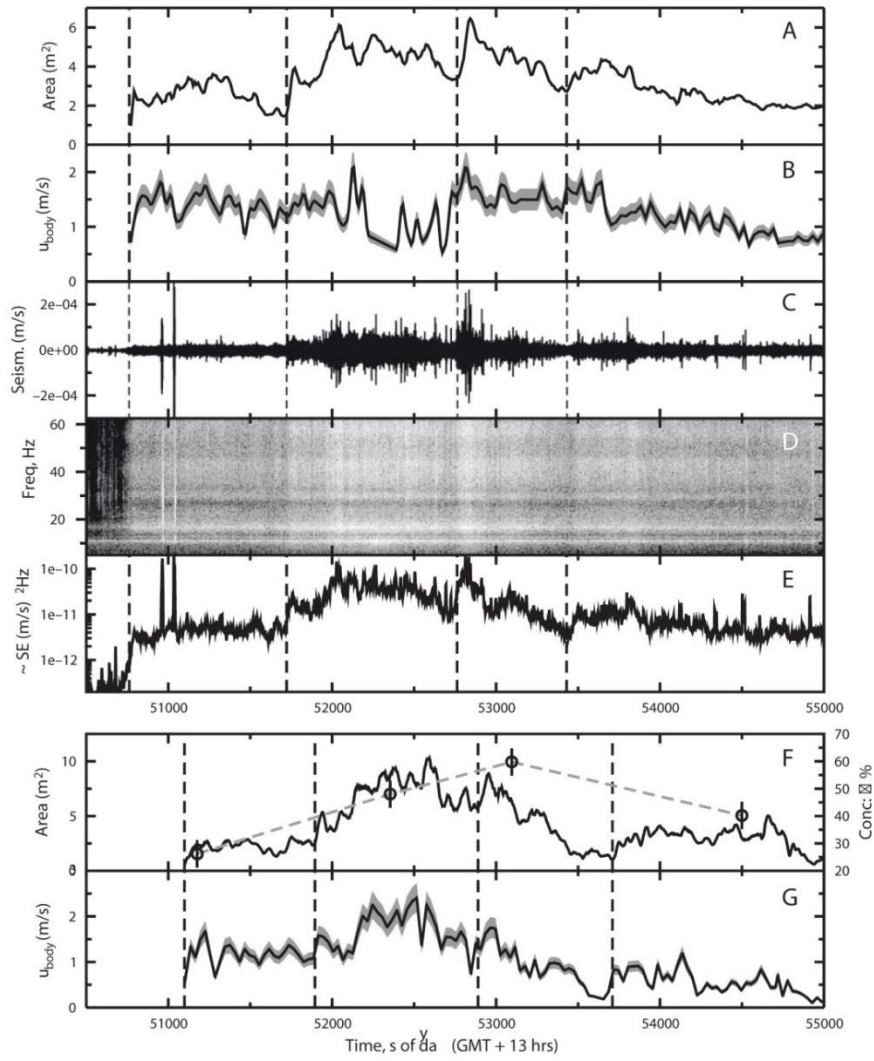


Figure 3. After Vallance and Iverson, 2015.



**Figure 4.** After Ancey (2007, modified).



**Figure 5.** After [Doyle et al. 2011](#).

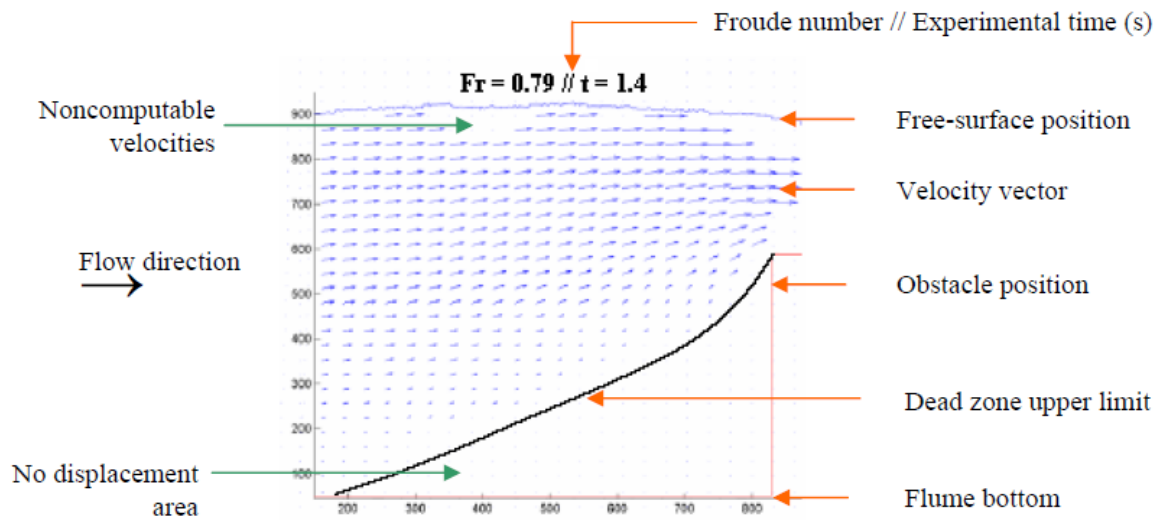


**Figure 6A.** After Tiberghien et al., 2007.

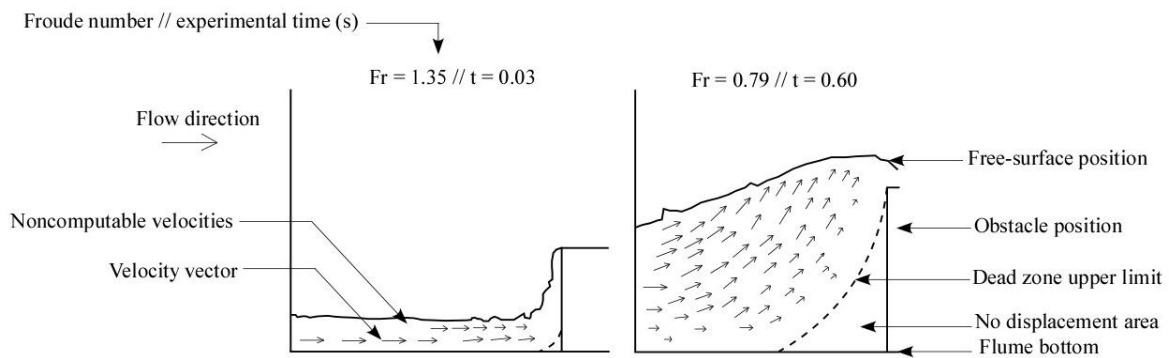


**Figure 6B.** After Tiberghien et al., 2007.

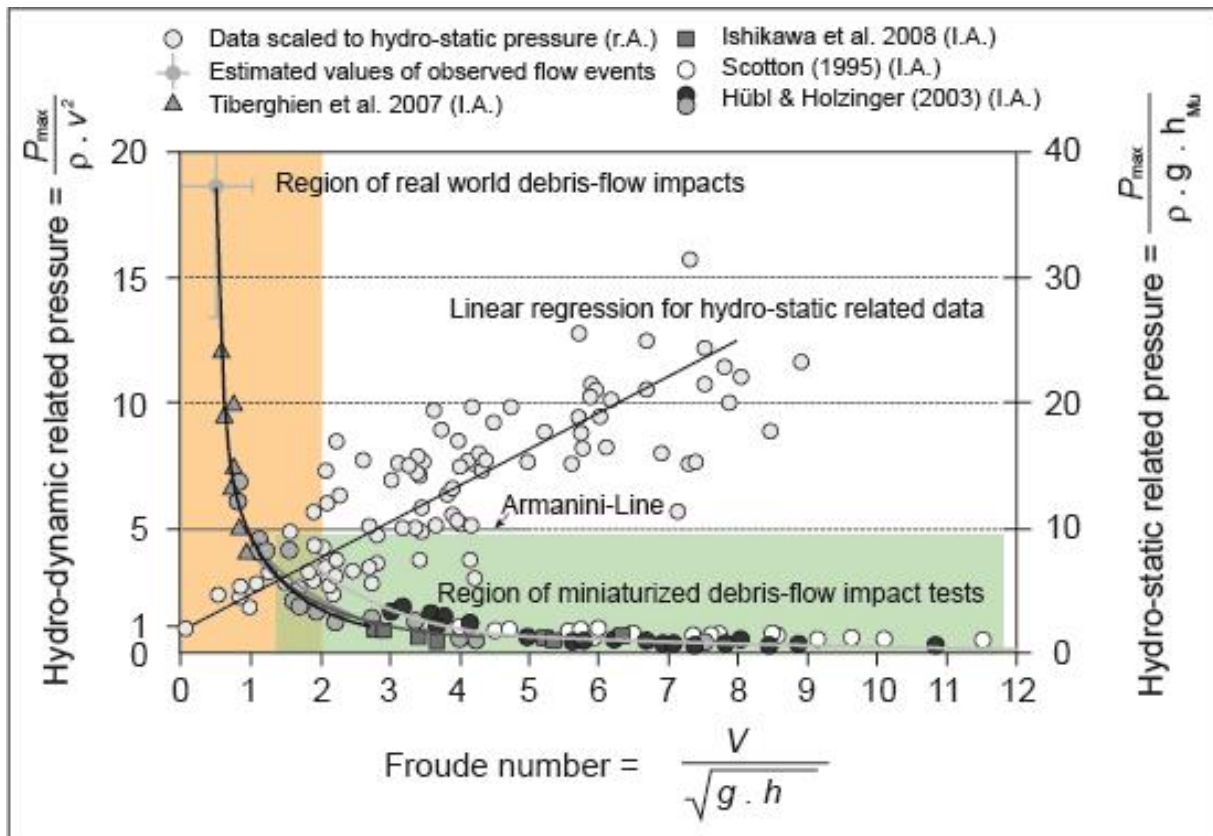


Figure 7. After Proske et al., 2011 (from Hübl et al., 2009, modified).

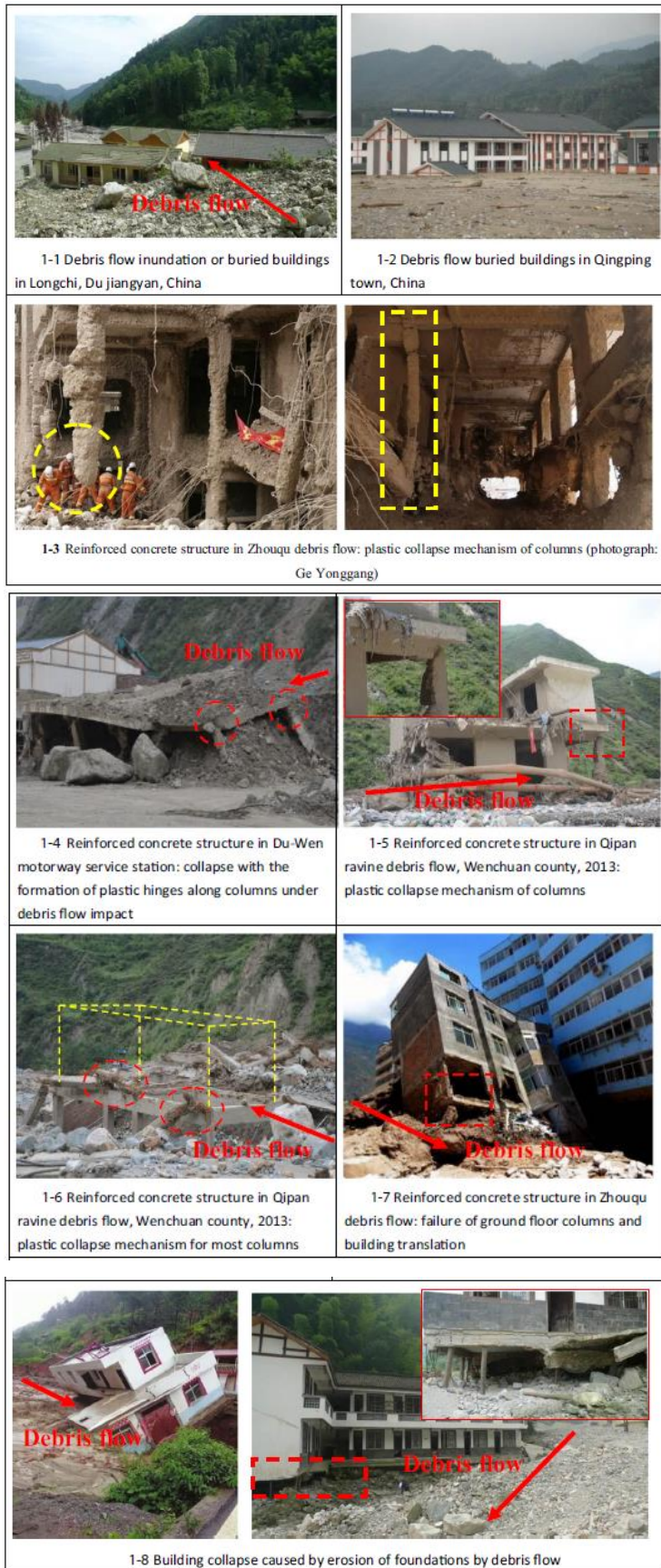
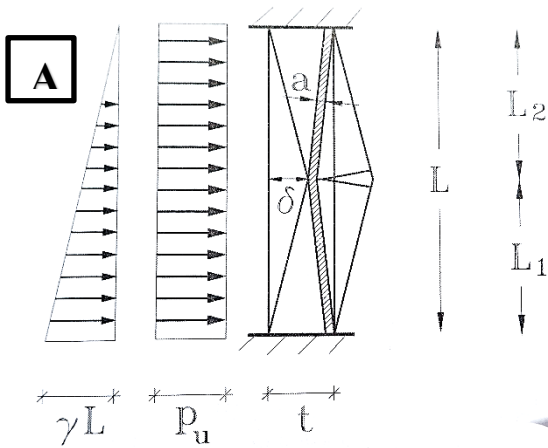


Figure 8. After Zeng et al., 2015

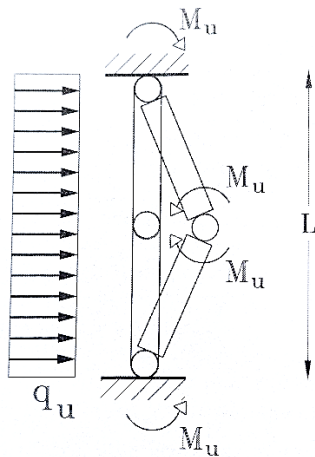


$$P_u = \frac{P_u \cdot 2}{L} - \frac{1}{2} \cdot \gamma \cdot L$$

$$p = C_f \cdot \rho \cdot V^2 \cdot \cos^2 \alpha = \frac{\gamma}{g} \cdot V^2 \cdot \cos^2 \alpha$$

$$V = \sqrt{\frac{g}{\gamma} \cdot \frac{P_u}{\cos^2 \alpha}} = \frac{1}{\cos \alpha} \sqrt{\frac{g}{\gamma}} \left( \frac{P_u \cdot 2}{L} - \frac{1}{2} \cdot \gamma \cdot L \right)$$

**Type-A Mechanism.** Collapse of the tuff or brick external wall.

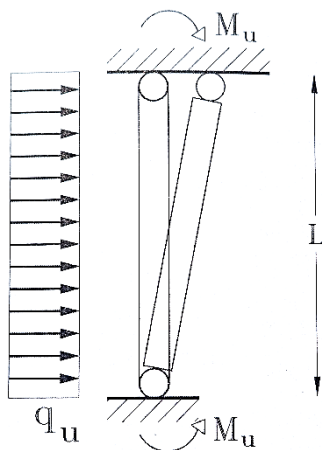


$$q_u = \frac{16 \cdot M_u}{L^2}$$

$$q = C_f \cdot \rho \cdot D \cdot V^2 = \frac{\gamma}{g} \cdot D \cdot V^2$$

$$V = \sqrt{\frac{g}{\gamma} \cdot \frac{Q_u}{D}} = \sqrt{\frac{g}{\gamma} \cdot \frac{16 \cdot M_u}{L^2 \cdot D}}$$

**Type-B Mechanism.** Three plastic-hinge collapse mechanism in Reinforced Concrete (RC) columns

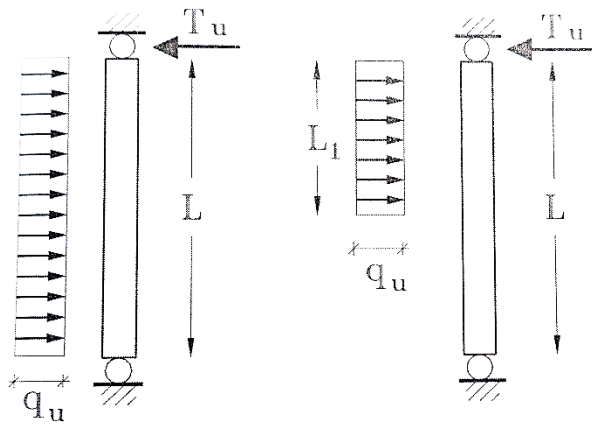


$$q_u = \frac{4 \cdot M_u}{L^2}$$

$$V = \sqrt{\frac{g}{\gamma} \cdot \frac{Q_u}{D}} = \sqrt{\frac{g}{\gamma} \cdot \frac{16 \cdot M_u}{L^2 \cdot D}}$$

$$V = \sqrt{\frac{g}{\gamma} \cdot \frac{4 \cdot \sum_i M_{u,i}}{L^2 \cdot \sum_i D_i}}$$

**Type-C Mechanism.** Two plastic hinges collapse mechanism in RC columns.



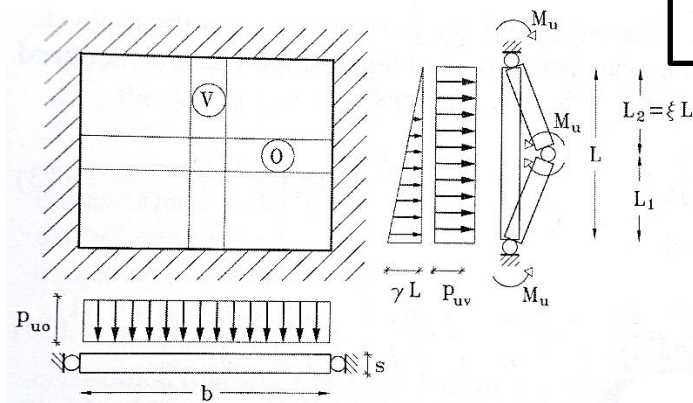
**D**

$$q_u = \frac{2 \cdot T_u}{L}$$

$$q_u = \frac{2 \cdot T_u}{L} \cdot \frac{1}{\frac{L_1}{L} \cdot (2 - \frac{L_1}{L})}$$

$$V = \sqrt{\frac{g}{\gamma}} \cdot \frac{Q_u}{D}$$

**Type-D Mechanism.** Shear collapse mechanism of RC columns.



**E**

$$P_{uv} = \frac{4 \cdot M_u}{L^2 \cdot \xi \cdot (1 - \xi)} - \frac{\gamma \cdot L}{3} \cdot (1 + \xi)$$

$$P_{uo} = 2 \cdot \tau_k \cdot \frac{s}{b}$$

$$V = \sqrt{\frac{g}{\gamma}} \cdot \frac{P_u}{\cos^2 \alpha} = \frac{1}{\cos \alpha} \cdot \sqrt{\frac{g}{\gamma}} \cdot (P_{uv} + P_{uo})$$

**Type-E mechanism.** Debris flow impact against the ground floor wall of masonry buildings.

Figure 9. After Nigro and Faella (2010).

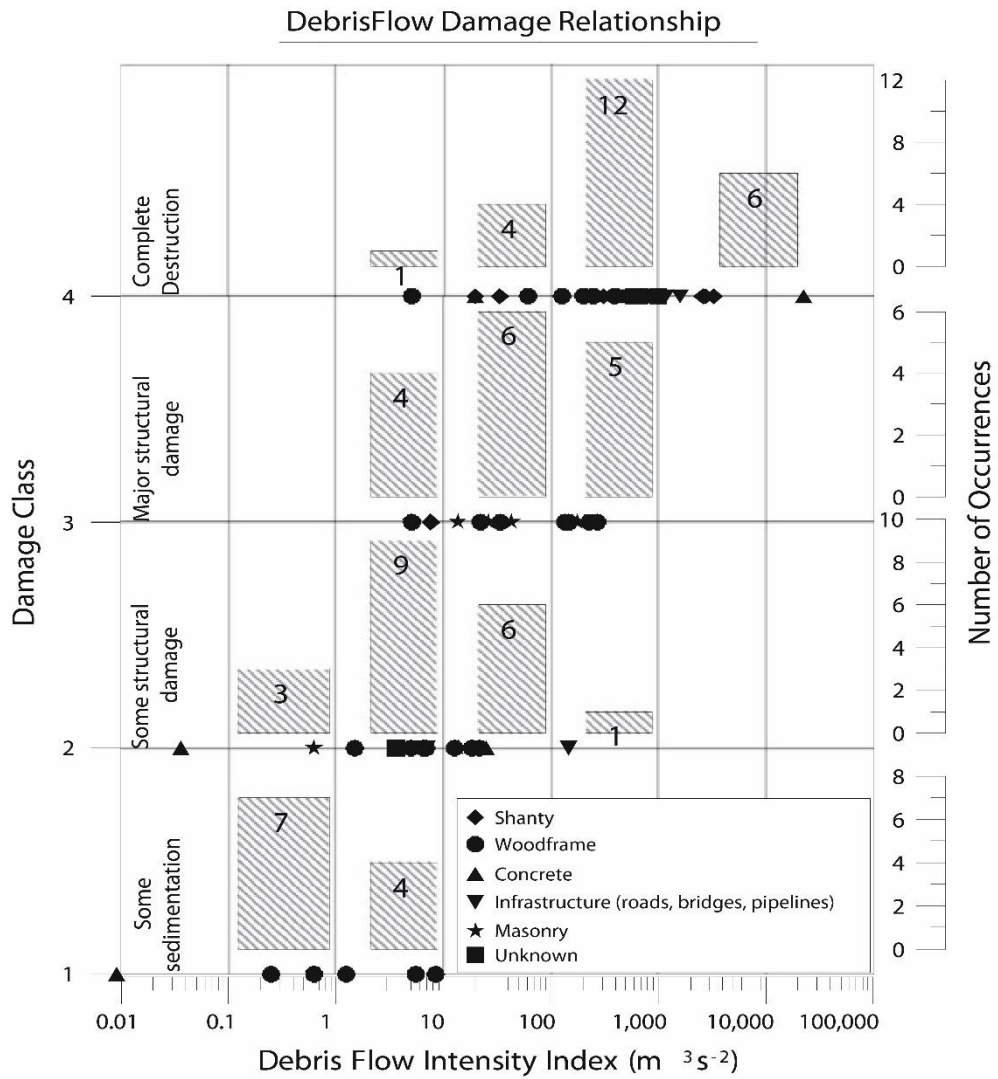


Figure 10. After Jakob et al., 2012.

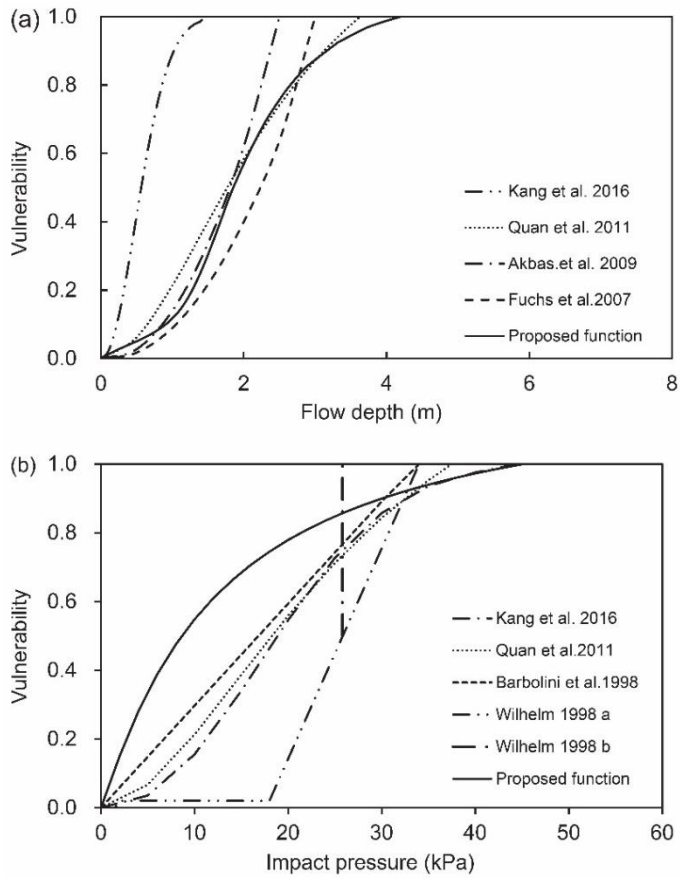


Figure 11 A. After Zhang et al., 2018

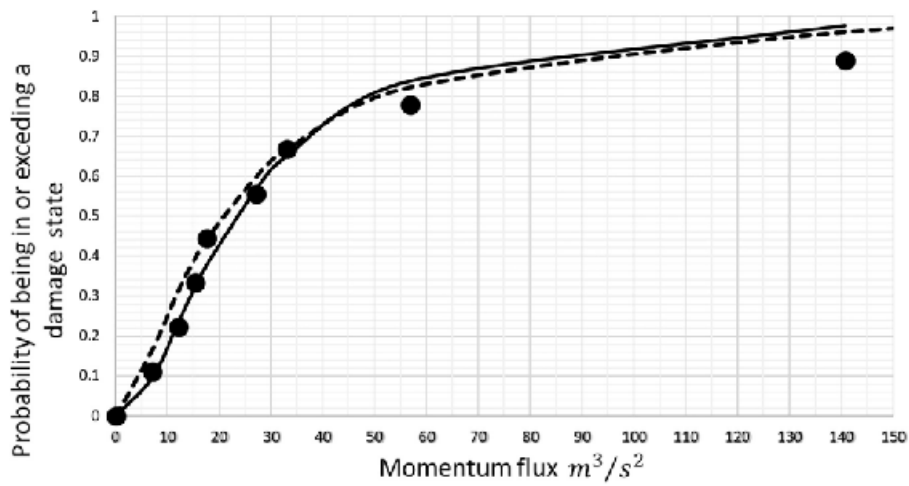


Figure 11 B. After Prieto et al., 2018.

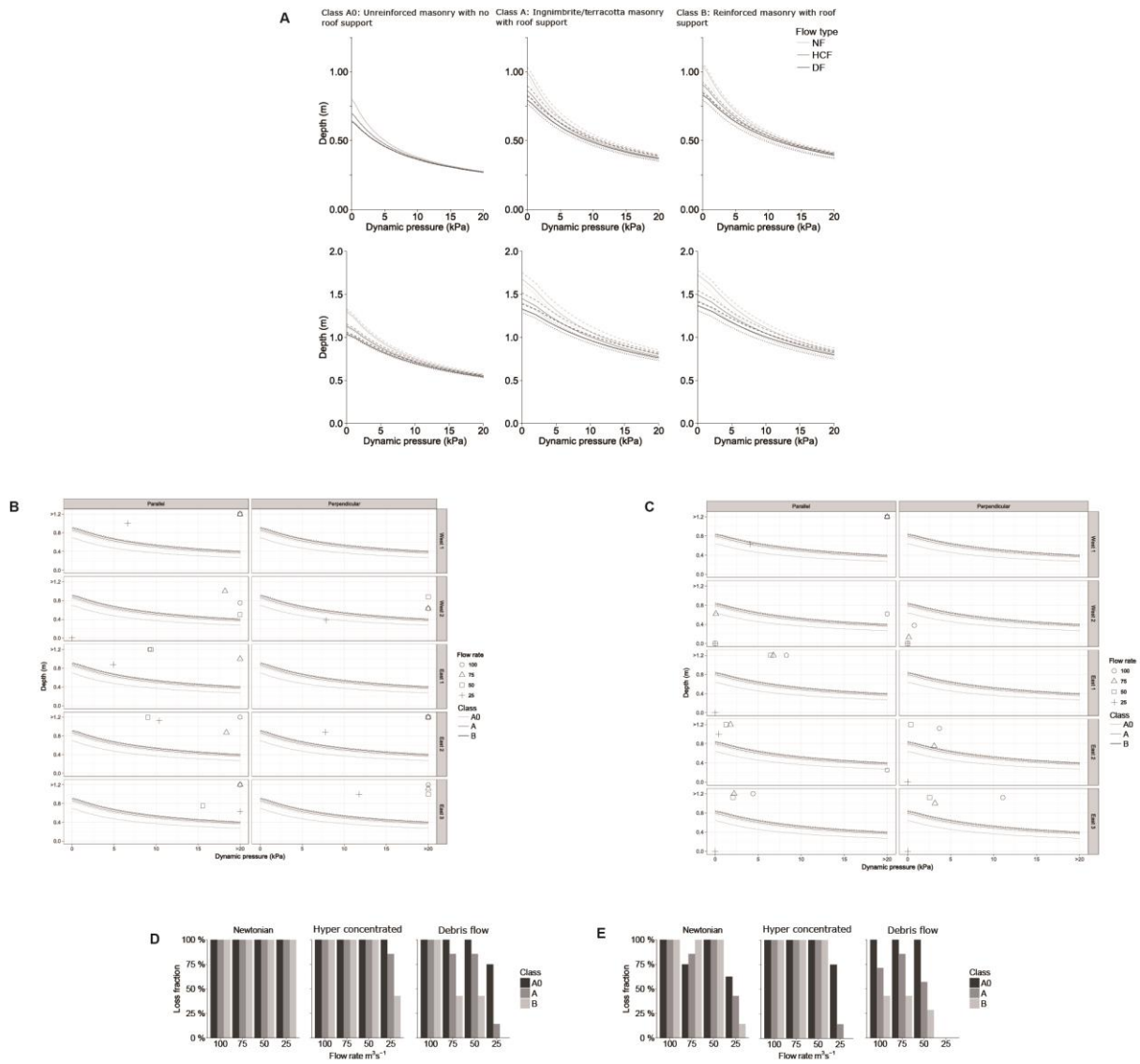
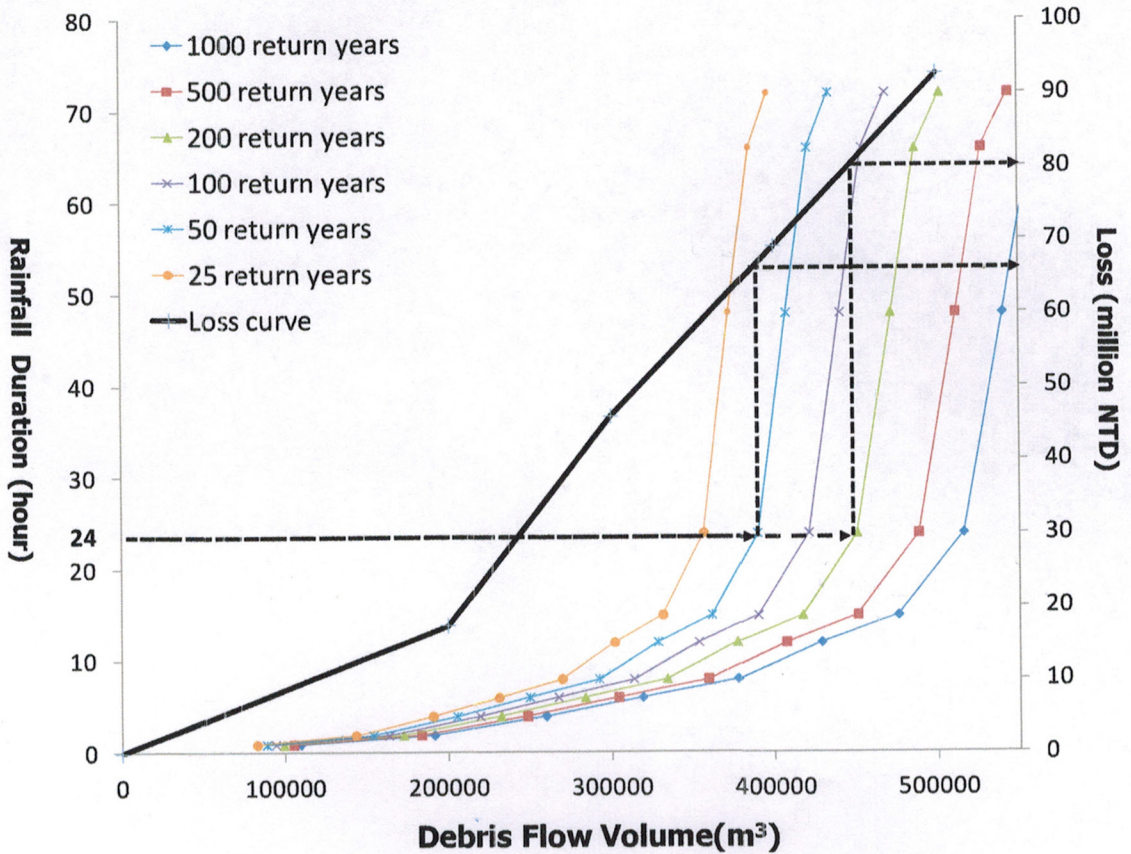


Figure 12. After Mead et al. 2017



Volcan Location Reference No.	Event date	Type, occurrence	Surface km <sup>2</sup>	Volume 10 <sup>6</sup> m <sup>3</sup>	Velocity m/s	Depth m	Peak discharge m <sup>3</sup> /s	Runout distance km	Mobility ΔH/L	Froude number	Solid concentration % vol	Density kg/m <sup>3</sup>	Fatalities/ Affected, displaced	Shear strength τ dn/cm <sup>2</sup>	Damage to habitat, infrastructure and valuables
Galunggung, Indonesia 1,2	1822	p LH	>100	>0.11				10-30					4,000 / Thousands		114 villages
Cotopaxi, Ecuador 1,2,3	1877	p LH	440	370*				300					1,000 / Tens of thousands		Widespread burial
Kelut, Indonesia 2,4	1585, 1919 1990, 2014	p LH	131	0.131				40					10,000 5,200 / Thousands		105 villages (9000 houses)
Mt. Ruapehu, New Zealand 5	1953	pe LH	>100	1.9				60	<1				151 / > 150		Roads and railway bridges
Mt. Ruapehu 6	1945,1995± 1996	p LH, Snow slurry	> 50	2.9 – 11 total	2.1–3.6	2-3	42	8–20	0/025	< 1*	35-52	470–910	2 / 25 families	On average 200–10,000	Tourism, electricity facilities, aviation, agriculture, cattle Total: 129,923, 400 \$NZ (2000)
Mt Ruapehu 7	2007	s LH		0.44	6.5–19.6		1,000–5,500	70	0.02	< 1*	56.8-70.5	1,900–2,200*			
Rio Reventado, Irazu, Costa Rica 8	1963 1965	pe LH, HCF		13–22	2.9–10	8–12	1,130–1,980		0.05	0.5	15-50	1,130–1,180			
Mount St.-Helens, Washington, USA 9	1980	p, pe LH		50.10 <sup>6</sup>	10–31.1	3-6	500–2,300	100		≥ 1	35-70	1,970–2,300	56 / Hundreds	390-11,300	Extensive damage : bridges, Road network
1,9	1919-1982	pe LH, HCF			3.5–4	2.1	450		0.4	0.75–1.72	55-70	1,500–1,800		7,800-8,400	
Nevado del Ruiz, Colombia 10	1985	p LH	2,100	90	4.9–17	5.2-19.8	15,000-48,000	104	0.045	0.7–1.3	30-70	1,800–2,100	23 030 4,420 injured		5092 houses
Mt. Pinatubo, Philippines	1991-1993	pe LH, HCF	200–400	30–40	2.6–3.1	0.5-0.7	10	45	0.025	< 1*	18-31	1110–1500	957 /		112 236 houses

1,11													249,370 affected 5,000 displaced		
Mt. Pinatubo 12	1997	pe LH, HCF	>400	160*	3-6	1-6	20-60	>30	0.02		40-57	1840	26 / 224,610		285 houses
Casita, Nicaragua 1, 13	1998	s LH	7.5	3.1				30					2,513 et 1,000 missing		2 buried towns
Mayon, Philippines 15	2006	pe LH	130	18.8				8-14					1,266 / >10,000 displaced		6 towns, 81 000 houses, roads, plantations, dams
Semeru, Indonesia 16, 17	2000-2004	HCF		0.05-0.5	1.0-5.0	0.6-3.5	50-500	25-35	0.07	1-1.7	31-64	1,980- 2,100			Bridges
	2008	HCF		0.011- 0.11	3-6	0.5-2	25-250	20-25			28-44	1,460- 1,670			
Chaitén, Chile 18	2008	pe LH	10-15	1-3				10 + delta					Several / >2,000 displaced		Flooded town, roads, bridges, harbour
Merapi, Indonesia 19	2011-2012	pe LH	>7	>5				20					3 et 15 injured / 3,000 without shelter		860 houses (215 devastated), 70 ha cultivated land buried
Wrightwood Canyon, South CA, USA 20	1941 1969 1973	DF		0.4-0.5*	1.2-4.4 0.6-3.75	1-2	2,400 1,620- 2,130		0.25	0.87	79-85	2,400 1,620- 2,000		600- 5000	
Malaya Almatinka River, Kazakhstan 20	1975	DF		4.5	4.3-9.4	2.0-8.5	250- 5,980		0.13*	6.12?	67	2,000	?	?	
Kaibab plateau, Arizona, USA 21	1976	DF		0.8-1.10	3-7	1.5-4.5	85-110		0.2	?	80	2,000		221	
Hunshui Gully, China 22	1980	DF		0.5	10-12	3-5	900- 1,000 2,000- 2,300		0.25	1.90	80-85	2,000- 2,300		294-490	

Bullock Creek, Mt. Thomas, NZ 23	1980	DF HCF		0.0195	2.5-5.0	3-5	10-20		0.2	1.26	57-84	1,590-2,130		1,300-2,400	
Pine Creek, Muddy River, WA, USA 20, 23	1980	DF		14	3-31	6-15	6250-28,600		0.1	0.9-2.1	60-85	1,970-2,160		3,900-11,300	
Nojiri River, Sakurajima, Japan 20	1980	DF HCF		0.0061-0.0194	4.8-13	2.4-3.2	48-300		0.1	2.71	30-60*	1,810-1,950			
Saint Antoine, Maurienne, France 24, 25	1987	DF	1.5	0.08				4					0 Hundreds displaced		Bridges, roads, railway, storage 2,580,000 US\$
Larcha, Nepal 20, 26	1996	DF	2.5-5	0.104				2-5					54 100 displaced ?		Constructions and bridges
Harihara River, Japan 26	1997	DF	0.12-0.3	0.0116				0.2-1.2					21		Constructions and bridges
Canadian Cordillera 26	1984-1995	DF	0.03-10	0.02-2				0.02-2					?		
Swiss Alps 26	1990-1999	DF	0.03-5	0.001-0.215				0.07-1.3					?		
Vargas, Venezuela 27	1999	DF	5-6	15-21				6-10					15-19,000 Tens of thousands affected/displaced		Severe destruction, loss of \$2 billion
Sarno, Campania, Italy 1, 14	1998	s LH HCF	1.38	1.42	6-20	0.5-3	600-3,400	0.9-2.1	0.1-0.27		30-45	1750 ± 80	150-161 >50 evacuated	200-3000	Several tens of buildings and vehicles
Jiangjia Ravine, Yunan, China 28	1961-2000	DF HCF	1.6-2.1	0.161-0.240				6-8					?		Heavy damage to local infrastructure
Central Italian Alps 20	1997 2002	DF	3.1-9 8-10	0.006-0.09	3.1-9 8-10	2-2.5 2-5*	23-71 35-400	1-2	0.6	?	90	2,400-2550*			

The Dolomites (Fiemmes, Belluno), Italy 29	2006	DF	0.62	0.907	2	0.5- 2.57	181- 476	0.5	0.4-0.5	?	63-72.5	?			Forest, 1 road, paths
Wenchuan, China Post-earthquake 30	2008-2016	DF HCF	0.65-1.97	0.73-1.98				0.7-2.4				Several tens	Thousands affected		Severe damage to villages, reconstructed sites, highway and bridges

Flow Processes	Flow properties	Impacts		Consequences
		Direct	indirect	
<b>Hydrostatic pressure</b>	Water and sediment mixture leading to drowning and trapping of living organisms or fall of elements onto them	Drowning Trauma	Shock	Living organism is drowned, trapped, or buried. Severe trauma (due to building collapse, debris), mutilation and fractures of limbs and skulls.
				Injuries due to conveyed heavy objects carried in LHs or DFs that induce broken bones, or from bodies driven against stationary objects and crushed.
<b>Boulders as missiles and impact pressure</b>	$E = f(m, u)$ Energy upon impact of block depends on kinetic energy of the missile, hence on its velocity and mass	Trauma	Shock	Injuries, deep lacerations, penetrating wounds, and infections after admission to hospitals
<b>Ablation and undercutting</b>	See undercutting of a structure (Table 5)	Trauma Drowning	Shock	Landslide induced by lateral undercutting and sapping that can lead to people falling from banks into moving flows.
<b>Accumulation</b>	Cohesion, density $\rho$ , and $\phi$ permeability of flow	Induration Cementation	Change in topography	Trapping of living organisms in LH and DF flows that produces traumatic asphyxia or traps people in the valley, alluvial plain or at home surrounded by LH. Runoff on indurated crust of deposits may contribute to overrun and avulse towards channels apparently outside main flows.
	Leakage of industrial toxic elements and domestic waste in LH flow	Contamination, disease	Contamination and pollution Deterioration of harvest	Contamination of soils, streams and phreatic reservoirs by toxic elements. Withering of harvest owing to excess water supply that can lead to food shortage and digestive problems.
	Concentration in toxic elements together with their mobility		Remobilisation of material	LH/DF deposits can be remobilised by arrival of additional LH, avulsion, or by heavy rainstorms.
<b>Chemical and Biological actions Heat and pH</b>	Temperature of hot LHs Contamination of water Low pH of LH/DF traveling across or scouring sulphur-rich fumarolic field or industrial waste	Chemical and temperature burns	Infections Deterioration	Chemical and temperature burns to plants, fauna and people produced by pH and high temperatures. Infections including gas gangrene, tetanus, and necrotizing tissues in victims rescued after being in the mud for days (Baxter and Horwell, 2015).

Table 2



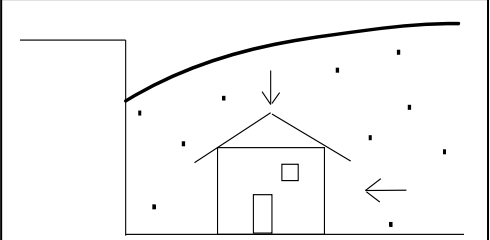
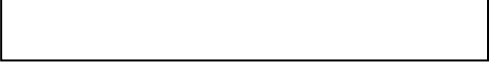
**Table 3**

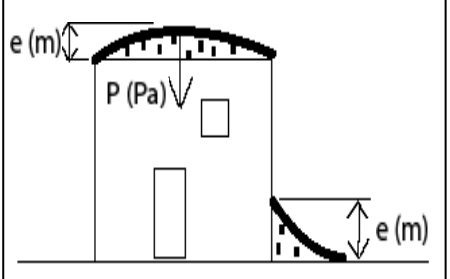
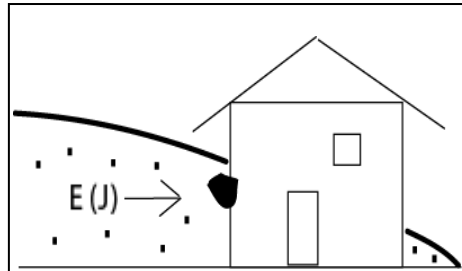
DOMAIN	GEOMORPHIC UNIT	ACTING PROCESS	IMPACTS		GEOMORPHIC CHANGES increasing hazards	
			Direct	Indirect	Mid term	Long term
RIVER CHANNEL AND VALLEY	Bed	Burial Scouring	Deposition, sedimentation	Tail cuts down in bed & deposit	Bed raising	Overspill made possible
	Channel and bends	Infilling readjustment	Favors overrun Cut through	Debris entrainment	Down cutting	Gradient steepening
	Overtop banks and terraces		Pressure Sterilizes land & habitat of natural life	Volume growth down valley Destroy forest	Increasing width	Avulsion made possible
	Profile: transversal longitudinal	Alteration enhances & blocks steepens	Favors overspill Accelerates flows	Landslides on adjacent slopes	Valley narrows or enlarged	Headward retreat Entranchment Progradation
OUTSIDE AND BEYOND RIVER VALLEY	Terraces and beyond edges	Overbank Sediment supply Damming river	Limited deposit Bank collapse	Excess sediment Contamination Bury forest	Enlargement	Overspill and avulsion
	Tributary, independent drainage	Avulsion, Sudden supply to rivers	Extensive aggradation	Unexpected burial	Re-activation	Coalescence of multiple valleys
	Volcaniclastic plains & fans	Overland flow Anastomosis Migration	Large valleys & extensive fans Solid charge	Creates and/or erode	Extension of ring plains	Growth or and degradation
VOLCANO MOUNTAIN foothills	Volcano flanks	Erosion and deposition	Topographic changes	Destabilization	Erosion Sedimentation	Degradation and aggradation
	Ring plain Fans	Volcaniclastic sedimentation	Aggradation Progradation	Hydrological perturbations	Overbank and avulsion	Channel shifting

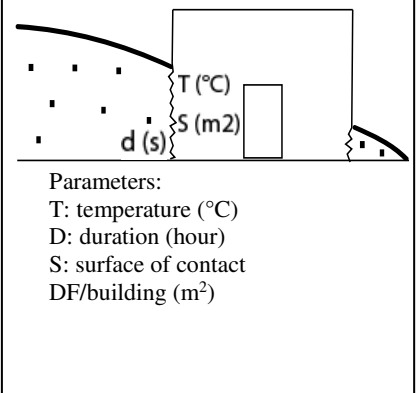
Numerical Program and origin	Input parameters				Output	Applications Usefulness	Limitations	References
LAHARZ USGS, CVO	Grid and DEM Maximum cross-sectional and planimetric areas of inundation.	Lahar volumes from geological record and historical events.	Height/Length ratio Break-in-slope at base of volcanic cone.	Channel wetted section; two equations.	Automatic mapping of surfaces potentially susceptible to inundation by LHs.	Useful, first-order, automatic delineation of hazard zones. User friendly.	Empirical, statistical method (not based on laws of mass and energy conservation).	Schilling, 1998, 2014 Iverson et al., 1998 Rickenmann, 2005 Williams et al., 2008, Oramas-Dorta et al., 2009a,b
TITAN2D Two-phase flow version Geophysical Mass Flow Group SUNY at Buffalo USA	A depth-averaged, thin layer computational fluid dynamics code to simulate geophysical flows. Uses GRASS GIS that simulates dry granular flows by combining integrated equations and DEM.	Initiation point, momentum, transport parameters, solid ratio. Laws of mass and momentum balance. Coulomb constitutive description.	Internal and basal friction, initiation site: pile of debris, Solid to pore-fluid ratio. Two constituent phases.	Bedrock type and friction coefficient using GRASS GIS	Uses GRASS GIS to provide inundation areas and depth, run-up heights, including effect of substrate friction.	Provide flow limit, Inundation areas, Runout path, flow velocity, deposit thickness, travel time	Needs rheological tests and initiation conditions.	Pitman, Le, 2005 Patra et al., 2005 Sheridan et al., 2005 Williams et al., 2008 Procter et al., 2010a,b, 2012
TITAN 2F Derived from SUNY at Buffalo	A computational code derived from Tian2D and created to simulate biphasic flows over a DEM.	Flow volume Based on past events or probabilities	High resolution DEM, GIS		Titan2Fcombines the Coulomb and hydraulic models to calculate flow behavior	Used with a probabilistic approach that yields estimated flow extent and path, flow depth, velocity range, and dynamic pressure	Needs rheological tests and initiation conditions.	Córdoba et al., 2015, 2018 Rodríguez-Espinosa et al., 2017
VOLCFLOW LMV, UCA	A physically based code; laws of mass and energy conservation.	Deposit thickness, flow velocity, discharge.	High-spatial resolution DEM.		Extent and path Deposit Thickness.	Able to map flow hazards, volcanogenic tsunami, lava flows, flows, dense and dilute PDCs, reproduce emplacement of fluidized flows in laboratory.		Kelfoun and Druitt, 2005
FLO-2D Software Inc., 2017	A flood routing, hydrodynamic, two dimensional model. Eulerian framework. Non-linear explicit difference method based on a quadratic rheologic law.	Flow volume, stress, yield stress, Dynamic viscosity, Shear rate, depth-integrated. Dissipative friction slope. Surface detention, Manning, Strickler "n".	Dynamic-wave momentum equation.	Depth-averaged channel equations continuity momentum. Finite-difference routing scheme.	A hydrodynamic two-dimensional model simulates the progression of inundation associated with a given flow volume. Based on the volume-conservation model.	Able to route non-Newtonian flows over a complex topography. Allows obstructions pathways such as infrastructure to be examined.		O'Brien et al, 1993, 2000 Quan Luna et al., 2011 Caballero and Capra, 2014; Wörni et al., 2012 Charbonnier et al., 2018b

EDDA 1.0 Erosion–Deposition Debris flow Analysis	A Model to better understand flow actions, to reproduce the dynamic chain of flow processes: transport, erosion and deposition.					Based on measurements acquired in natural channels, the model seems to better estimate parameters used for hazard estimate	Does not allow the the flow dynamics to be as well understood as the dataset obtained from the scale flume experiments	<a href="#">Chen and Zhang, 2015</a>
DCL USGS, CVO	A new depth-averaged mathematical model to simulate all stages of DF motion, from initiation to deposition. Basal Coulomb friction. Reduction of friction by high pore-fluid pressure.	Shock-capturing numerical scheme with adaptive mesh refinement, implemented in the open-source DCLAW package.	Simultaneous evolution of flow thickness, solid volume fraction, basal pore-fluid pressure and 2 components of flow momentum.	Each of five equations contains a source term represents the influence of state-dependent granular dilatancy	Critical role of granular dilatancy in linking coevolution of the solid volume fraction and pore fluid pressure, which regulates debris-flow dynamics	D-Claw performs well in predicting evolution of flow speeds, thicknesses and basal pore-fluid pressures (measured in large-scale flume experiments, USGS)	The Darcian hydraulic permeability of the debris and its compressibility: are likely to vary as a consequence of dilation and agitation of moving debris. No data or theories exist to constrain these variations.	<a href="#">Iverson and George, 2014</a> <a href="#">George and Iverson, 2014</a>
RAMMS Rapid Mass Movements SLF Swiss Institute for snow avalanche research	Unified software package, 3D- three-process modules for snow avalanches, DFs and rockfalls, together with a protect module and visualization module in one tool.	Mean velocity flow height, density, g, friction slope, downslope angle. Cell size. Frictional force, cohesiveness, normal stress on the slip surface.	dry Coulomb-type friction coefficient, viscous resistance, which varies with square flow velocity.	One-phase approach, Voellmy fluid model. Assuming no shear deformation.	A finite volume scheme used to solve the shallow water equations in general three-dimensional terrain. Well calibrated, hydraulics-based, depth-averaged continuum model.	Flow body moves as a plug with with everywhere the same mean velocity over the height of the flow, the friction slope.		<a href="#">Cesca and D’Agostino, 2008</a> <a href="#">Christen et al., 2010</a>
DAN “Dynamic Analysis”, DAN3 And DAN-W, for rapid landslides	A continuum model based on a Lagrangian solution of the equations of motion with selected material rheologies: plastic, frictional, laminar, turbulent, Bingham, Coulomb viscous flow, Voellmy fluid.	Material parameters change along the flow. Lateral confinement of the path. in stiffness of the moving mass. Yield strength, dynamic viscosity.	Moving Lagrangian Frame. A rheological kernel to be calibrated. Basal flow resistance force.	Internal rigidity of coherent slide debris moving on a thin liquefied basal layer.		DAN of rapid and composite flows includes a generalized rheological kernel, which can be calibrated so as to obtain the best simulation of the observed behavior of particular flows.	It is approximate as it involves the reduction of a complex and heterogenous 3D-problem into a simple one D formulation. Trial and error procedure.	<a href="#">Hungr, 1995, 2008</a> <a href="#">Hungr, 2010</a>

SPH Smoothed particle hydrodynamics	A mesh-free Lagrangian method where the coordinates move with the fluid.	Discrete particles have a spatial distance over which their properties are smoothed by a kernel function.	Kernel functions commonly used include Gaussian function, the quintic spline and the Wendland $C^2$ kernel.	Euler equations of mass conservation and momentum balance.	Simulates the dynamics of continuum media, such as solid mechanics and fluid flows. Divides the fluid into a set of discrete particles.	Several benefits over traditional grid-based techniques. It is possible to simulate fluid motion using SPH in real time.	Technical Difficulty in treating boundary conditions. Does not consider bulking and debulking processes.	<a href="#">Pastor et al., 2009</a> <a href="#">Haddad et al. 2010</a> <a href="#">Pasculli et al., 2013</a> <a href="#">Mead et al., 2017</a>
Improved CA Cellular Automata model for estimating the runout extent of a DF event over 3-D topography.	CA model simulates DFs using simple transition rules that represent local interactions between cells and neighbors.	A new transition function that considers both the topography and persistence effects of DFs, and including results from a well-documented flume experiment.	DF persistence function influenced by the slope of the previous direction, approximating the law of cosines at a steep slope and the Gamma law at a gentle slope.	Cellular space, CA neighborhood, finite set of states of each individual automaton, transition rules, and time step.	The simulated deposition perimeter pattern, runout distance, and sediment depth are in high accordance with data from the post-hazard field investigation.	Consequent computational efficiency.	Inability of the persistence function to take into account the effects of the viscosity of the DF mass and bed-sediment entrainment. The model uses a constant flow depth for a single routine.	<a href="#">Han et al., 2017a,b</a> <a href="#">D'Ambrosio et al., 2003</a> (e.g. SCIDICCA)

PROCESSES EXERTED BY DFS AND LHs	SCHEMATIC ILLUSTRATION OF FORCES ACTING ON EDIFICES	MECHANISMS AND PARAMETERS TO BE CONSIDERED	EQUATIONS USED	FACTORS INCREASING RESISTANCE / WEAKNESS IN EXPOSED VALUABLES
<p><b>HYDRODYNAMIC PRESSURE:</b></p> <p><b>horizontal or lateral component</b> <i>hc</i></p>	 <p>P (Pa), F (x), S (m<sup>2</sup>), H (m), m (x), U (m/s<sup>-1</sup>), V (m<sup>3</sup>), ρ dv/dx, D (hour), θ (°)</p>	<p><math>P = F/S</math> where S is the building surface over which force F is applied, where <math>F = m \cdot a</math> and acceleration = <math>dv/dx</math>, which is a derivative of x based on the size of space to be considered and m is the LH or DF mass: <math>m = \rho \cdot V</math> (ρ flow density x V volume), hence <math>P = [(\rho \cdot V) \cdot (dv/dx)] / S</math> Other parameters to be considered are: duration, roof angle, edifice structural heterogeneity, and number of storeys.</p>	<p><math>P = [(\rho \cdot V) \cdot (dv/dx)] / S</math></p> <p>How ductile a material is governed by deformation rate and temperature via the</p> <p>Young modulus* (elasticity) E according to Hooke's law: <math>\sigma = F/S = E \cdot \epsilon</math>, where ε expresses the relative lengthening.</p>	<p>High Young modulus determines the rigidity of a material. The thicker a material is, the more rigid it is. Pressure is higher on joints and space between dressed stone. Most vulnerable construction materials: adobe, sheet metal, brick, wood, lapilli concrete, dry stone without joint.</p>
<p><b>vertical component</b> <i>vc</i></p>		<p>Pressure P, Force F, LH or DF mass, acceleration, S edifice surface, duration, roof angle, edifice structural heterogeneity, storey number.</p>	<p><math>P = [(\rho \cdot V) \cdot (dv/dx)] / S</math> Young modulus, same as above.</p>	<p>The more fragile a material is, the more prone to disaggregation it is. The higher the ratio mass / surface and density is, the more stable the material is. The more porous the material is, the more fluid it can absorb. Percentage, size and contours of openings.</p>
<p><b>HYDROSTATIC PRESSURE:</b></p> <p><b>vertical (ground) and lateral (soil) from differential depth outside and inside structure</b></p> <p><b>Capillary rise</b> <b>Buoyancy</b></p>		<p><math>F = \rho \cdot g \cdot h</math>, where ρ is LH or DF density g is the gravitational force, and h is LH or DF depth.</p> <p>LH/DF density and viscosity, flow height, gravitational constant; water content, pore pressure. Dense flows become buoyant Buoyancy force causes structure and objects to float.</p>	<p><math>P = [(\rho \cdot V) \cdot (dv/dx)] / S</math></p> <p>The effects on a building of lateral and uplift pressure forces due to the hydrostatic pressure of surrounding LH / DF and saturated ground. Lateral pressure concentrated at bottom of wall, and also drawn up into porous material due to capillary rise.</p>	<p>Pressure exerted on housing induces deformations on loadbearing interior walls, hence deformation propagates to other edifice elements. Young modulus. Permeability of construction material. Water content in material may exceed the plasticity threshold. Vulnerable materials as above.</p>

<p><b>DEPOSITION AND ACCUMULATION OF LH OR DF MATERIAL</b> Flow inundates, overflows; resides and starts depositing</p>	 <p>Parameters: E: thickness (m) P: hydrostatic pressure (Pa)</p>	<p><i>Case of deposits on roof:</i> Pressure P depends on force and surface on which it is exerted. F mass of elements deposited on roof.</p> <p><i>Case of deposits on the edifice edges:</i> deposits exert an oblique force due to wall-buttressing, dependent on lahar depth.</p>	<p>Pressure <math>P = F / S</math></p> <p><math>F = m * g</math></p> <p>Mechanism similar to that of vertical dynamic pressure</p> <p>Permeability of edifice Water content of material</p>	<p>Burial leading to filling up all openings and closing access to edifice. Contrasting effect: infill material makes the structure more resistant, but corrosion of metal makes it more vulnerable. Stream/river and rainfall-induced runoff may be derived towards the edifice and water saturated deposits may be remobilized. Sudden and steady supply in water into the edifice that may lead to wither the structure. Percentage and size of openings are critical.</p>
<p><b>UNDERCUTTING SCOURING</b> Flow undercuts river bank, bridge or building</p>	<p>LH/DFs are able to erode ground under buildings or construction foundations. Lateral scouring and undercutting of substrate under buildings.</p>	<p>Significant role of flow density <math>\rho</math>, amount of solid particles, velocity <math>v</math>, and geomorphic site: flows erode more easily if channels become narrower and sinuous.</p>	<p>Deformation, cracks opening, vertical displacement and collapse.</p>	<p>Erosion of ground or building foundations triggers deformation due to structure load. Soil properties and bedrock characteristics play a major role on scouring effects.</p>
<p><b>COLLISION: BOULDERS ACTING AS MISSILES</b></p>	 <p>Parameters: E: Kinetic energy (J) Drag coefficient</p>	<p>Energy liberated upon impact depends on kinetic energy of the projected element, therefore velocity, mass and size.</p> <p>Impact may be discrete or continuous (time of inundation is a critical parameter).</p> <p>Inclined roofs provide more surface area likely to be hit by blocks.</p>	<p>Mechanism similar to that of horizontal component of dynamic pressure</p> <p>Compromise between plasticity and relaxation capacity of construction material and its resistance to missiles.</p>	<p>Plasticity/rigidity of the edifice roof and walls can be modified owing to continuous impacts of blocks. They may resist more if block impacts are discrete or brief. Missiles can crack or break walls out. Cracks may facilitate water circulations into the edifice. Blocks can open holes in walls or displace load bearing walls leading to structural collapse, but material that fell out can be used again by flows. Openings (glass, plastic, wood) are highly vulnerable.</p>

<p><b>SOIL DEFORMATION</b></p>		<p>Pore pressure in soil/bedrock  <math>\epsilon</math> soil deformation, induced by retreat or swelling soil mechanism or liquefaction.          Soil porosity and <math>\phi</math> permeability          Clay content of deformable soil (e.g. swelling clay minerals).</p>	<p><math>\epsilon, \phi</math>  <math>\phi</math>          Young modulus          Mechanisms similar to that of hydrostatic pressure</p>	<p>The edifice structure deforms following soil and ground deformation.          Crack propagation and hinges across the structure can lead to collapse.</p>
<p><b>PARTICULAR CASE OF HOT (PRIMARY) LAHARS:</b>          temperature          pH</p>	 <p>Parameters:          T: temperature (°C)          D: duration (hour)          S: surface of contact DF/building (m<sup>2</sup>)</p>	<p>Heat transfer from lahar flow to housing elements and furniture:          T &lt; 100°C, heat loss from lahar, area of contact on housing Sb, at ground level (Sl), and exposed to air (Se).          Thermal conductivity and heat capacity of material hit by hot lahar.          pH of fumarolic or sulphur-rich (often hot) DF or LH</p>	<p>T, Sb, Sl, Se          Thermal conductivity          Heat capacity          and properties of material hit</p>	<p>Temperature at which more vulnerable elements can undergo combustion. At least temperature increase makes construction material more fragile to the effects of other processes above.          Permeability and physical-chemical characteristics of materials bear upon behavior to temperature increase.          Slow combustion of material through infiltration, in particular timber, openings (doors, windows), plastic and wood interior and balcony.</p>
<p><b>Non-physical actions</b></p>	<p>Chemical, biological, nuclear effects from outside</p>	<p>Acid, sewage, oil mixing with water</p>		<p>Contamination          Rusting</p>

**Table 5.**

Table 6

TYPOLOGY OF ASSETS OR VALUABLES		Built environment and services				Economic activity				Agriculture, crops, forest, fishery			Transportation network, services				Vehicles, machinery			Water supply			Power supply			Telecommunications Electric network			Health care, welfare, social fabric			Hydraulic, defense work		REQUIRED ACTIONS		
CATEGORIES OF COMPONENTS AND ITEMS		Residential	Commerce, industry	Education, religion	Sport	Factory, warehouse	Mining, tourism	Trade	Finance, insurance	Field, crops	Machine, shelter	Cattle, poultry	Road, bridge	Rail network	Airport	Harbour	Car	Lorry	Tractor, other	Water tank	Irrigation	Sewage	Dam	Oil, gas	Heating	Overhead line	Grounded line	PC, station	Hospital, dispensary	Local facility	Common house	Canal, dyke	dam, wall	Cleaning	Repair	Replacement
According to four scenarios**	Damage percent	5	5	3	2	5	2	1	0	10	5	10	5	3	1	2	5	5	2	5	5	5	5	2	1	5	0	1	10	10	5	5	5	X		
		2	0	2	0	10	5	2	1	25	15	15	20	5	2	3	15	10	5	10	10	5	10	5	2	10	1	2	20	15	10	15	15	X	X	
		5	4	0	3	20	10	5	2	50	25	20	45	15	5	10	30	20	10	25	20	10	20	10	5	20	2	10	40	30	20	25	25		X	X
		100	90	60	50	35	20	10	5	100	30	30	90	45	20	30	50	30	20	50	30	20	50	25	15	30	5	15	60	40	30	50	50		X	X
	Damage ratio	0.1	0.05	0.03	0.01	0.1	0.01	0	0	0.2	0.1	0.2	0.1	0.1	0.2	0	0.1	0.1	0.1	0.1	0.1	0.1	0.1	0.05	0.01	0.1	0	0.005	0.2	0.1	0.05	0.1	0.1			
		0.3	0.2	0.1	0.05	0.2	0.1	0	0	0.3	0.2	0.2	0.2	0.1	0.1	0	0.3	0.2	0.1	0.2	0.2	0.1	0.2	0.1	0.01	0.2	0.01	0.02	0.3	0.2	0.1	0.2	0.2			
		0.5	0.3	0.2	0.1	0.4	0.3	0.1	0	0.5	0.3	0.2	0.4	0.2	0.1	0	0.4	0.3	0.2	0.4	0.3	0.2	0.4	0.2	0.1	0.3	0.02	0.2	0.4	0.3	0.2	0.3	0.3			
		1	0.9	0.7	0.5	0.5	0.4	0.2	0.1	1	0.4	0.4	0.9	0.6	0.3	0.1	0.6	0.4	0.2	0.5	0.3	0.2	0.5	0.3	0.2	0.4	0.1	0.2	0.7	0.5	0.3	0.5	0.5			
	Loss of function	10	5	3	2	5	2	1	0	10	5	10	5	3	1	2	5	5	2	5	5	5	5	5	2	10	0	5	10	10	5	10	10	X	X	
		25	15	10	5	10	5	2	1	20	10	15	20	10	3	5	15	10	5	10	10	5	10	10	5	15	5	10	25	20	10	20	20	X	X	
50		30	25	10	20	10	5	2	40	15	20	50	25	10	15	30	20	15	20	15	10	25	25	10	25	10	15	50	40	25	30	30		X	X	
100		80	70	50	50	20	10	5	80	30	40	80	50	30	20	90	50	25	50	25	15	50	50	25	50	20	25	70	50	30	60	60			X	
Function loss index	0.1				0.05				0.1			0.05				0.1			0.1			0.1			0.1			0.15			0.1					
	0.25				0.1				0.2			0.2				0.15			0.2			0.2			0.15			0.25			0.2					
	0.5				0.25				0.4			0.5				0.3			0.25			0.3			0.2			0.5			0.3					
	1				0.4				0.8			0.8				0.9			0.5			0.5			0.5			0.7			0.6					
Economic cost \$US x 10 <sup>6</sup>	0.1-0.99				0.1-0.99				0.01-0.099			0.1-0.99				0.01-0.099			0.1-0.99			0.1-0.99			0.1-0.99			1-9.9			0.1-0.99			X		
	1-9.9				1-9.9				0.1-0.99			1-9.9				0.1-0.99			1-9.9			1-9.9			1-9.9			10--99			1-9.9			X		
	10--99				10--99				1-9.9			10--99				1 --9.9			10 --99			10 --99			10--99			100-999			10--99			X		
	100-1,000				>100				10--99			>100				10--99			100			100			>100			100-999			>1000					X